Growth Types and Bonding Mechanisms for Copper / Steel Interface by Fusion Welding

F. A. Hashim
Mechanical Engineering Department
Engineering College
University of Thi-Qar

Q. J. H. Al-Hussnioy
Welding and Inspection Department
Electrical Ministry

Abstract

The aim of this work is to study the possibility of joining copper (ASTM , C1020100) to low carbon steel (ASTM A36) using the shielded metal arc welding (SMAW) and the gas tungsten arc welding (GTAW) processes by eight types of electrodes ; ERNiCrFe-5 , ERNiCu-7 , ECu , ECuSn-A, E309L, E 312, E7018 , and ENi-1. Joint is designed as single – V – butt weld for 5 mm thickness plate . From the microstructure observation there were two kinds of boundaries ; the first is homogenous weld , which happens when fillers with chemical composition is similar to those of one of the parent metals . While the second type is heterogenous nucleation , which happens when the chemical compositions of the fillers and the parent metals are not similar . Three types of solidification were regonized ; the first is epitaxial from the copper side , the second is nonepitaxial from the steel side , and the third type is competitive which shown in the two sides . Solidification cracks on the steel side are shown , and these cracks are filled by brazing process . All tested specimens in tension and bending show the copper properties .

المستخلص

الهدف من اجراء هذه الدراسة لمعرفة امكانية لحام النحاس نوع (ASTM , C1020100) الى الفولاذ المنخفض الكاربون نوع (ASTM , A36) بطريقتي اللحام القوس المعدني المغطى (SMAW) ولحام القوس الكهربائي باستخدام قطب التنكستن (GTAW) . مادة الحشو المستخدمة هي :

ECuSn-A , ECU , ERNiCu-7 , ENRiCrFe-5 , ENi-1 , E7018 , E312 , E309 L

وصلة اللحام مهمة تناكبية احادية الحفر . سمك صفائح اللحام 5 ملم . من ملاحظات البنية البلورية اتضح لنا نوعين من الحدود البلورية ، الاولى حدود منتظمة والتي تحصل باستخدام اسلاك لحام مشابهة لأحد طرفي وصلت اللحام ، الثاني هي حدود هجينة والتي تحصل نتيجة لعدم تماثل سلك اللحام مع الاساس المعدني لثلاثة أنواع من الاغماد وحصلنا عليها الاولى نوع Epitaxial والذي كان على العموم في جانب النحاس ، الثاني يسمى Nonepitaxial والذي يكون من جانب الفولاذ ، اما الثالث فأنه نوع Competitiveوالذي يكون من كلا الجانبين . حدوث بعض التشققات على الساخن والتي لوحظ املائها بطريقة البرصمة وبذلك يرتفع مرة اخرى بمتانة وصلة اللحام . لوحظ تماثل المواصفات الميكانيكية للشد والحني لجميع الوصلات والتي تمثل المواصفات الميكانيكية للنحاس .

1. Introduction

In fusion welding the exiting base-metal grains at the fusion line act as the substrate for nucleation . Since the liquid metal of the weld pool is in intimate contact with these substrate grains and wets them completely (0 to 0) Figure (1) . Crystal nucleate from the liquid metal upon the substrate grains go without difficulties . Such a growth initiation process shown in Figure (2)is called epitaxial growth [1] . When welding with a filler metal (or joining two different materials) , the weld metal composition is different from the base metal composition , and the weld metal crystal structure can differ from the base metal crystal structure . When this occurs , epitaxial growth is no longer there and new grains will have to nucleate at the fusion boundary [1] .

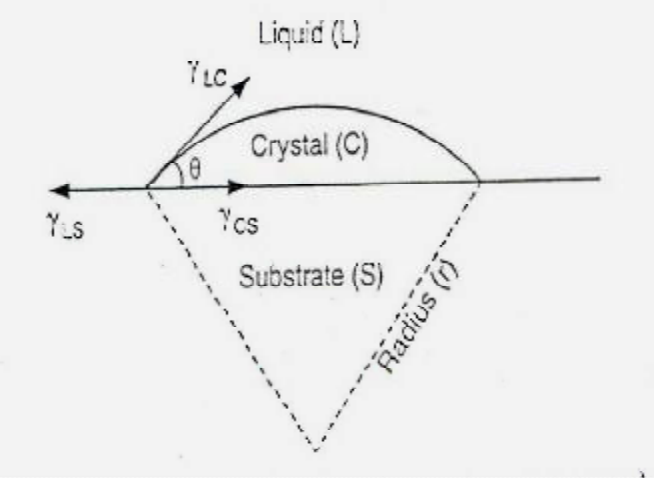

Figure (1). Spherical of crystal nucleated on planer substrate from liquid. [1]

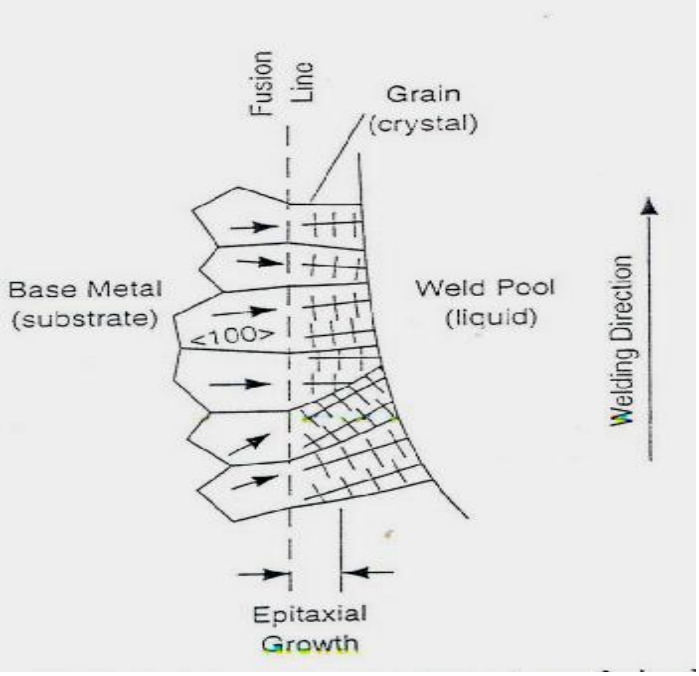

Figure (2). Epitaxial growth of weld metal near fusion line.[1]

Nelson et al [2] pointed out that weld type 409 St St of BCC structure with monel filler metal of FCC structure produce a FCC weld metal deposit . Figure(3) shows the fusion boundary or interface microstructure . They concluded that the neucleation of solid weld metal occurs on heterogeneous site on the partially melted base metal at the fusion boundary (Nonepitaxial growth) . The grains structure near the fusion line of a weld is dominated either by epitaxial growth , when the base metal and the weld metal have the same crystal structure, or by nucleation of new grains when they have different crystal structure a way from fusion line . However , the grain structure is dominated by a different mechanism known as competitive growth , as sown in Figure (4) [3] . The aim of this study is to realize the bonding structure and mechanisms for dissimilar weld of copper to steel by different fillers .

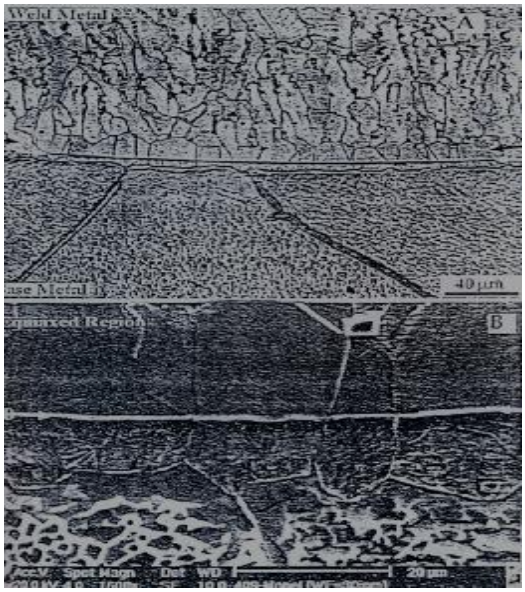

Figure (3). Fusion boundary microstructure in 409 ferritic st.st (bcc) welded with Monel filler wire (fcc):(A) optical micrograph : (B) scanning electron micrograph . White arrows:fusionboundary;dark arrows: new grains nucleated along fusion boundary .[2]

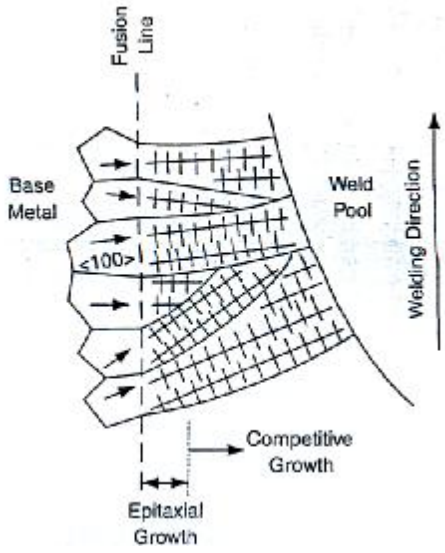

Figure (4). Competitive growth in bulk fusion zone .[3]

2. Experimental work

In order to accomplish the objective of this work , the following equipments were use : manual electric arc welding machine type ESAB LHF400 , gas tungsten arc welding machine type Miller 403 , grinding and polishing machine type Hergon MP 200 to prepare microscopic test specimens , gas torch for preheating , tensile test machine type Instrom 1195 of 2500 Kg capacity , and optical microscope connected to a computer with a digital camera . Steel plates type AISI 1015 ASTM A 36 , and copper plates type OFHC , ASTM DS – 65 , C10100 – C15735 , them of 5 mm thickness . Table 1 shows the nominal chemical composition of steel and cooper compared to standard specifications AISI-ASTM for both metals [4] .

Table (2) shows the mechanical properties for steel and copper compared to standard specifications AISI-ASTM for both metals [4]. Different types of electrodes as filler metals alloys were used according to ASME specification (section 11, part C). Table 3 shows

Table (1). Chemical composition of steel and copper. [4]

ELEMENT	LOW CARBON STEEL AISI 1015 ASTM A36		COPPER (OFHC) ASTM DS-65(C10100-C15735
	Nominal %	Actual %	Nominal %
C	0.13-0.18	0.15	-
Mn	0.3-0.6	0.402	-
P	-	0.04	-
S	-	0.05	-
Si	0.129	0.06	-
Cr	-	-	-
Ni	-	-	-
O2	-	-	0.002-0.003
Cu	-	0.034	99.9
Fe	Rem	Rem	-

Table (2). Mechanical properties for steel and copper.[4]

MECHANICAL PROPERTIES	COPPER (OFHC) ASTM DS-65(C10100-C15735		LOW CARBON STEEL AISI 1015 ASTM A36	
	Actual	Nominal	Actual	Nominal
Tensile Strength (N/mm²) MPa	216	200-250	410	380- 450
Modulus of elasticity GPa	112	110	210	205 min
Elongation%	46	60	28	25 min
Hardness (Kg/mm^2) Vickers	85	80	185	180

Table (3) . Chemical composition of electrodes and filler (FMA).[5, 6]

Electrode(filler) type	Fe	C	Mn	Si	Cu	Ni	Cr	P	Mo	Ti	Sn
E Cu	0.2	_	0.1	0.1	Rem.	_	_	_	_	_	
E CuSn-A	0.25	_	1.5	_	Rem.	_	_	0.05 to 0.35	_	_	4.0 to 6.0
E Ni-1	o.75	0.1	0.75	1.25	0.25	92.0 min.	_	0.3	_	1.0-4.0	4.0 to 6.0
ER NiCrFe-5 Inconel Alloy	6.0	0.08	1.0	0.35	0.5	70.0 min.	14.0	0.03	_	_	_
ER NiCu-7 Monel Alloy	2.5	0.15	4.0	1.25	Rem.	62.0 to 69.0	_	0.02	_	_	_

E 309L	**Rem.**	**0.04**	**0.25 to 0.5**	**0.9**	**0.75**	**12-14**	**22 to 25**	**0.04**	**0.75**	**_**	**_**
E312	**Rem.**	**0.15**	**0.25 to 0.5**	**0.9**	**0.75**	**8 to 10.5**	**28 to 32**	**0.04**	**0.75**	**_**	**_**
E 7018	**Rem.**	**0.04**	**1.6**	**0.75**	**_**	**0.3**	**0.2**	**_**	**0.3**	**_**	**_**

the nominal chemical composition of these electrodes [5,6]. Table 4 shows the mechanical properties for these electrodes [5,6] . The steel and copper plates were cutted to 300 x 150 x 5 mm for mechanical testing , and to 50 x 50 x 5 mm for microstructure testing . The steel surfaces were sand blasted , while copper surfaces were cleaned by alcohol . The welded plates were arranged as in figure 5 [7] , which welded by different types electrodes ECu , ECu-Sn-A , E7018 , E309L , E312 , and ENi-1 . by shielded metal arc welding (SMAW) process .

Table (4). Mechanical properties for electrodes and filler (FMA). [5, 6].

Electrodetype	**Yield strength Mpa**	**Tensile strength Mpa**	**Elongation%**
E312	500	750	25
ER NiCrFe-5 Inconel Alloy	410	640	40
E 309L	470	580	32
E 7018	445	540	29
ER NiCu-7 Monel Alloy	330	530	45
E Ni-1	320	450	25
E CuSn-A	235	330-390	25
E Cu	170	225	20

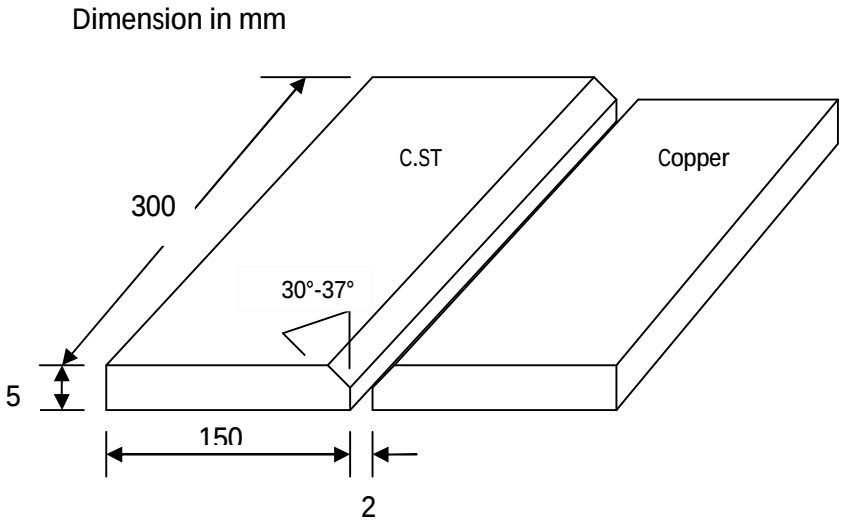

Figure (5). Dimensions of specimen according to ASME Section IX.[7]

Also the same dissimilar joint as in Figure (1) be welded by gas tengsten arc welding (GTAW) process using electrode types ERNiCrFe-5 , and ERNiCu-7, as shown in Table (5). The welded specimens were cutted according to AWS specification as shown in Figure (6). The tensile samples were prepared according to ASTM E 8M-88 specification as in Figure (7). While , the Figure (8) shows the standard dimensions for bending test according to ASTM E 190 specification .

Table (5). Variable parameters for electrodes and filler.

processes	Electrode& filler		Current		voltage	speed mm/min.	Gas flow L/min.	preheat C°	Interpass temp.C°
	type	Dia. mm	polar	Amp.					
GTAW	ERNiCrFe-5	2.4	DCSP	170-200	11	15	3.5	400-500	250-300
	ERNiCu-7	2.4	DCSP	170-200	11	15	3.5	400-500	250-300
SMAW	ENi-1	3.2	DCRP		24	16	-	400-500	250-300
	ECu	3.2	DCRP		22	15	-	400-500	250-300
	ECuSn-A	3.2	DCRP		23	15	-	400-500	250-300
	E309L	3.2	DCRP AC		24	18	-	400-500	250-300
	E312	3.2	DCRP		25	17	-	400-500	250-300
	E7018	3.2	DCRP AC	110-150	23	17	-	400-500	250-300

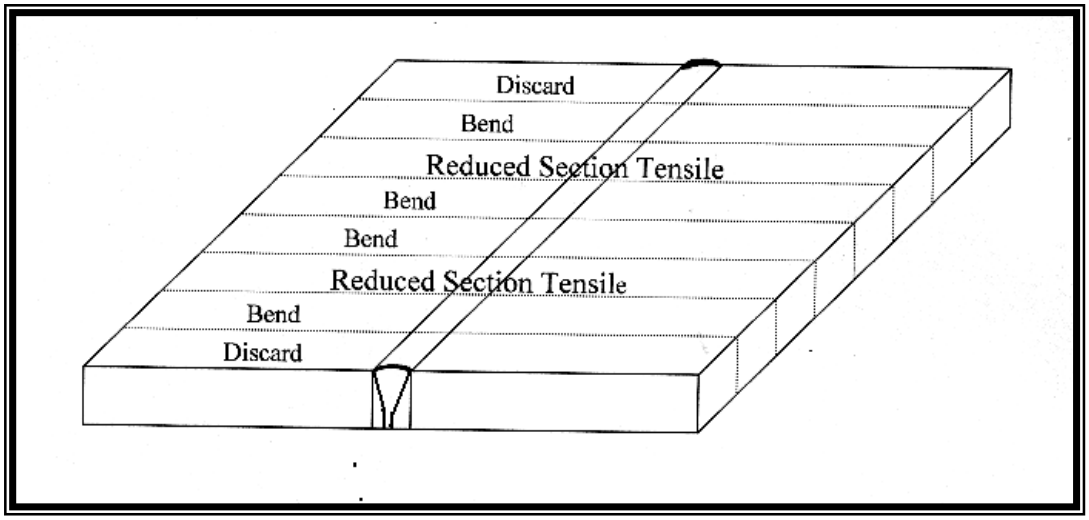

Figure (6).Specimen of the sample to be tested, according to AWS specification [7].

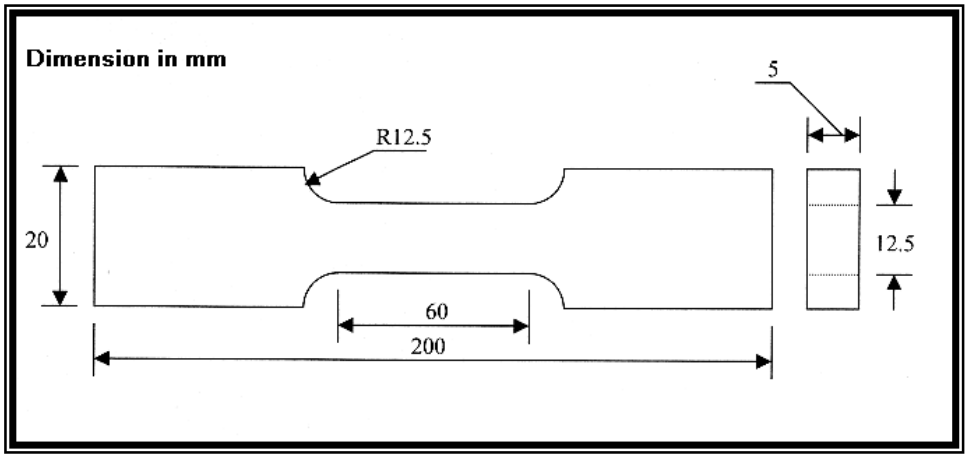

Figure (7) .Tensile test specimen, according to ASTM (E 8M-88) specification [7].

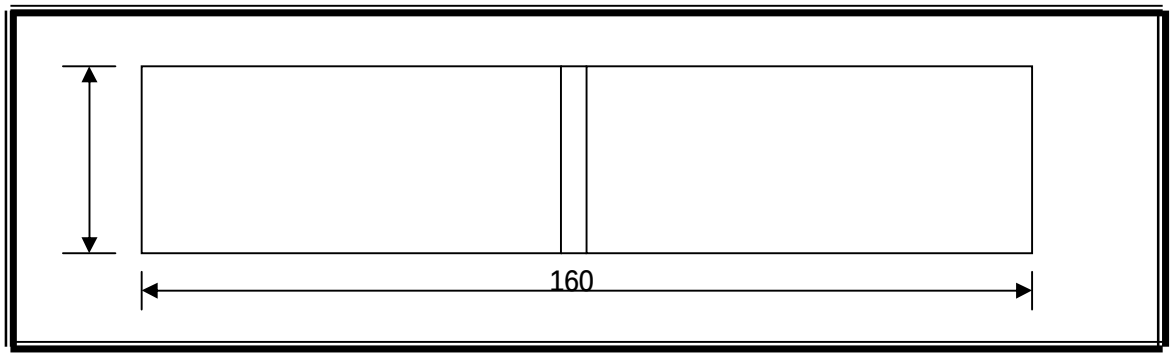

Figure (8). Bending test specimen, according to ASTM (E 190) specification [7].

3. Results and discussion

3.1 E7018 Weld Deposits

A dark dots appear in the copper weld pool , which are represent an oxide particles due to the new process of dissimilar joining (Figure 9 – a) . Epitaxial nucleation is formed during the solidification process at the fusion boundary, Figure (6–b) . While a homogenous weld interface is produced because of the similarity in the chemical composition at the steel side , (Figure 9 – C) .

Porosity

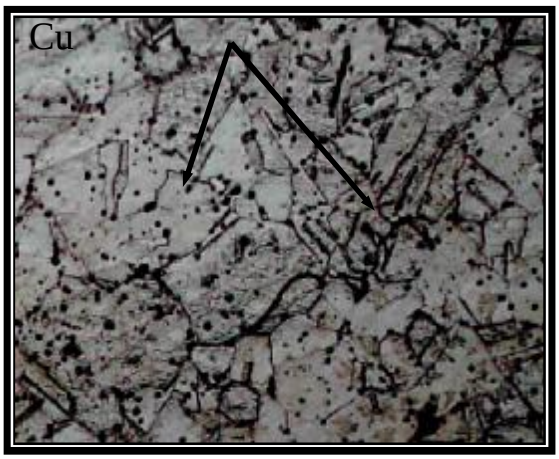

Figure(9-a)

Epitaxial

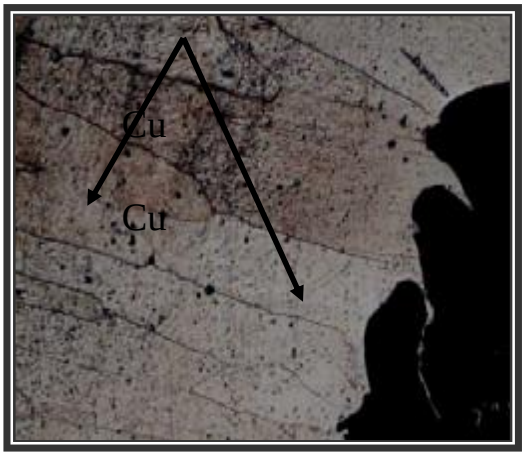

Figure (9-b)

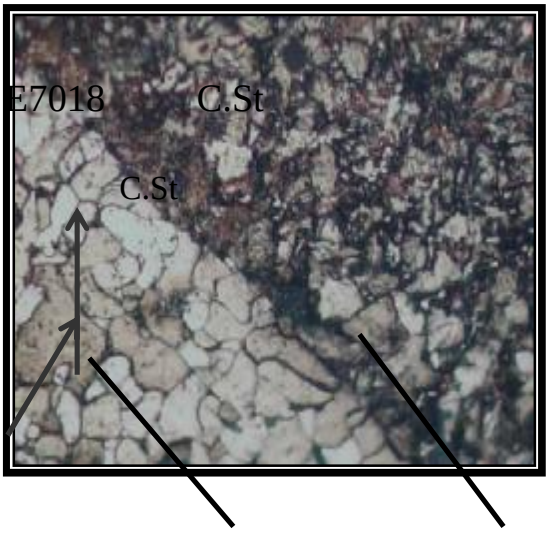

Interface

Figure(9-c)

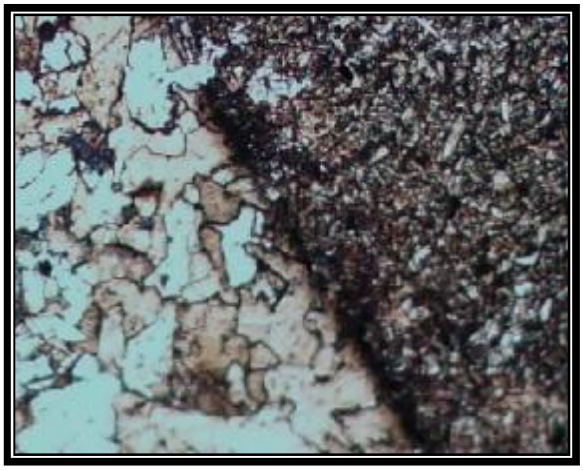

Ferrite

Figure (9-d)

Figure (9) .Cu/C.St system with E7018,SMAW, (a) Cu base metal, X 108, (b)Cu interface with E7018, X 108.(c,d) C.St interface with E7018, X 270.

3.2 ERNiCu-7 weld deposits

The nonepitaxial solidification had appear at the interface zone of copper/filler as shown in figure 10 c , d . The characteristics of this type of solidification is a copper grain structure parallel to the fusion line, which show a transion stage between the new structure of copper and the deposite . Figure 10 – e shows a micro crack due to solidification cracking which occurs when partitioning of elements during solidification causes low melting point films to form along solidification grain boundaries . As the weld metal cools and shrinks , a level of strain will develop and causes separation of the grain boundary along the liquid films . This type of cracking usually appears along the weld centerline , especially in a thick or heavily restrained weldment , and its occur immediately after welding [8] . This cracks will brazed immeadiatly because of presence an elements have low melting point will act as brazing filler to weld this cracks .

3.3 ECuSn-A weld deposits

Epiazial nucleation was appear from the copper side as shown in figure 11 – a , while showing nonepitaxial nucleation from the steel side . (Figure 11 b – c) .

3.4 E309L welded deposits

Nonepitaxial nucleation and hot cracking with brazing process was pointed out at the steel/ filler side . (figure 12 a ,b, c) . While shows competitive growth in bulk fusion zone of copper / filler side (figure 12-d, e and f) .

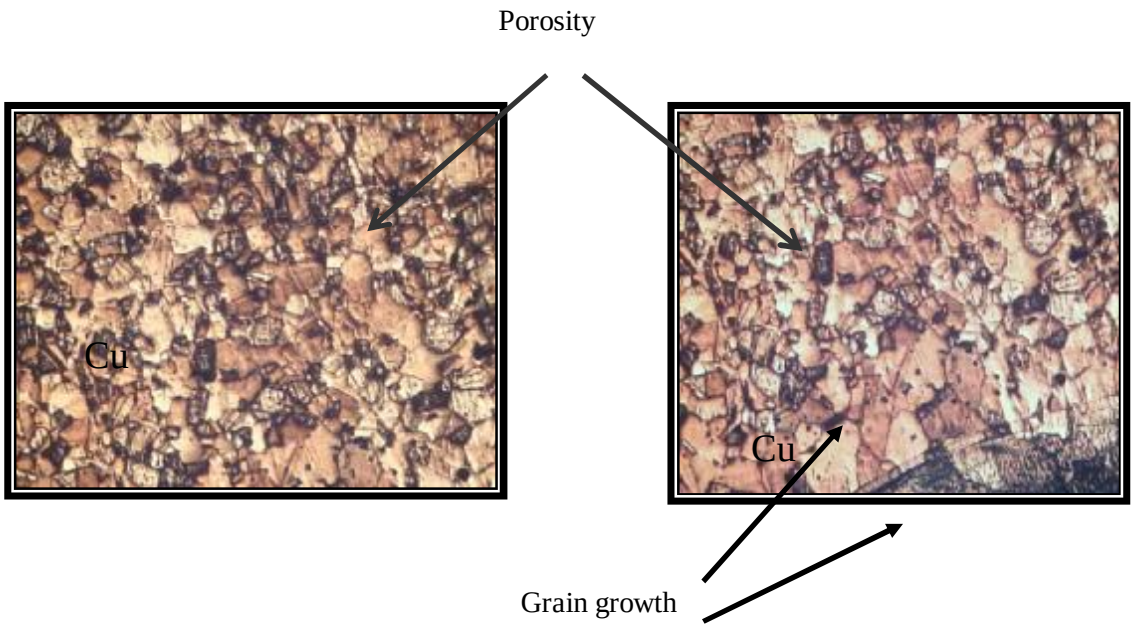

Figure (10- a) **Figure (10-b)**

Figure (10). Cu / C.St system with ER NiCu-7, GTAW. (c, d) Cu interface with ERNiCu-7, X 108. (e) C.St interface with ERNiCu-7, X 270. (f) C.St base metal, X 270.

Grain growth

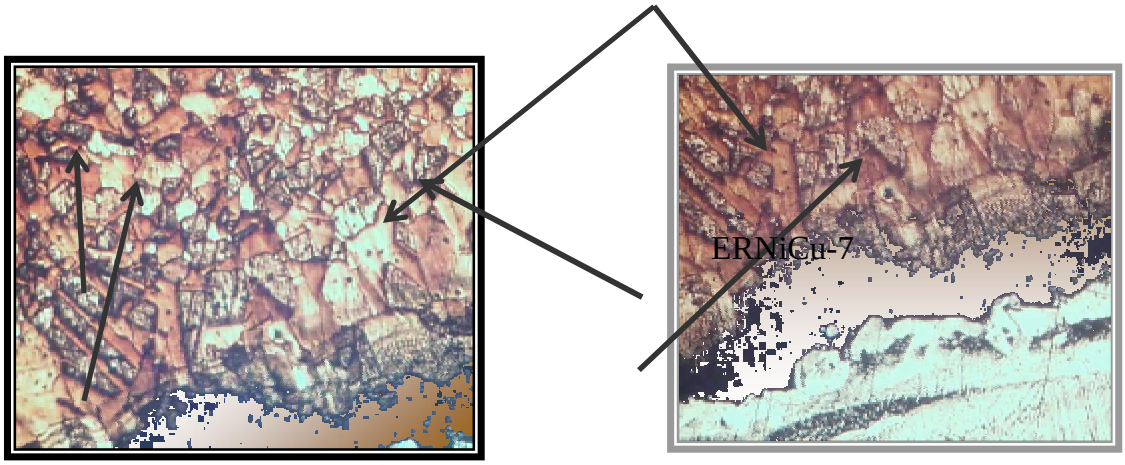

Twin band

Nonepitaxail

Figure (10-c)

Figure (10- d)

Crack

ferrite

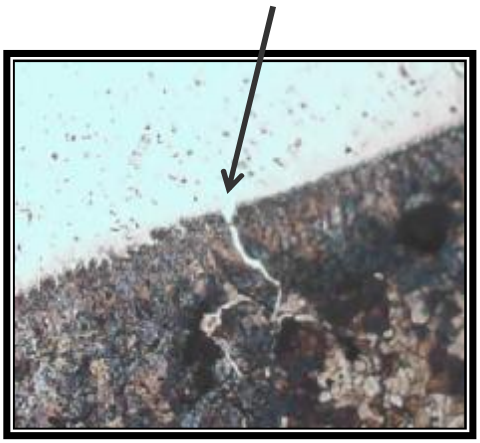

Figure (10- e)

Figure (10- f)

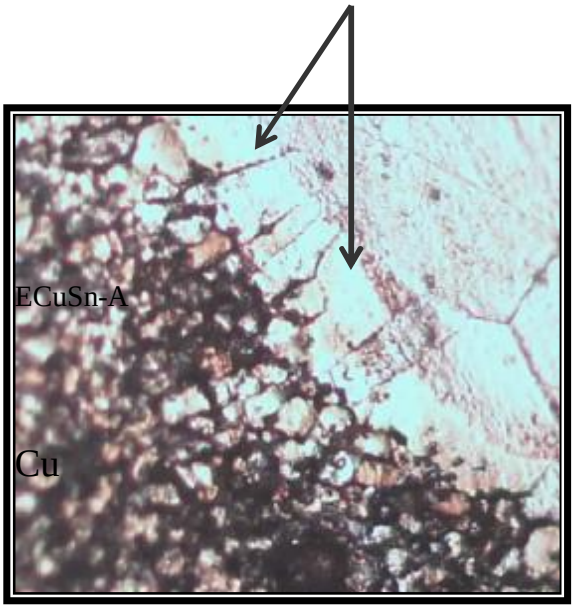

Figure (11- a)

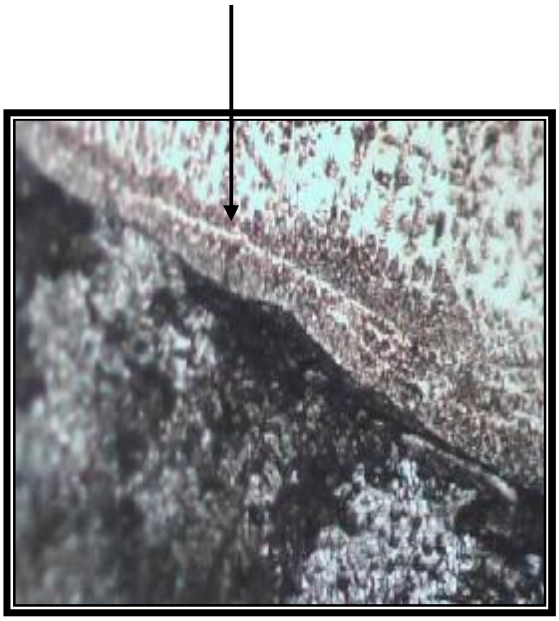

Figure (11- b)

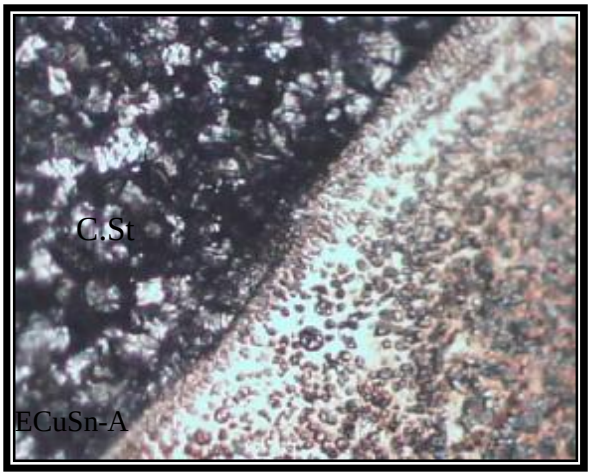

Figure (11- c)

Figure (11- d)

Figure(11). Cu/C.St system with ECuSn-A,SMAW,(a)Cu interface with ECuSn,X 108.(b,c) C.St interface with ECuSn-A, X 108. (d)C.St base metal, X 270.

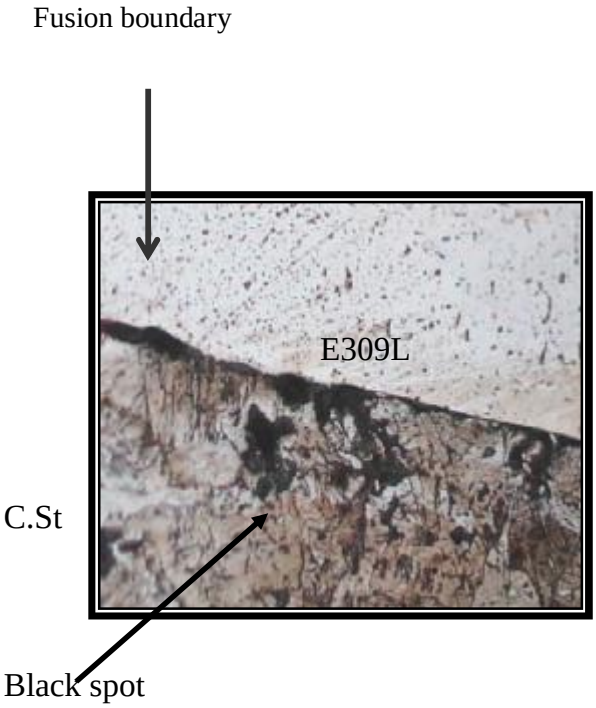

Figure (12- a)

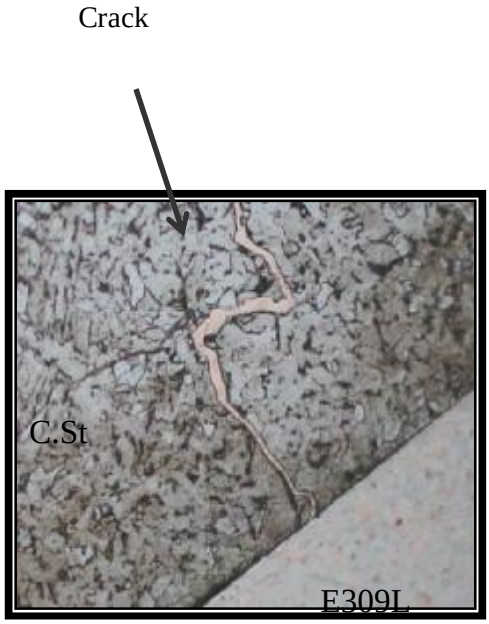

Figure (12- b)

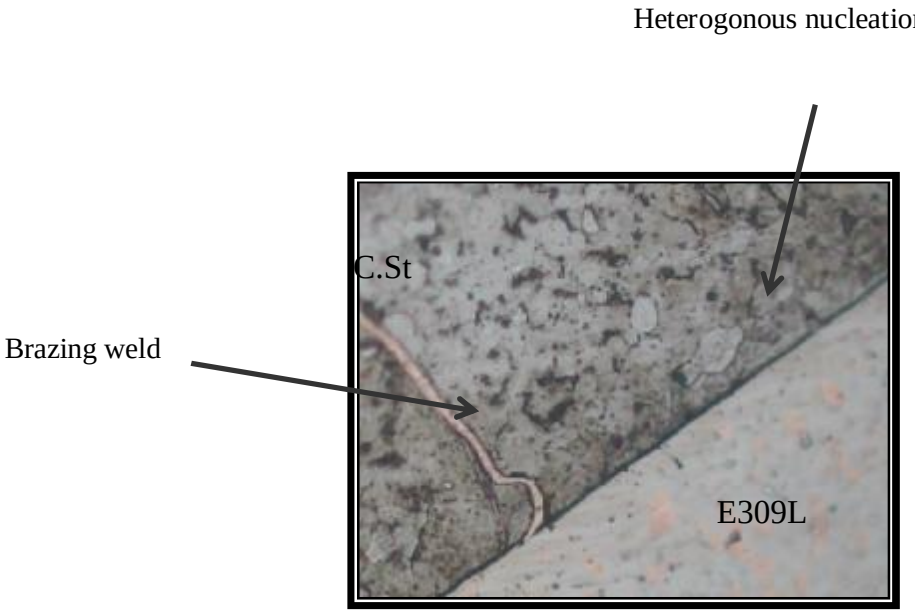

Figure (12- c)

Figure (12). Cu/ C.St system with E309L, SMAW. (a, b) C.St interface with E309L, X 108 .(c) C.St interface with E309L, X 270.

3.5 ECuweld deposits

The same welding mechanisms be shown with this filler , that an nonepitaxial nucleation with brazing action at the steel / filler side , while an competitive epitaxial growth from the copper / filler side . This clearly shown in the figure 13 , a , b and c for steel side , and 13-d , e , f and g for copper side .

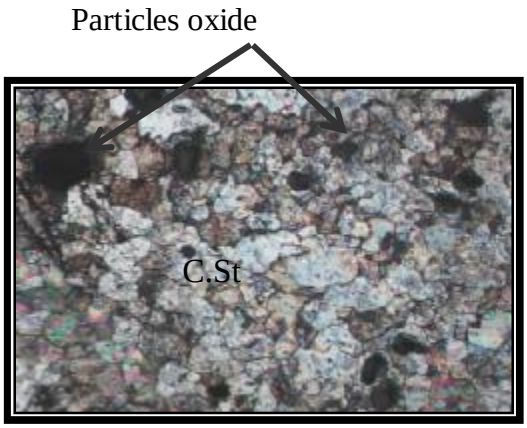

Heterogeneous nucleation

Figure (13- a)

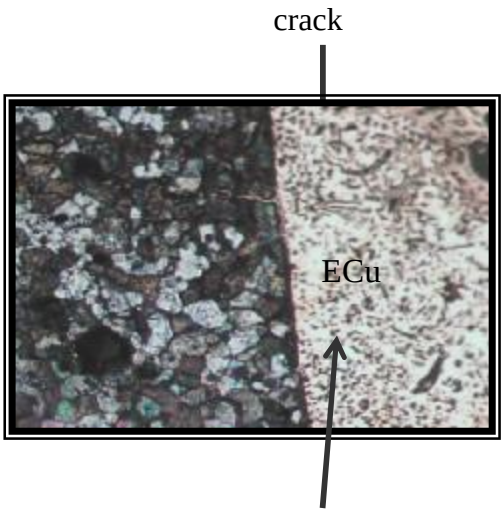

Figure (13-b)

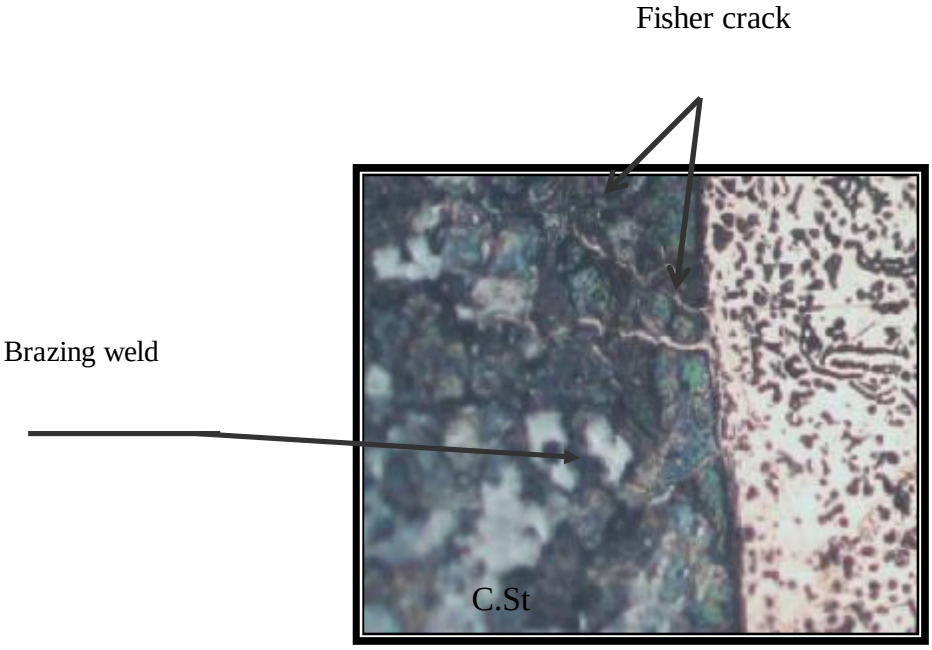

Figure (13- c)

Figure (13). Cu/ C.St with ECu, SMAW. (a) ECu ,weld metal, X 108, (e)Cu interface with ECu,X 108 . (f)Cu interface with ECu, X 270. (g) Cu base metal, X 108.

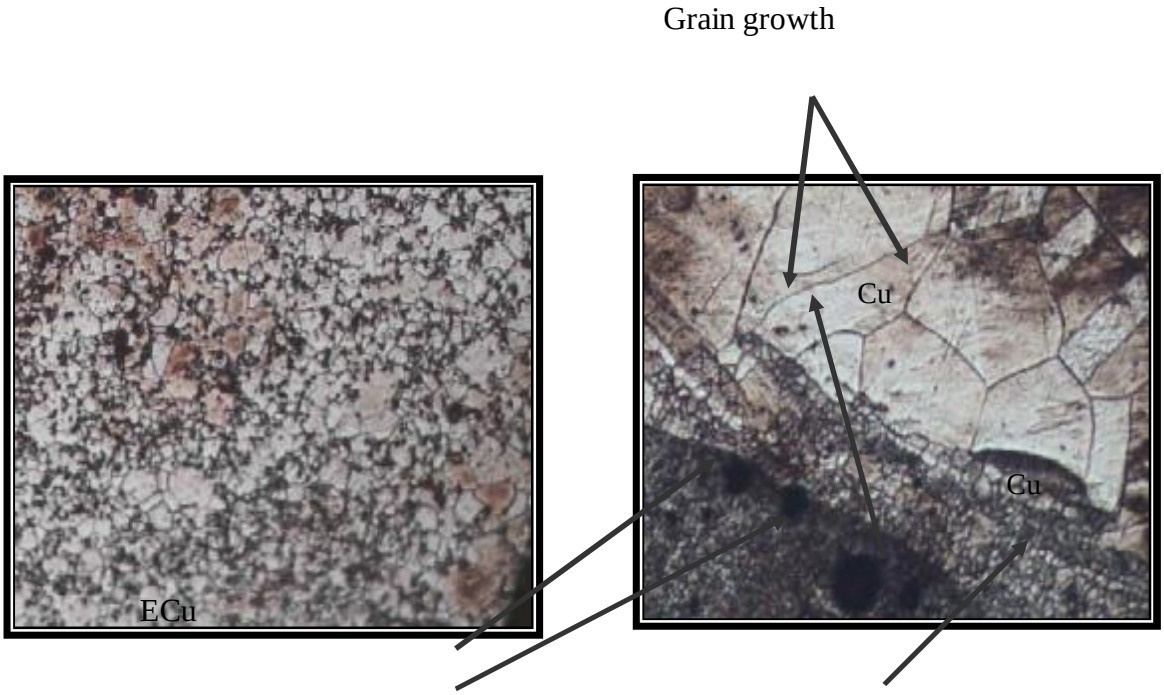

Figure (13- d) **Figure (13- e)**

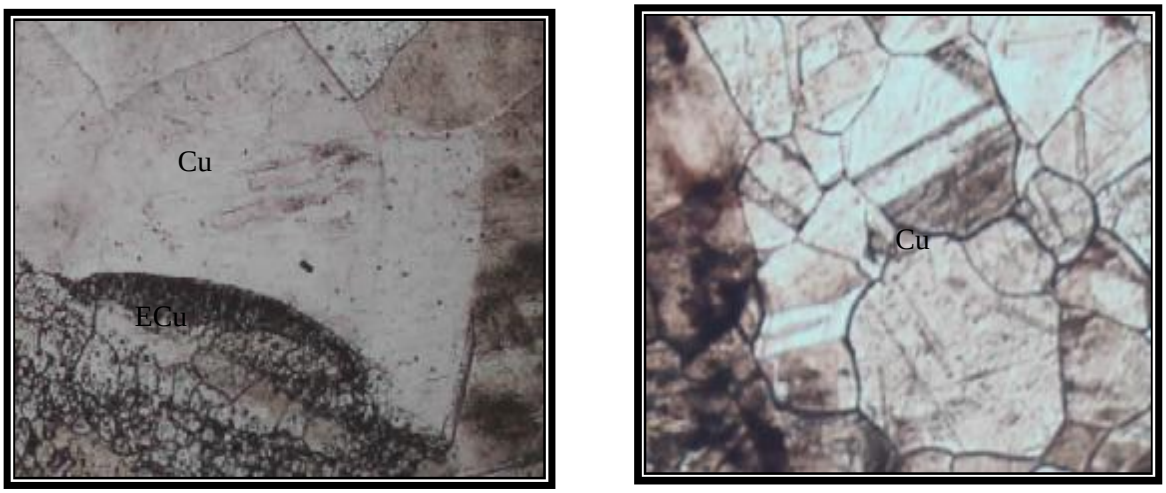

Figure (13- f) **Figure (13- g)**

3.6 E312 Weld Deposits

Figure(14,b)shows an competitive growth in fusion line from the copper side, while filler / copper interface show hetrogenous nucleation with some of dissolution of E312 filler as appear in figure (4 , c).

3.7 ENi-1 Weld Deposits

This filler show excessive dissolution at the copper side with competitive epitaxial growth , while nonepitaxial nucleation from the steel side as shown in figure (15).

Equaixed columnar crystal

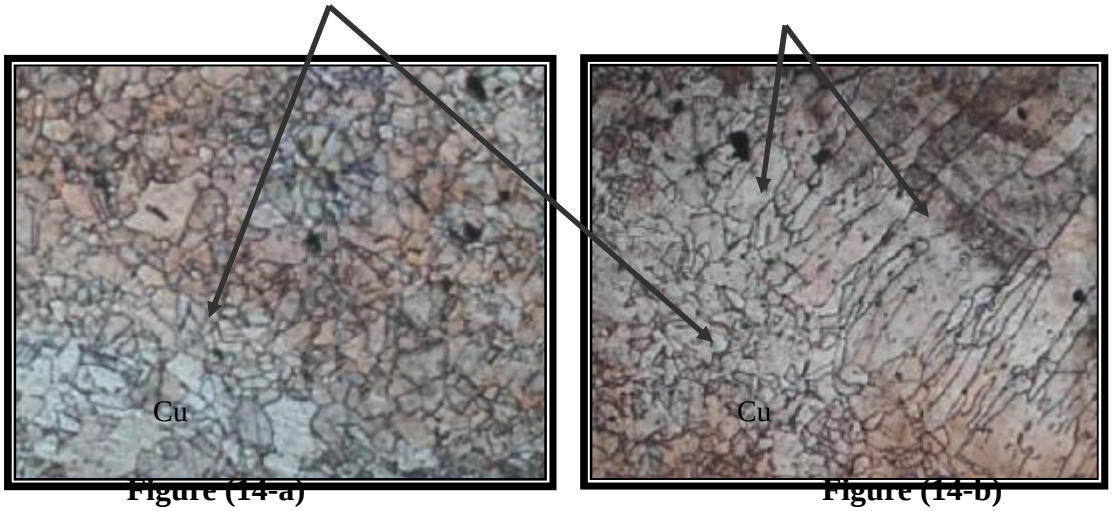

Figure (14-a) **Figure (14-b)**

Epitaxail solidification

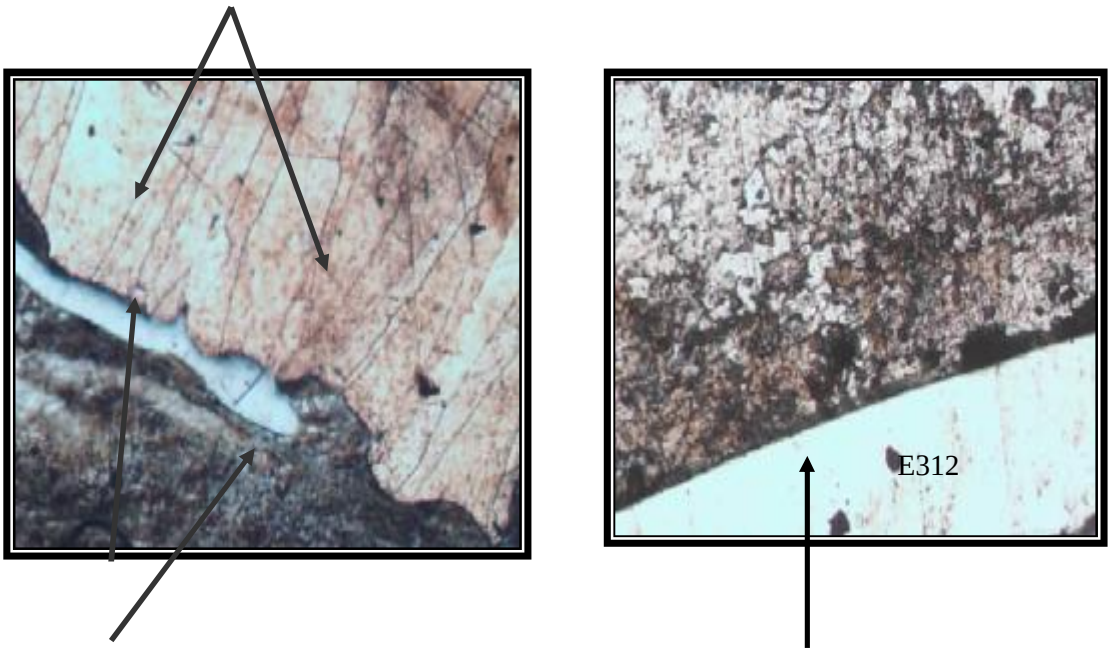

Dissolution for E312 Heterogeneous nucleation

Figure (14-c) **Figure (14-d)**

Figure (14). Cu/C.St with E312, SMAW. (a, b) Cu base metal, X 108. (c) Cu interface with E312, X 108. (d) C.St interface with E312, X 108.

3.8 ERNiCrFe-5 Weld Deposits

This filler shows an hetrogenous nucleation from both sides , copper / filler and steel / filler as appear clearly in figure 16 . Some dissolution of this filter in copper side will help to produce nonpitaxial solidification as in figure 16 – e .

3.9 Results of Tensile and Bend Test

The results obtained from the tensile and bending tests are equal the properties of copper , this result document that welding procedure is well because that all failure happen at copper side as shown in the figure (17 and 18), which represent the properties of copper . While bending shows no difference in bending properties for all joints (Figure 19 and 20) .

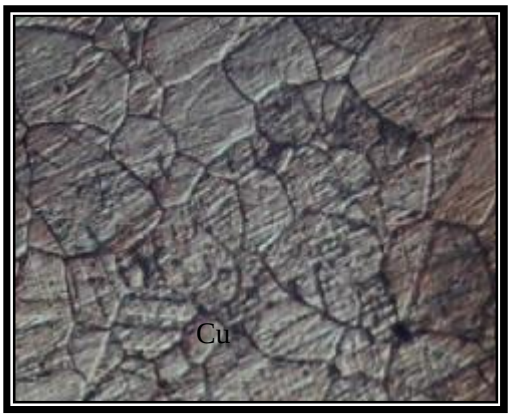

Figure (15-a)

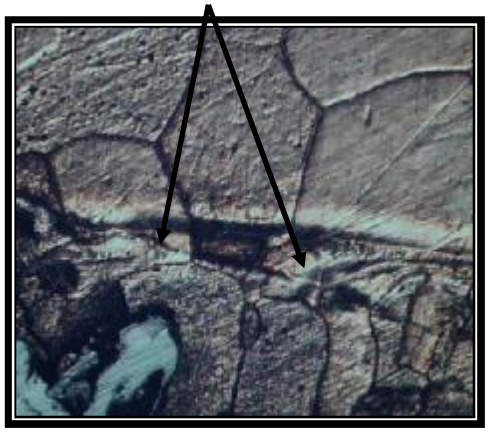

Figure (15-b)

Figure (15). Cu/C.St with E Ni-1, SMAW.(a)Cu base metal ,X 108.(b,c,d)Cu interface with ENi-1,X 108.

Competitive solidification

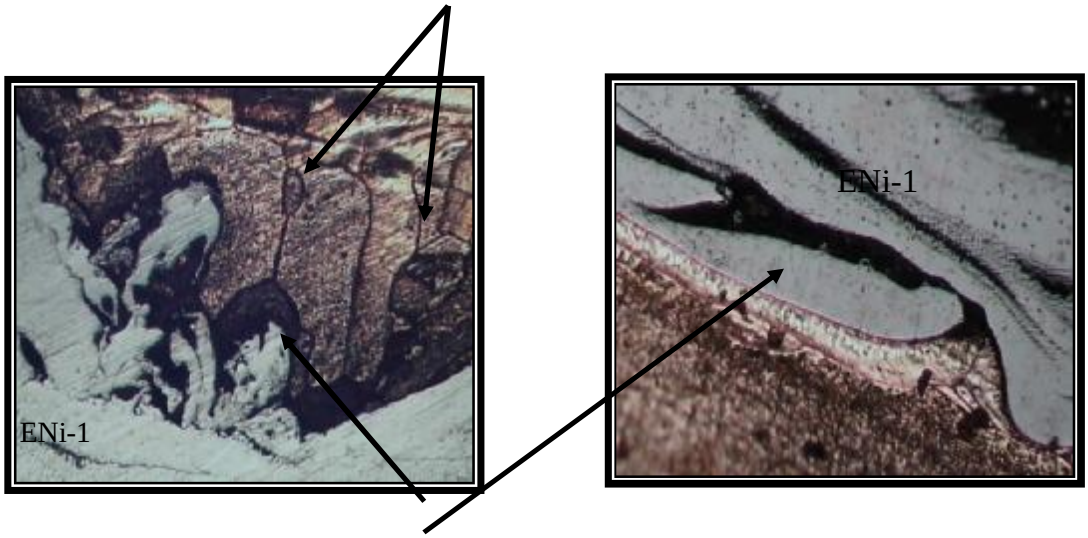

Figure (15-c) Dissolution for ENi-1 **Figure (15**-d)

Ferrite particleoxide

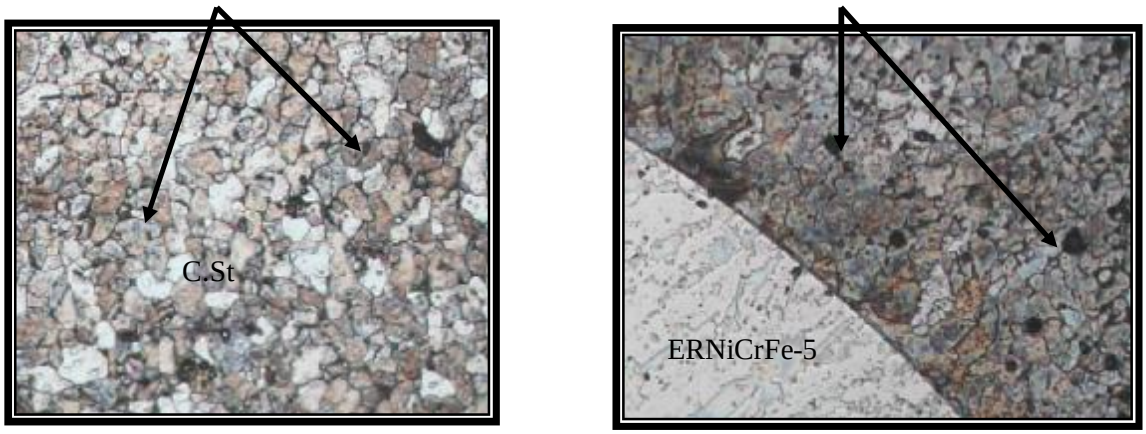

Figure (16-a) **Figure (16-b)**

Figure (16). Cu/C.St with ER NiCrFe-5, GTAW.(e) Cu interface with ERNiCrFe-5, X 108.(f) Cu base metal , X 108.

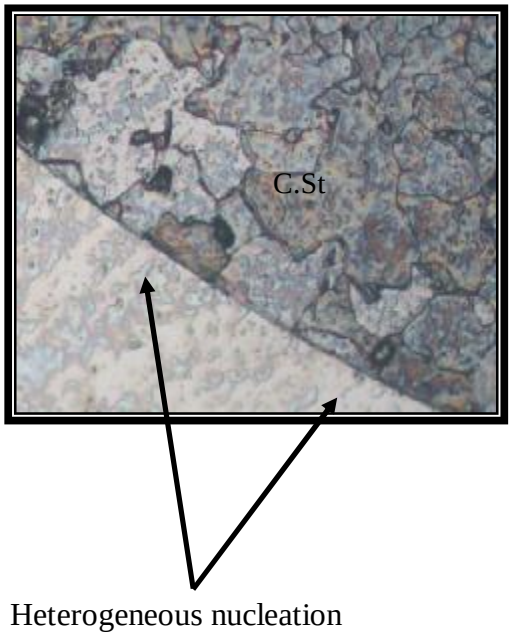

Figure (16-c)

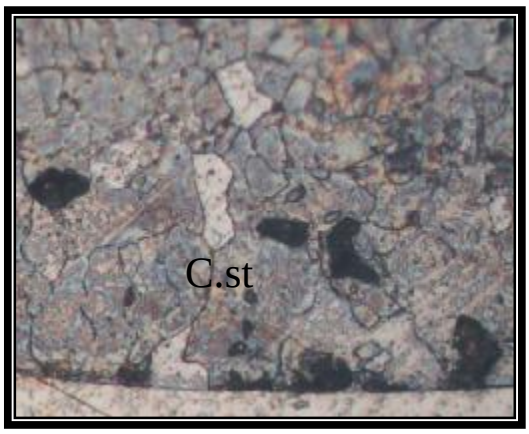

Figure (16-d)

Nonepitaxail solidification

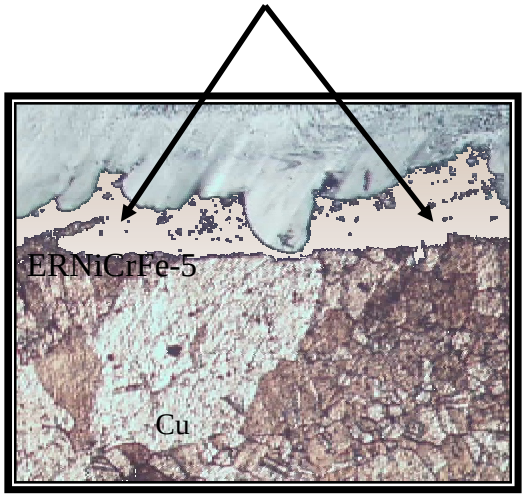

Figure (16-e)

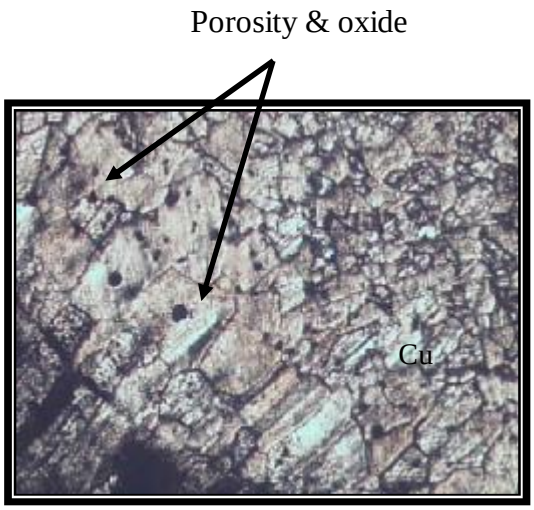

Figure (16-f)

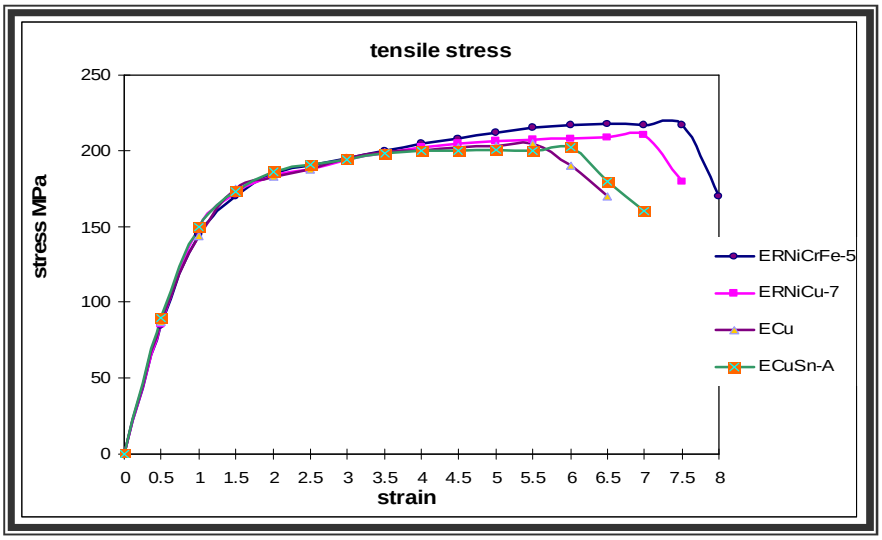

Figure (17). Tensile test data for copper / steel weldments by SMAW and GTAW processes using different filler metals (FMA).

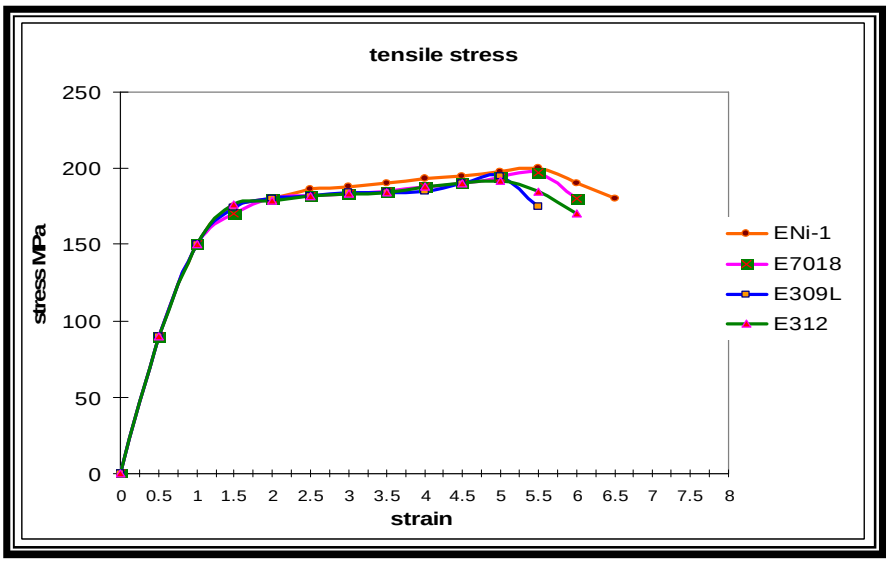

Figure (18). Tensile test data for copper / steel weldments by SMAW and GTAW processes using different filler metals (FMA).

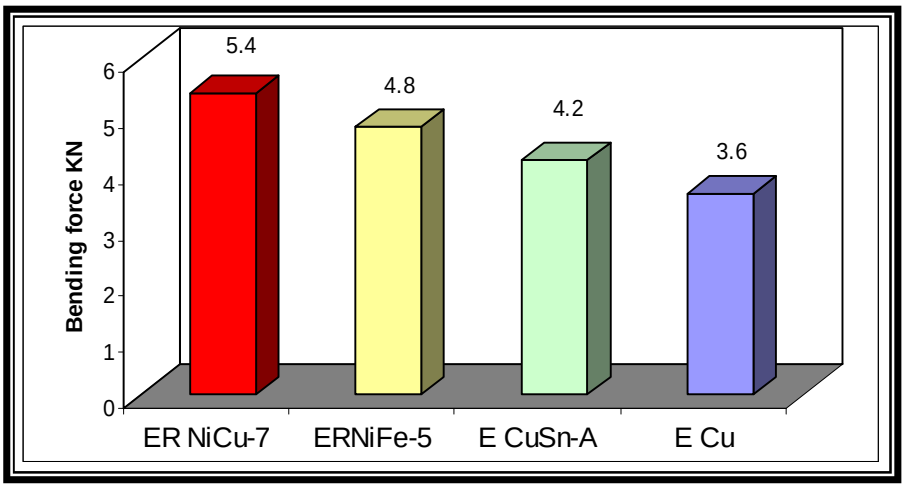

Figure (19). Bending test data for copper / steel weldments by SMAW and GTAW processes using different filler metals (FMA).

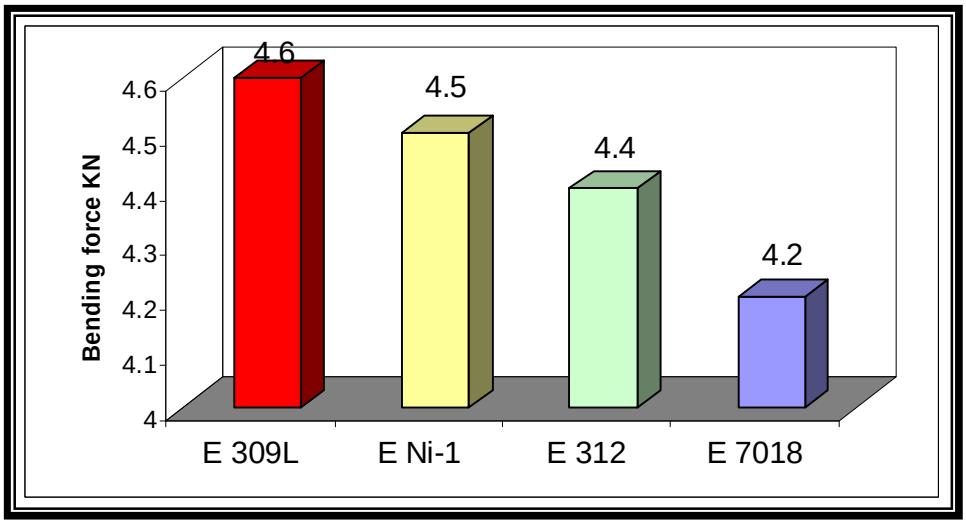

Figure (20). Bending test data for copper / steel weldments by SMAW and GTAW processes using different filler metals (FMA).

3.10 Bonding Mechanism

From joining of copper/steel system by using arc welding (SMAW and GTAW) , the bonding mechanism is as follows :

A. The arc is causing high dissolution or high mobility between dissimilar metals .

B. Because these metals are dissimilar , there is low affinity between them as compare with same filler / metal . This will results in segregation or separation between the mixed weld .

C. This will result and create a hot cracks (solidification cracks) almost at steel side .

D. Cracks will filled by copper liquid in a process like brazing .

E. Brazing happens after steel has solidified , then brazing start because part of filler and copper are not yet solidified .

F. The final stage is the closing of steel side cracks by capillary action of brazing causing the returned of strength of the joint .

4. Conclusions

Joining of copper and steel can be accomplished by using different electrodes by using SMAW and GTAW processes . Different solidification types can happen when using different filler and different welding processes .

Solidification cracks appear on the steel side of the weld when using any of the three following electrode ERNiCu-7 , E-309L , and ECu .

Brazing welds happen after steel solidification , the brazing mechanism takes place because the filler / copper have not yet solidified .

Brazing process is an intermediate process that helps strength to return to weld joints .

5. References

[1] Sindo Kou , 2003 ," Welding Metallurgy " 2nd Edition , John Wiley and Sons Inc. , Hoboken , New Jersy .

[2] Nelson . W. , Lippold . J. C, and Mills M. J. ,2000 , " Mature and Evolution of the Fusion Boundary in Ferritic – Austenitic Dissimilar Metal Welds- part 2 : On-colling Transformations " , WJ, Vol. 79 , No. 10 .

[3] Granjon H. ,1998," Fundamentals of Welding Metallurgy " , Naveen , Shashdara Delhi , Second Edition .

[4] The procedure Handbook of Arc Welding , 12th Editions , The Lincoln Company of Canada LTD , 1973 .

[5] ASME , Section 11 , Part C , Specification for Welding Rods , Electrodes , and Filler Metals , Edition July 1998 .

[6] ESAB , Welding Handbook , Consumables for Manual and Automatic Welding , 6th Edition , 2001 .

[7] ASME , " Section IX , Qualification Standard for Welding and Brazing Procedures , 1989.

[8] Rowe M. P. Crook , and Hoback G. L. , " Weldability of a corrosion Resistance NiCrMoCu Alloy " , W. J. , Vol. 82 , Na 11 , 2003 .

Controlling and Reducing Hazard Exposure to Hand Power Tools Vibration

Kadhim Karim Muhsin

Mechanical Engineering Department

College of Engineering

Thi-Qar University

Abstract

This paper investigates the combination of hand arm response and the vibration of hand power tools. The model of the hand power tools used in this paper to analyse cumulative sequences from the excitation during the operation is the jack hammer. The user subjected to many diseases during operation of the 'jack hammer such as (sever pain, numbness, pins, needles, loss of sense, and touch, loss of grip strength and painful wrist) .These diseases caused from the successive high amplitudes of vibration transferred from the jack hammer to the hand arm of the user. Results are presented to study the relationship between the excitation and the response of the system with the aid of Ansys program to give the indications of Eigen values and Eigen vectors deformation, to predict the behavior of hand-arm vibration, to control the risks from the vibration of the tool. This indicates that the high amplitudes of the jack hammer can be minimized by adding the dynamic vibration absorber which is a simply-spring mass system to the original mass system to make the system to two degree of freedom system and the entire system will have two Eigen values one above the excitation and the other under the excitation and this leads to eliminate the higher response and will have very small amplitude instead of very large amplitude to protect the users from the risks of hand arm vibration during the operation.

Keywords: Hand-transmitted vibration, risk-assessments, construction tools.

السيطرة وتقليل التعرض لخطر الاهتزاز في ذراع اليد الناتج عن اجهزة العمل اليدوية الاهتزازية

المستخلص

يدرس هذا البحث العلاقة بين استجابة ذراع اليد واجهزة العمل اليدوية الاهتزازية حيث ان النموذج الرياضي المستخدم في هذا البحث يقوم بتحليل الاهتزاز المتعاقب التراكمي الناتج عن الاثارة اثناء اشتغال الجهاز المستعمل في هذه الدراسة وهو "الجك همر" حيث يتعرض المشغل الى العديد من المشاكل مثل (الام حادة في الذراع ,خدر الاصابع, فقدان الحس واللمس , قبضة يد مؤلمة وفقدان التحسس) هذه المشاكل ناجمة من السعات العالية المتتالية المنقولة من الجك همر الى الذراع حيث ان النتائج النظرية التي عرضت تم استخدامها لدراسة العلاقة بين الاثارة والاستجابة للمنظومة بمساعدة لبيان المؤشرات التي تعطي الترددات الطبيعية والنسوق والتشوهات المرنة وذلك للتنبؤ بسلوك الذراع Ansys برنامج المعرض الى الاهتزازات للسيطرة على المخاطر الناجمة من ادوات الاهتزاز حيث تم الاستنتاج الى انه يمكن تقليل السعة العالية للجك همر باضافة جهاز الامتصاص الديناميكي للاهتزازات الذي هو عبارة عن منظومة بسيطة مكونة من نابض وكتلة (منظومة ذات درجة حرية واحدة) الى المنظومة الاصلية لتحويله الى منظومة ذات درجتي حرية حركة وبالتالي يمتلك النظام باكملة ترددين طبيعين احدهما اعلى من تردد الاثارة والاخر ادنى من تردد الاثارة وهذا يؤدي الى الغاء السعة العالية ويكون النظام ذو سعة صغيرة جداً بدلاً من السعة الكبيرة جدا لحماية المستخدمين من مخاطر الاهتزاز خلال عمل الجهاز.

1. Introduction

Hand-arm vibration is a vibration transmitted from work processes into workers' hands and arms. It can be caused by operating hand-held power tools, such as road breakers, and hand-guided equipment, such as powered lawnmowers, or by holding materials being processed by machines, such as pedestal grinders [1, 2]

Jack hammer have been in use for years and are utilized to break up concrete, asphalt and other hard material .A conventional jackhammer is powered by compressed air and emits a significant amount of vibration to the operator .This continued vibration can result in fatigue and possible injury to the operator of the jack hammer .Hence .there is a need for a jackhammer that has a significantly reduced vibration for the operator [3,4].

2. Model analysis

The model used in the present study is the "jack hammer" as shown in figure (1).

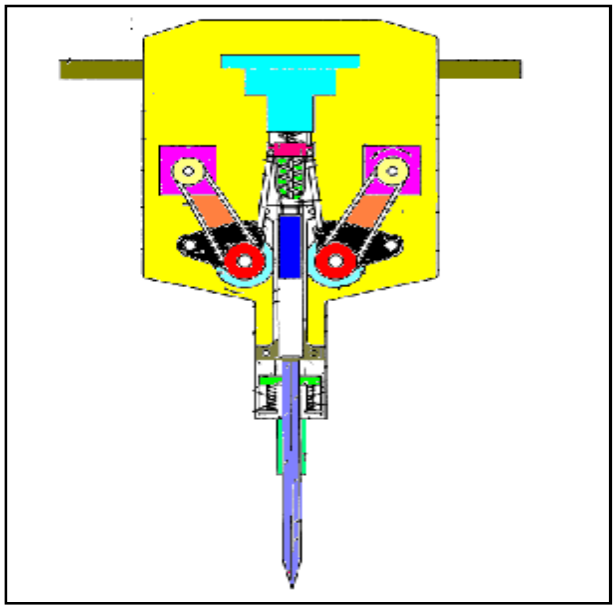

Figure(1).Jack hammer geometry [3].

The general equations modeling the multi-degree system of the Systematic representation of jack hammer shown in Figure (2).

$$m_1\ddot{x}_1+(c_1+c_2+c_3+c_4)\dot{x}_1-c_3\dot{x}_2-c_4\dot{x}_3+(k_1+k_2+k_3+k_4+k_5+k_6)x_1+(k_3+k_4)x_2-(k_5+k_6)x_3=F_0\,sin\omega t \quad (1)$$

$$m_2\ddot{x}_2+(c_3+c_5)\dot{x}_2-c_3\dot{x}_1-c_5\dot{x}_4+(k_3+k_4+k_7)x_2-(k_3+k_4)-c_7\dot{x}_4=0 \quad (2)$$

$$m_3\ddot{x}_3+(c4+c6)\dot{x}_3-c4\dot{x}_1-c_6\dot{x}_4+(k3+k6+\ddot{}k8)x_3-(k5+k6)x_1-k8x_4=0 \quad (3)$$

$$m_4\ddot{x}_4+(c_5+c_6+c_7)\dot{x}_4-c_5\dot{x}_2-c_6\dot{x}_3+(k_7+k_8+k_9+k_{10})x_4-k_7x_2-k_8x_3-(k_9+k_{10})x_5-c_7\dot{x}_5=0 \quad (4)$$

$$m_5\ddot{x}_5+(c_7+c_8)\dot{x}_5-c_7\dot{x}_4-c_8\dot{x}_6+(k_9+k_{10}+k_{11})x_5-(k_9+k_{10})x_4-k_{11}x_6=0 \quad (5)$$

$$m_6\ddot{x}_6+c_8\dot{x}_6-c_8\dot{x}_5+k_{11}x_6-k_{11}x_5=0 \quad (6)$$

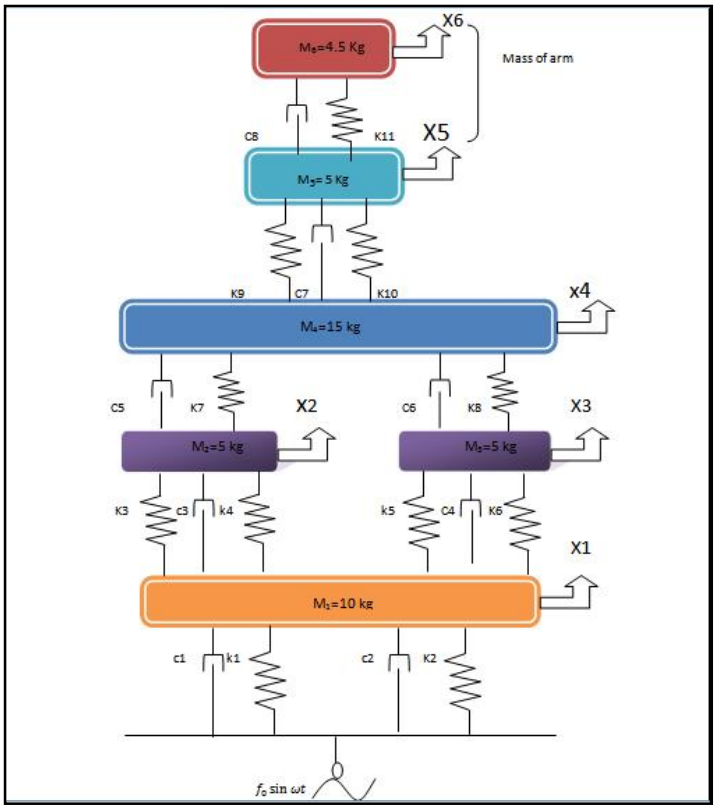

Figure(2). Systematic representation of jack hammer.

Putting equations (1-6) in matrix form

$$\begin{bmatrix} m_1 & 0 & 0 & 0 & 0 & 0 \\ 0 & m_2 & 0 & 0 & 0 & 0 \\ 0 & 0 & m_3 & 0 & 0 & 0 \\ 0 & 0 & 0 & m_4 & 0 & 0 \\ 0 & 0 & 0 & 0 & m_5 & 0 \\ 0 & 0 & 0 & 0 & 0 & m_6 \end{bmatrix} \begin{Bmatrix} \ddot{x}_1 \\ \ddot{x}_2 \\ \ddot{x}_3 \\ \ddot{x}_4 \\ \ddot{x}_5 \\ \ddot{x}_6 \end{Bmatrix} +$$

$$\begin{bmatrix} c_1+c_2+c_3+c_4 & -c_3 & -c_4 & 0 & 0 & 0 \\ -c_3 & c_3+c_5 & 0 & 0 & 0 & 0 \\ -c_4 & 0 & c_4+c_6 & -c_6 & 0 & 0 \\ 0 & -c_5 & -c_6 & c_5+c_6 & -c_7 & 0 \\ 0 & 0 & 0 & -c_7 & c_7+c_8 & -c_8 \\ 0 & 0 & 0 & 0 & -c_8 & c_8 \end{bmatrix} \begin{Bmatrix} \dot{x}_1 \\ \dot{x}_2 \\ \dot{x}_3 \\ \dot{x}_4 \\ \dot{x}_5 \\ \dot{x}_6 \end{Bmatrix} +$$

$$\begin{bmatrix} k_1+k_2+k_3+k_4+k_5+k_6 & -(k_3+k_4) & -(k_5+k_6) & 0 & 0 & 0 \\ -(k_3+k_4) & k_3+k_4+k_7 & 0 & -k_7 & 0 & 0 \\ -(k_5+k_6) & 0 & k_3+k_6+k_8 & -k_8 & 0 & 0 \\ 0 & -k_7 & -k_8 & k_7+k_8+k_9+k_{10} & -k_9-k_{10} & 0 \\ 0 & 0 & 0 & -k_9-k_{10} & k_9+k_{10}+k_{11} & -k_{11} \\ 0 & 0 & 0 & 0 & -k_{11} & k_{11} \end{bmatrix}$$

$$\begin{Bmatrix} x_1 \\ x_2 \\ x_3 \\ x_4 \\ x_5 \\ x_6 \end{Bmatrix} = \begin{bmatrix} f_0 \\ 0 \\ 0 \\ 0 \\ 0 \\ 0 \end{bmatrix} \qquad (7)$$

Mode shapes

The equation of mode shape depended upon the matrixes of stiffness, the stiffness coefficient and determinate as [5-8]:

$$\phi_{ij} = \frac{k_{ij}^{cT}}{|D|} F_o$$

$$[k_{ij}] = \begin{bmatrix} k_{11} & k_{12} & k_{13} & k_{14} & k_{15} & k_{16} \\ k_{21} & k_{22} & k_{23} & k_{24} & k_{25} & k_{26} \\ k_{31} & k_{32} & k_{33} & k_{34} & k_{35} & k_{36} \\ k_{41} & k_{42} & k_{43} & k_{44} & k_{45} & k_{46} \\ k_{51} & k_{52} & k_{53} & k_{54} & k_{55} & k_{56} \\ k_{61} & k_{62} & k_{63} & k_{64} & k_{65} & k_{66} \end{bmatrix} \quad (8)$$

The matrix stiffness coefficients

$$[k_{ij}^{c}] = \begin{bmatrix} k_{11}^{c} & k_{12}^{c} & k_{13}^{c} & k_{14}^{c} & k_{15}^{c} & k_{16}^{c} \\ k_{21}^{c} & k_{22}^{c} & k_{23}^{c} & k_{24}^{c} & k_{25}^{c} & k_{26}^{c} \\ k_{31}^{c} & k_{32}^{c} & k_{33}^{c} & k_{34}^{c} & k_{35}^{c} & k_{36}^{c} \\ k_{41}^{c} & k_{42}^{c} & k_{43}^{c} & k_{44}^{c} & k_{45}^{c} & k_{46}^{c} \\ k_{51}^{c} & k_{52}^{c} & k_{53}^{c} & k_{54}^{c} & k_{55}^{c} & k_{56}^{c} \\ k_{61}^{c} & k_{11}^{c} & k_{63}^{c} & k_{64}^{c} & k_{65}^{c} & k_{66}^{c} \end{bmatrix} \quad (9)$$

The cofactor transpose of the stiffness matrix

$$[k_{ij}^{c}]^{T} = \begin{bmatrix} k_{11}^{c} & k_{21}^{c} & k_{31}^{c} & k_{41}^{c} & k_{51}^{c} & k_{61}^{c} \\ k_{12}^{c} & k_{22}^{c} & k_{32}^{c} & k_{42}^{c} & k_{52}^{c} & k_{62}^{c} \\ k_{13}^{c} & k_{23}^{c} & k_{33}^{c} & k_{43}^{c} & k_{53}^{c} & k_{63}^{c} \\ k_{14}^{c} & k_{24}^{c} & k_{34}^{c} & k_{44}^{c} & k_{54}^{c} & k_{64}^{c} \\ k_{15}^{c} & k_{25}^{c} & k_{35}^{c} & k_{45}^{c} & k_{55}^{c} & k_{65}^{c} \\ k_{16}^{c} & k_{26}^{c} & k_{36}^{c} & k_{46}^{c} & k_{56}^{c} & k_{66}^{c} \end{bmatrix} \quad (10)$$

The Eigen vectors of the system are:

$$\phi_{11}=\frac{[k_{11}^c]^T}{|D|}f_0 \quad \phi_{12}=\frac{[k_{21}^c]^T}{|D|}f_0 \phi_{13}=\frac{[k_{31}^c]^T}{|D|}f_0 \quad \phi_{14}=\frac{[k_{41}^c]^T}{|D|}f_0$$

$$\phi_{15}=\frac{[k_{51}^c]^T}{|D|}f_0 \quad \phi_{16}=\frac{[k_{61}^c]^T}{|D|}f_0 \phi_{21}=\frac{[k_{21}^c]^T}{|D|} \quad \phi_{22}=\frac{[k_{22}^c]^T}{|D|}$$

$$\phi_{23}=\frac{[k_{32}^c]^T}{|D|} \phi_{24}=\frac{[k_{42}^c]^T}{|D|} \quad \phi_{25}=\frac{[k_{52}^c]^T}{|D|} \quad \phi_{26}=\frac{[k_{62}^c]^T}{|D|}$$

$$\phi_{31}=\frac{[k_{13}^c]^T}{|D|} \phi_{32}=\frac{[k_{23}^c]^T}{|D|} \quad \phi_{33}=\frac{[k_{33}^c]^T}{|D|} \quad \phi_{34}=\frac{[k_{43}^c]^T}{|D|}$$

$$\phi_{35}=\frac{[k_{53}^c]^T}{|D|} \phi_{36}=\frac{[k_{63}^c]^T}{|D|} \quad \phi_{41}=\frac{[k_{14}^c]^T}{|D|} \quad \phi_{42}=\frac{[k_{24}^c]^T}{|D|}$$

$$\phi_{43}=\frac{[k_{34}^c]^T}{|D|} \phi_{44}=\frac{[k_{44}^c]^T}{|D|} \quad \phi_{45}=\frac{[k_{54}^c]^T}{|D|} \quad \phi_{46}=\frac{[k_{64}^c]^T}{|D|}$$

$$\phi_{51}=\frac{[k_{15}^c]^T}{|D|} \phi_{52}=\frac{[k_{25}^c]^T}{|D|} \quad \phi_{53}=\frac{[k_{35}^c]^T}{|D|} \quad \phi_{54}=\frac{[k_{45}^c]^T}{|D|}$$

$$\phi_{55}=\frac{[k_{55}^c]^T}{|D|} \phi_{56}=\frac{[k_{65}^c]^T}{|D|} \quad \phi_{61}=\frac{[k_{16}^c]^T}{|D|} \quad \phi_{62}=\frac{[k_{26}^c]^T}{|D|}$$

$$\phi_{63}=\frac{[k_{36}^c]^T}{|D|} \phi_{64}=\frac{[k_{46}^c]^T}{|D|} \quad \phi_{65}=\frac{[k_{56}^c]^T}{|D|} \quad \phi_{66}=\frac{[k_{66}^c]^T}{|D|} \qquad (11)$$

The modal matrix

$$\begin{bmatrix} \phi_{11} & \phi_{12} & \phi_{13} & \phi_{14} & \phi_{15} & \phi_{16} \\ \phi_{21} & \phi_{22} & \phi_{23} & \phi_{24} & \phi_{25} & \phi_{26} \\ \phi_{31} & \phi_{32} & \phi_{33} & \phi_{34} & \phi_{35} & \phi_{36} \\ \phi_{41} & \phi_{42} & \phi_{43} & \phi_{44} & \phi_{45} & \phi_{46} \\ \phi_{51} & \phi_{52} & \phi_{53} & \phi_{54} & \phi_{55} & \phi_{56} \\ \phi_{61} & \phi_{62} & \phi_{63} & \phi_{64} & \phi_{65} & \phi_{66} \end{bmatrix} \qquad (12)$$

The determinate$|D|$ can be determined by using Fortran power station program.

The natural frequencies of the system

$$\omega_{ij} = \frac{[\phi_{ij}]^T[k][\phi_{ij}]}{[\phi_{ij}]^T[m][\phi_{ij}]}$$

Transpose of the mode shape:

$$[\phi_{ij}]^T = \begin{bmatrix} \phi_{11} & \phi_{21} & \phi_{31} & \phi_{41} & \phi_{51} & \phi_{61} \\ \phi_{12} & \phi_{22} & \phi_{32} & \phi_{42} & \phi_{52} & \phi_{62} \\ \phi_{13} & \phi_{23} & \phi_{33} & \phi_{43} & \phi_{53} & \phi_{63} \\ \phi_{14} & \phi_{24} & \phi_{34} & \phi_{44} & \phi_{54} & \phi_{64} \\ \phi_{15} & \phi_{25} & \phi_{35} & \phi_{45} & \phi_{55} & \phi_{65} \\ \phi_{16} & \phi_{26} & \phi_{36} & \phi_{46} & \phi_{56} & \phi_{66} \end{bmatrix} \quad (13)$$

The natural frequencies of the system are:

$$\omega_1 = \frac{[\phi_{11} \quad \phi_{21} \quad \phi_{31} \quad \phi_{41} \quad \phi_{51} \quad \phi_{61}] \begin{bmatrix} k_{11} & k_{11} & k_{11} & k_{11} & k_{11} & k_{11} \\ k_{11} & k_{11} & k_{11} & k_{11} & k_{11} & k_{11} \\ k_{11} & k_{11} & k_{11} & k_{11} & k_{11} & k_{11} \\ k_{11} & k_{11} & k_{11} & k_{11} & k_{11} & k_{11} \\ k_{11} & k_{11} & k_{11} & k_{11} & k_{11} & k_{11} \\ k_{11} & k_{11} & k_{11} & k_{11} & k_{11} & k_{11} \end{bmatrix} \begin{bmatrix} \phi_{11} \\ \phi_{21} \\ \phi_{31} \\ \phi_{41} \\ \phi_{51} \\ \phi_{61} \end{bmatrix}}{[\phi_{11} \quad \phi_{21} \quad \phi_{31} \quad \phi_{41} \quad \phi_{51} \quad \phi_{61}] \begin{bmatrix} m_1 & 0 & 0 & 0 & 0 & 0 \\ 0 & m_2 & 0 & 0 & 0 & 0 \\ 0 & 0 & m_3 & 0 & 0 & 0 \\ 0 & 0 & 0 & m_4 & 0 & 0 \\ 0 & 0 & 0 & 0 & m_5 & 0 \\ 0 & 0 & 0 & 0 & 0 & m_6 \end{bmatrix} \begin{bmatrix} \phi_{11} \\ \phi_{21} \\ \phi_{31} \\ \phi_{41} \\ \phi_{51} \\ \phi_{61} \end{bmatrix}} \quad (14)$$

$$\omega_2 = \frac{[\phi_{12} \quad \phi_{22} \quad \phi_{32} \quad \phi_{42} \quad \phi_{52} \quad \phi_{62}] \begin{bmatrix} k_{11} & k_{11} & k_{11} & k_{11} & k_{11} & k_{11} \\ k_{11} & k_{11} & k_{11} & k_{11} & k_{11} & k_{11} \\ k_{11} & k_{11} & k_{11} & k_{11} & k_{11} & k_{11} \\ k_{11} & k_{11} & k_{11} & k_{11} & k_{11} & k_{11} \\ k_{11} & k_{11} & k_{11} & k_{11} & k_{11} & k_{11} \\ k_{11} & k_{11} & k_{11} & k_{11} & k_{11} & k_{11} \end{bmatrix} \begin{bmatrix} \phi_{12} \\ \phi_{22} \\ \phi_{32} \\ \phi_{42} \\ \phi_{52} \\ \phi_{62} \end{bmatrix}}{[\phi_{12} \quad \phi_{22} \quad \phi_{32} \quad \phi_{42} \quad \phi_{52} \quad \phi_{62}] \begin{bmatrix} m_1 & 0 & 0 & 0 & 0 & 0 \\ 0 & m_2 & 0 & 0 & 0 & 0 \\ 0 & 0 & m_3 & 0 & 0 & 0 \\ 0 & 0 & 0 & m_4 & 0 & 0 \\ 0 & 0 & 0 & 0 & m_5 & 0 \\ 0 & 0 & 0 & 0 & 0 & m_6 \end{bmatrix} \begin{bmatrix} \phi_{12} \\ \phi_{22} \\ \phi_{32} \\ \phi_{42} \\ \phi_{52} \\ \phi_{62} \end{bmatrix}} \quad (15)$$

$$\omega_3 = \frac{[\phi_{13} \quad \phi_{23} \quad \phi_{33} \quad \phi_{43} \quad \phi_{53} \quad \phi_{63}] \begin{bmatrix} k_{11} & k_{11} & k_{11} & k_{11} & k_{11} & k_{11} \\ k_{11} & k_{11} & k_{11} & k_{11} & k_{11} & k_{11} \\ k_{11} & k_{11} & k_{11} & k_{11} & k_{11} & k_{11} \\ k_{11} & k_{11} & k_{11} & k_{11} & k_{11} & k_{11} \\ k_{11} & k_{11} & k_{11} & k_{11} & k_{11} & k_{11} \\ k_{11} & k_{11} & k_{11} & k_{11} & k_{11} & k_{11} \end{bmatrix} \begin{bmatrix} \phi_{13} \\ \phi_{23} \\ \phi_{33} \\ \phi_{43} \\ \phi_{53} \\ \phi_{63} \end{bmatrix}}{[\phi_{13} \quad \phi_{23} \quad \phi_{33} \quad \phi_{43} \quad \phi_{53} \quad \phi_{63}] \begin{bmatrix} m_1 & 0 & 0 & 0 & 0 & 0 \\ 0 & m_2 & 0 & 0 & 0 & 0 \\ 0 & 0 & m_3 & 0 & 0 & 0 \\ 0 & 0 & 0 & m_4 & 0 & 0 \\ 0 & 0 & 0 & 0 & m_5 & 0 \\ 0 & 0 & 0 & 0 & 0 & m_6 \end{bmatrix} \begin{bmatrix} \phi_{13} \\ \phi_{23} \\ \phi_{33} \\ \phi_{43} \\ \phi_{53} \\ \phi_{63} \end{bmatrix}} \quad (16)$$

$$\omega_4 = \frac{[\phi_{14} \quad \phi_{24} \quad \phi_{34} \quad \phi_{44} \quad \phi_{54} \quad \phi_{64}] \begin{bmatrix} k_{11} & k_{11} & k_{11} & k_{11} & k_{11} & k_{11} \\ k_{11} & k_{11} & k_{11} & k_{11} & k_{11} & k_{11} \\ k_{11} & k_{11} & k_{11} & k_{11} & k_{11} & k_{11} \\ k_{11} & k_{11} & k_{11} & k_{11} & k_{11} & k_{11} \\ k_{11} & k_{11} & k_{11} & k_{11} & k_{11} & k_{11} \\ k_{11} & k_{11} & k_{11} & k_{11} & k_{11} & k_{11} \end{bmatrix} \begin{bmatrix} \phi_{14} \\ \phi_{24} \\ \phi_{34} \\ \phi_{44} \\ \phi_{54} \\ \phi_{64} \end{bmatrix}}{[\phi_{14} \quad \phi_{24} \quad \phi_{34} \quad \phi_{44} \quad \phi_{54} \quad \phi_{64}] \begin{bmatrix} m_1 & 0 & 0 & 0 & 0 & 0 \\ 0 & m_2 & 0 & 0 & 0 & 0 \\ 0 & 0 & m_3 & 0 & 0 & 0 \\ 0 & 0 & 0 & m_4 & 0 & 0 \\ 0 & 0 & 0 & 0 & m_5 & 0 \\ 0 & 0 & 0 & 0 & 0 & m_6 \end{bmatrix} \begin{bmatrix} \phi_{14} \\ \phi_{24} \\ \phi_{34} \\ \phi_{44} \\ \phi_{54} \\ \phi_{64} \end{bmatrix}} \quad (17)$$

$$\omega_5 = \frac{[\phi_{15} \quad \phi_{25} \quad \phi_{35} \quad \phi_{45} \quad \phi_{55} \quad \phi_{65}] \begin{bmatrix} k_{11} & k_{11} & k_{11} & k_{11} & k_{11} & k_{11} \\ k_{11} & k_{11} & k_{11} & k_{11} & k_{11} & k_{11} \\ k_{11} & k_{11} & k_{11} & k_{11} & k_{11} & k_{11} \\ k_{11} & k_{11} & k_{11} & k_{11} & k_{11} & k_{11} \\ k_{11} & k_{11} & k_{11} & k_{11} & k_{11} & k_{11} \\ k_{11} & k_{11} & k_{11} & k_{11} & k_{11} & k_{11} \end{bmatrix} \begin{bmatrix} \phi_{15} \\ \phi_{25} \\ \phi_{35} \\ \phi_{45} \\ \phi_{55} \\ \phi_{65} \end{bmatrix}}{[\phi_{15} \quad \phi_{25} \quad \phi_{35} \quad \phi_{45} \quad \phi_{55} \quad \phi_{65}] \begin{bmatrix} m_1 & 0 & 0 & 0 & 0 & 0 \\ 0 & m_2 & 0 & 0 & 0 & 0 \\ 0 & 0 & m_3 & 0 & 0 & 0 \\ 0 & 0 & 0 & m_4 & 0 & 0 \\ 0 & 0 & 0 & 0 & m_5 & 0 \\ 0 & 0 & 0 & 0 & 0 & m_6 \end{bmatrix} \begin{bmatrix} \phi_{15} \\ \phi_{25} \\ \phi_{35} \\ \phi_{45} \\ \phi_{55} \\ \phi_{65} \end{bmatrix}} \quad (18)$$

$$\omega_6 = \frac{[\phi_{16} \quad \phi_{26} \quad \phi_{36} \quad \phi_{46} \quad \phi_{56} \quad \phi_{66}] \begin{bmatrix} k_{11} & k_{11} & k_{11} & k_{11} & k_{11} & k_{11} \\ k_{11} & k_{11} & k_{11} & k_{11} & k_{11} & k_{11} \\ k_{11} & k_{11} & k_{11} & k_{11} & k_{11} & k_{11} \\ k_{11} & k_{11} & k_{11} & k_{11} & k_{11} & k_{11} \\ k_{11} & k_{11} & k_{11} & k_{11} & k_{11} & k_{11} \\ k_{11} & k_{11} & k_{11} & k_{11} & k_{11} & k_{11} \end{bmatrix} \begin{bmatrix} \phi_{16} \\ \phi_{26} \\ \phi_{36} \\ \phi_{46} \\ \phi_{56} \\ \phi_{66} \end{bmatrix}}{[\phi_{16} \quad \phi_{26} \quad \phi_{36} \quad \phi_{46} \quad \phi_{56} \quad \phi_{66}] \begin{bmatrix} m_1 & 0 & 0 & 0 & 0 & 0 \\ 0 & m_2 & 0 & 0 & 0 & 0 \\ 0 & 0 & m_3 & 0 & 0 & 0 \\ 0 & 0 & 0 & m_4 & 0 & 0 \\ 0 & 0 & 0 & 0 & m_5 & 0 \\ 0 & 0 & 0 & 0 & 0 & m_6 \end{bmatrix} \begin{bmatrix} \phi_{16} \\ \phi_{26} \\ \phi_{36} \\ \phi_{46} \\ \phi_{56} \\ \phi_{66} \end{bmatrix}} \quad (19)$$

Generalized response for the system

For general n-degree of freedom system with mass m_i, stiffness matrix k_i, and damping c_i the response in each mode are:

$$x_i(t) = \sum_{i=1}^{6} \sum_{j=1}^{6} A_i \phi_{ij} \sin(\omega_j t + \psi_j)$$

The system responses are:

$$x_1(t) = A_1\phi_{11} \sin(\omega_1 t+\psi_1) + A_2\phi_{12} \sin(\omega_2 t+\psi_2) + A_3\phi_{13} \sin(\omega_3 t+\psi_3) + A_4\phi_{14} \sin(\omega_4 t+\psi_4) + A_5\phi_{15} \sin(\omega_5 t+\psi_5) + A_6\phi_{16} \sin(\omega_6 t+\psi_6) \quad (20)$$

$$x_2(t) = A_1\phi_{21} \sin(\omega_1 t+\psi_1) + A_2\phi_{22} \sin(\omega_2 t+\psi_2) + A_3\phi_{23} \sin(\omega_3 t+\psi_3) + A_4\phi_{24} \sin(\omega_4 t+\psi_4) + A_5\phi_{25} \sin(\omega_5 t+\psi_5) + A_6\phi_{26} \sin(\omega_6 t+\psi_6) \quad (21)$$

$$x_3(t) = A_1\phi_{31}\sin(\omega_1 t+\psi_1) + A_2\phi_{32}\sin(\omega_2 t+\psi_2) + A_3\phi_{33}\sin(\omega_3 t+\psi_3) + A_4\phi_{34}\sin(\omega_4 t+\psi_4) + A_5\phi_{35}\sin(\omega_5 t+\psi_5) + A_6\phi_{36}\sin(\omega_6 t+\psi_6) \quad (22)$$

$$x_4(t) = A_1\phi_{41}\sin(\omega_1 t+\psi_1) + A_2\phi_{42}\sin(\omega_2 t+\psi_2) + A_3\phi_{43}\sin(\omega_3 t+\psi_3) + A_4\phi_{44}\sin(\omega_4 t+\psi_4) + A_5\phi_{45}\sin(\omega_5 t+\psi_5) + A_6\phi_{46}\sin(\omega_6 t+\psi_6) \quad (23)$$

$$x_5(t) = A_1\phi_{51}\sin(\omega_1 t+\psi_1) + A_2\phi_{52}\sin(\omega_2 t+\psi_2) + A_3\phi_{53}\sin(\omega_3 t+\psi_3) + A_4\phi_{54}\sin(\omega_4 t+\psi_4) + A_5\phi_{55}(\omega_5 t+\psi_5) + A_6\phi_{56}\sin(\omega_6 t+\psi_6) \quad (24)$$

$$x_6(t) = A_1\phi_{61}\sin(\omega_1 t+\psi_1) + A_2\phi_{62}\sin(\omega_2 t+\psi_2) + A_3\phi_{63}\sin(\omega_3 t+\psi_3) + A_4\phi_{64}\sin(\omega_4 t+\psi_4) + A_5\phi_{65}\sin(\omega_5 t+\psi_5) + A_6\phi_{66}\sin(\omega_6 t+\psi_6) \quad (25)$$

The system velocities are:

$$\dot{x}_i(t) = \sum_{i=1}^{6}\sum_{j=1}^{6}\omega_j A_i\phi_{ij}\sin(\omega_j t+\psi_j)$$

$$\dot{x}_6(t) = \omega_1 A_1\phi_{61}\cos(\omega_1 t+\psi_1) + \omega_2 A_2\phi_{62}\cos(\omega_2 t+\psi_2) + \omega_3 A_3\phi_{63}\cos(\omega_3 t+\psi_3) + \omega_4 A_4\phi_{64}\cos(\omega_4 t+\psi_4) + \omega_5 A_5\phi_{65}\cos(\omega_5 t+\psi_5) + \omega_6 A_6\phi_{66}\cos(\omega_6 t+\psi_6) \quad (26)$$

$$\dot{x}_5(t) = \omega_1 A_1\phi_{51}\cos(\omega_1 t+\psi_1) + \omega_2 A_2\phi_{52}\cos(\omega_2 t+\psi_2) + \omega_3 A_3\phi_{53}\cos(\omega_3 t+\psi_3) + \omega_4 A_4\phi_{54}\cos(\omega_4 t+\psi_4) + \omega_5 A_5\phi_{55}\cos(\omega_5 t+\psi_5) + \omega_5 A_6\phi_{55}\cos(\omega_6 t+\psi_6) \quad (27)$$

$$\dot{x}_4(t) = \omega_1 A_1\phi_{41}\cos(\omega_1 t+\psi_1) + \omega_2 A_2\phi_{42}\cos(\omega_2 t+\psi_2) + \omega_3 A_3\phi_{43}\cos(\omega_3 t+\psi_3) + \omega_4 A_4\phi_{44}\cos(\omega_4 t+\psi_4) + \omega_5 A_5\phi_{45}\cos(\omega_5 t+\psi_5) + \omega_6 A_6\phi_{46}\cos(\omega_6 t+\psi_6) \quad (28)$$

$$\dot{x}_3(t) = \omega_1 A_1\phi_{31}\cos(\omega_1 t+\psi_1) + \omega_2 A_2\phi_{32}\cos(\omega_2 t+\psi_2) + \omega_3 A_3\phi_{33}\cos(\omega_3 t+\psi_3) + \omega_4 A_4\phi_{34}\cos(\omega_4 t+\psi_4) + \omega_5 A_5\phi_{35}\cos(\omega_5 t+\psi_5) + \omega_6 A_6\phi_{36}\cos(\omega_6 t+\psi_6) \quad (29)$$

$$\dot{x}_2(t) = \omega_1 A_1\phi_{21}\cos(\omega_1 t+\psi_1) + \omega_2 A_2\phi_{22}\cos(\omega_2 t+\psi_2) + \omega_3 A_3\phi_{23}\cos(\omega_3 t+\psi_3) + \omega_4 A_4\phi_{24}\cos(\omega_4 t+\psi_4) + \omega_5 A_5\phi_{25}\cos(\omega_5 t+\psi_5) + \omega_6 A_6\phi_{26}\cos(\omega_6 t+\psi_6) \quad (30)$$

$$\dot{x}_1(t) = \omega_1 A_1\phi_{11}\cos(\omega_1 t+\psi_1) + \omega_2 A_2\phi_{12}\cos(\omega_2 t+\psi_2) + \omega_3 A_3\phi_{13}\cos(\omega_3 t+\psi_3) + \omega_4 A_4\phi_{14}\cos(\omega_4 t+\psi_4) + \omega_5 A_5\phi_{15}\cos(\omega_5 t+\psi_5) + \omega_6 A_6\phi_{16}\cos(\omega_6 t+\psi_6) \quad (31)$$

3. Results and discussion

One could see that as predicted by physical inspections, constraining the boundaries results in increments of the amplitudes .It may seem that natural condition of the hand-arm are most closely described as single degree of freedom system. From a modal analysis point of

view, modeling of hand-arm and hand arm tool vibration are two challenging problems and they might have no unique answer especially in terms of classic boundary condition or what seems to be logically valid. For the identification of correct analysis is to do theoretical investigation and compare the results with model frequencies and shapes and to identify which set boundary conditions best describes the problem. Thus ,values of natural frequencies and the shape of natural modes are necessary for the jackhammer Model Updating of the hand .These values are important in three other senses .First ,these natural frequencies along with natural modes ,which are presented here, could be used for the development of lumped –parameter models of the hand –arm vibration .The procedure is one of the model analysis inverse problems domains .These models are typically easier to deal with and at the same time they could be integrated with other existing lumped-parameter models of the system. It is especially more important known that most of the vibrational models of the system are lumped-parameter models. Second, these values could be used for the determination of the type of vibrational loading that the hand-arm is exposed to and to determine if these vibrational risks could result in cumulative of the amplitudes situation of the system .Third, these values are of importance and change of values could be regarded as a case of probable hand-arm injuries. Forther the papers are presented acomplete analysis of the system in single and combined modes of boundary condition are necessary to be in hand-arm vibration injuries especially in the cases of large amplitude deficiency. Effects of geometry on natural frequencies of the humerus are of special interest mainly because of the fact that one could expect the range of natural frequencies of a humerus. Knowing how the vibrational properties are affected by geometry calls for a huge number of computational investigations among which the most important ones are presented here and some are mitted due to constraints .The natural frequencies are affected by the hand of individual human samples being considered. theoretical concerned with the hand arm vibration indicate that the design of jack hammer can be improved by predicting the hand-arm jack hammer behavior using the simulation .the simulation figures are being performed. First, simulation assumes that the humerus is subject to change in different amplitudes without dynamic vibration absorber. Second simulation, assumed that the humerus is subject to change in different amplitudes with dynamic vibration absorber. Qualitatively, in both simulations natural frequencies are being decreased by using dynamic vibration absorber of the geometrical dimensions. Values of the first simulation are presented here;could be consulted for computed values of the second simulation.The original geometry dimension are being considered.

4. System vibration control

By dividing the jack hammer system into discrete masses as shown in Fig.(3); m_1=10kg ,$m_{2,3}$=5kg ,m_4=15kg,m_5=5kg,m_6 which represent to the mass of hand arm of the worker=(4.5Kg).determining the six responses of the jack hammer system by one can add the dynamic vibration absorber between the masses(1,2,and3). The dynamic vibration absorber is as a simply single degree of freedom system ,usually used in the form of a simply spring – mass system .When it added to another single degree of freedom system as an auxiliary system ,it will transform the hole system in two degree of freedom with two natural frequencies of vibration .One of the natural frequencies is set above the excitation frequency while the other is set below it ,so that the main mass of entire system will have very small amplitude of vibration instead of very large amplitude under the given excitation. Then we can see how the response by adding the dynamic vibration absorber which will make the amplitude of response that reaches to the Hand-Arm very small .This reduces the risks, and protect the workers.

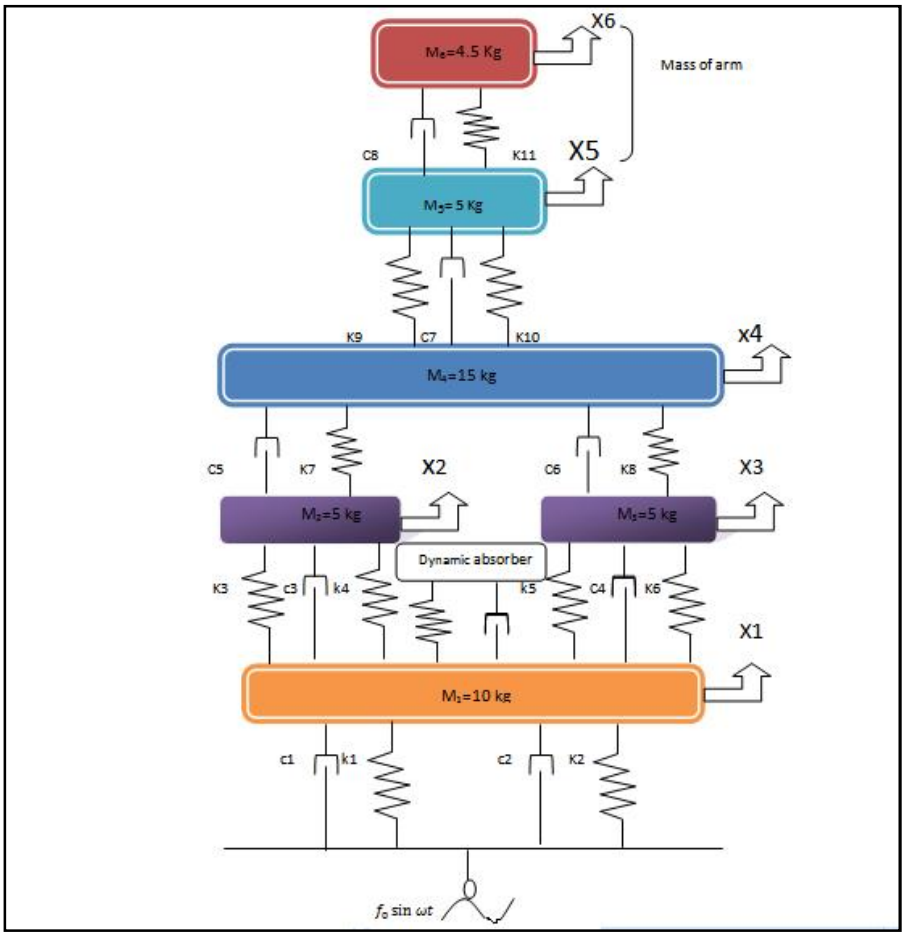

Figure (3). Systematic representation with dynamic absorber.

5. The deformations in jack hammer geometry

The vibration tool" jack hammer" can be drawn in Ansys v(5.4) program by putting the key point in the worksheet and connect it by lines then putting the force in the lower point (that means forced vibration)which its value will be between (10-20)N. After that it becomes easy to carry out the program and we will see how the deformation will be clear in the truss of the jack hammer due to the higher amplitude of response and how this deformation would reach the hand in high amplitude.

The uses of Ansys in this projects are to understand how the high amplitude of response will reach to the arm of the worker and causes the damage of the hand.

Figures (4-13) show the deformation which happened to the geometry due to the excitation in different masses ,and the red color shows the highest stress that affect the device ,and the other colors will be the decreasing of stresses gradually.

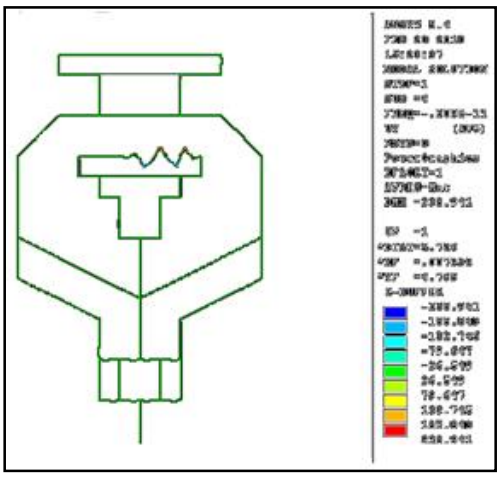

Figure(4). First mode shape .

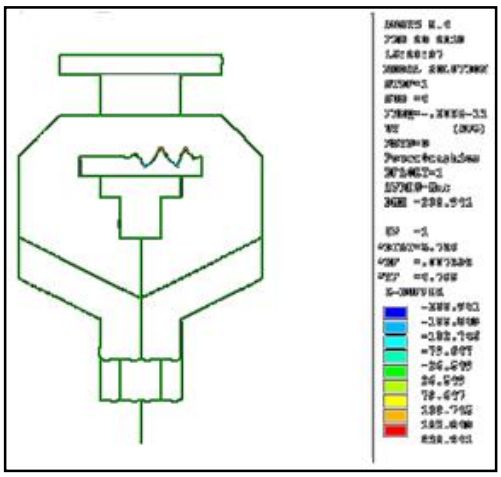

Figure(5). First mode shape.

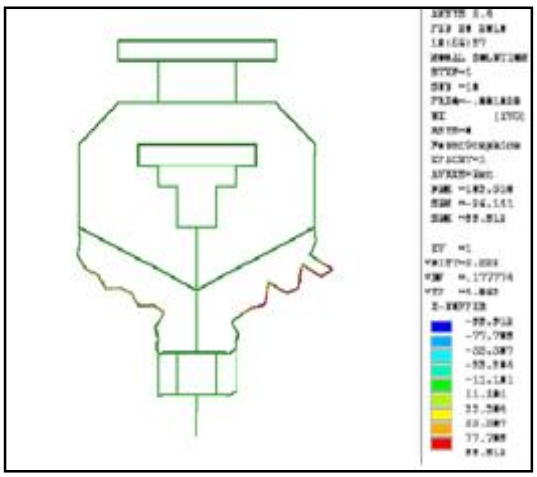

Figure(6).Second mode shape.

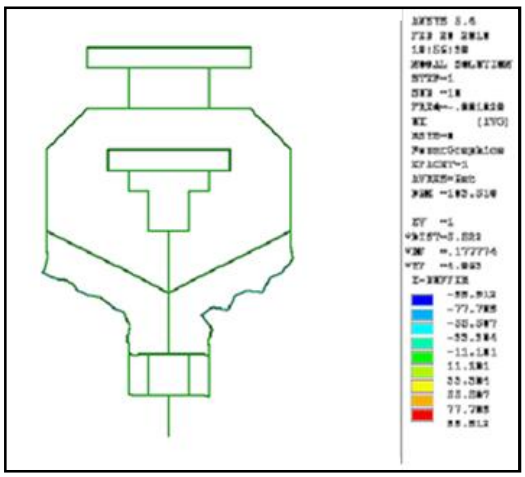

Figure(7). Third mode shape.

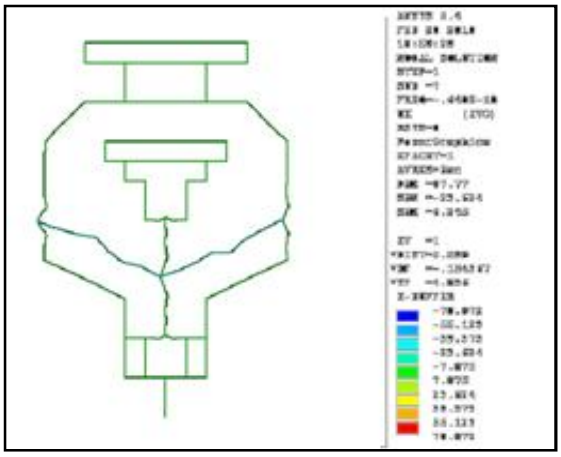

Figure(8).Forth mode shape .

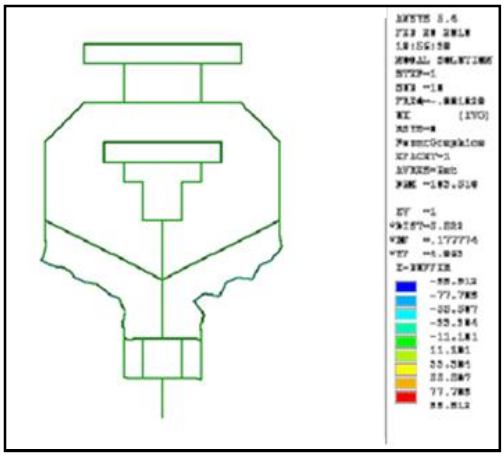

Figure (9).Fifth mode shape .

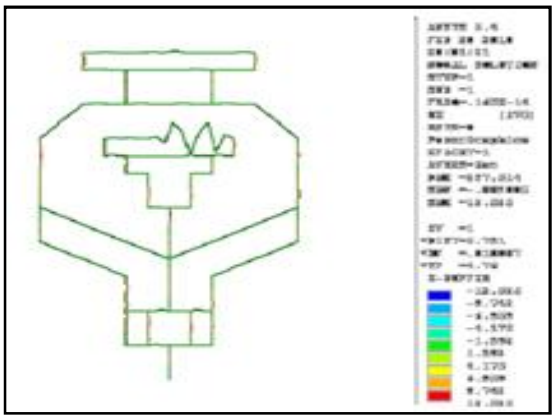

Figure (10).Sixth mode shape .

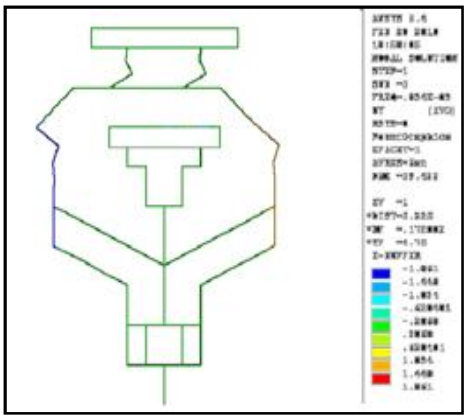

Figure (11).Seventh mode shape.

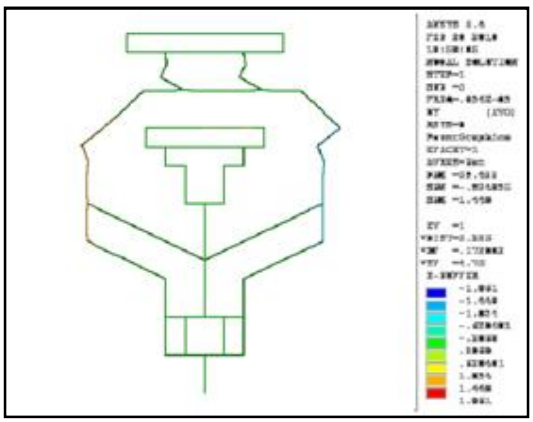

Figure (12).Eighth mode shape .

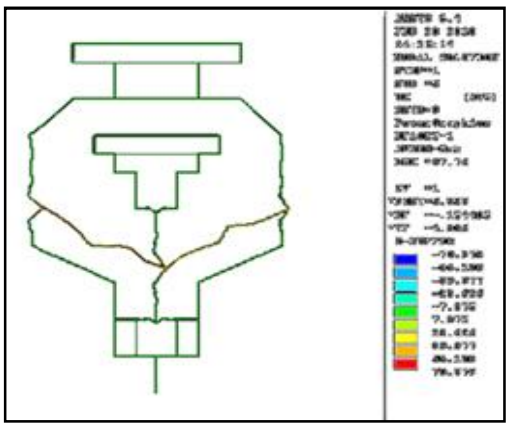

Figure (13). Ninth mode shape.

Figure (14) shows the responses of the system . The six equations of response which have 12 unknown like (A,B,C,D,E,F)and the six phase angle now can find the velocity of every response ,and by finding it there are 12 varabile and 12 equations . By using Fortran power station one can find the data that used a program to draw the curves for all responses Figure (14).

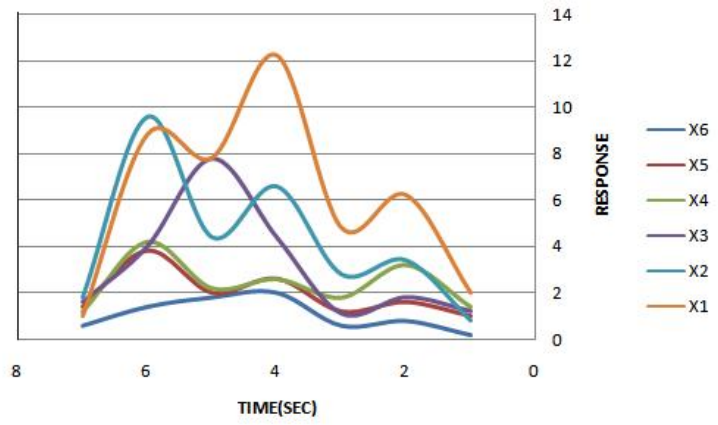

Figure (14). System responses without dynamic vibration absorber.

By adding the dynamic vibration absorber between the masses (1, 2, 3) this will vanish the response of these masses as shown in Figure(15). This response of (4, 5, 6) will also reduced to be safer for the arm.

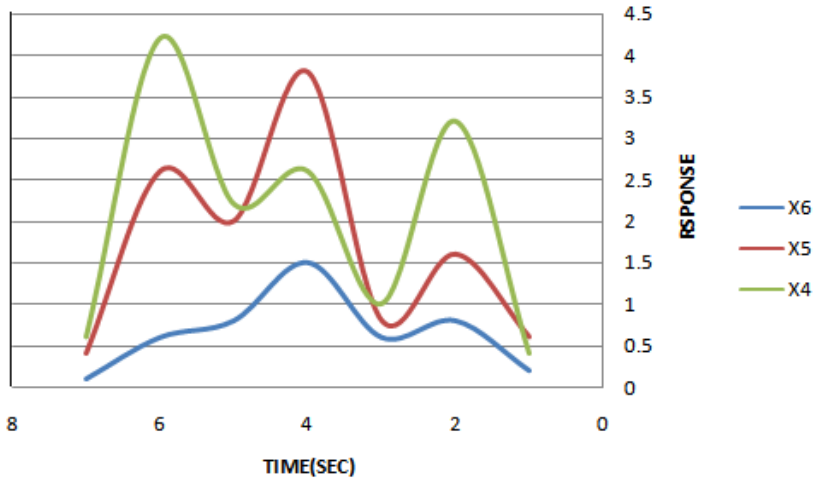

Figure(15) .System responses with dynamic vibration absorber.

The difference between the two Figures (14) and (15) shows that the dynamic vibration absorber will reduce the very large amplitude and the response that reaches to the arm will be less in the presence of dynamic vibration absorber ,and this will make the vibration reached to the arm less so that the risks will be reduced .

7. Conclusions

The jack hammer was of the hand-operated type in common use. Accelerations caused by it were taken as a point of reference since most persons have heard, if not seen, this type of machine in operation. These particular ground accelerations were the most periodic of any obtained in this investigation. The distance from the source was measured from the point of application of the bit.

Most papers on the investigation of the dynamics of jackhammer system it is usually assumed that during the operating process the parameters of these systems remain constant. However, the parameters, especially the stiffness and damping coefficients under impact. Therefore a study of jackhammer systems under conditions close to the actual ones leads to the problem of investigating dynamic systems in the presence of randomly varying parameters.

The simulation proves the presented mathematical model in terms of more accurate model parameters and analyzes the dynamic characteristics of the jackhammer structure when it is subjected to vibrational loading, studies the propagation taking into account the response vector (elements representing the response in each DOF), the excitation vector (elements representing the force in each DOF), degree of freedom (points & directions), frequency response matrix, and frequency response function.

Based on the optimal parameters, we design dynamic vibration absorber (spring – dashpot system) whose stiffness and damping are independently adjustable, to reduce the propagation of amplitudes to the desired value by decreasing the high amplitudes to very small amplitudes to protect the operator from the hand vibration risks.Hand Arm Vibration will often affect the people who regularly use high vibration equipment such as a jack hammer tool .The vibration of the tool or any material being vibrated is transmitted to the hands. Regular and frequent exposure to hand-arm vibration can lead to permanent health effects. This is most likely when contact with a vibrating tool or work process is regular part

of a person's job. Occasional exposure is unlikely to cause ill health , the exposure limit value is the maximum amount of vibration an employee may be exposed to on any single day. For hand-arm vibration the exposure limit value is a dailexposure of 5 m/s^2 It represents a high risk above which employees should not be exposed. The degree of risk will depend on many factors such as the amount of vibration, how long the tools are used for, the working posture and how cold it is will all make a difference. Using ansys programs version (5.4) will help us to predict the eigenvectors (mode shapes) and the natural frequency of jack hammer..the main aim of this research was to reduce the high amount of vibration and this can be done by using the dynamic vibration absorber which is a simply-spring mass system (single degree of freedom system) added to the original mass system to transform the system to degree of freedom system and the entire system will have two eigenvalue one above the excitation and the other under the excitation .And this will protect the employees from the risk and it is clear how amplitude of response is different after adding dynamic vibration absorber.

8. References

[1] Zadpoor A., Finite Element Method Analysis of Human Hand Arm Vibrations, Int. J. Sci. Res., Vol. 16, pp. 391-395, 2006.

[2] Richard W. Flygare, an Investigation of Ground Accelerations Produced by Machines, California Institute of Technology Pasadena, California, 1955.

[3] Hal A. and Michael G., Construction Vibrations and Their Impact on Vibration-Sensitive Facilities, San Mateo, California, 2000.

[4] L. Zuo Optimal Control with Structure Constraints and its Applicationto the Design of Passive Mechanical Systems. Master's thesis Massachusetts Institute of Technology. 2002.

[5] K. Seto, M. Ookuma, S. Yamashita and A. Nagamatsu JSME International Journal, Series III 30, 1638–1644. Method of estimating Equivalent mass of multi-degree-of-freedom system, 1987.

[6] Zuo L. and Nayfeh S., Structural Dynamics and Materials Conference, 2002.

[7] Amick, H., and Ungar, E., Evaluation of Ground and Structural Vibrations from Pile Driving," BBN Report No. 6427, January 1987.

[8] Alem N., Application of the new ISO 2631-5 to health hazard assessment of repeated shocks in U.S. army vehicles. Ind Health 43:403–412, 2005.

9. Nomenclature

Symbols	Description	Unit
A ,B ,C, D ,E ,F	Variables	---
C	Damping matrix	[N.s/m]
F_0	Force applied to the system	[N]
K	Stiffness matrix	[N/m]
$[k^c]$	Cofactor of the stiffness matrix.	[N/m]
$[k^c]^T$	Cofactor transpose of the stiffness matrix.	[m / N]
ϕ_{ij}	Mode shape (eigenvectors)	---
$[\phi_{ij}]^T$	Transpose of the mode shape matrix	---
$\|D\|$	Determinate of stiffness matrix.	---
ω	Natural frequency	[rad/sec]
ψ	Phase angle	---
M	Mass	[Kg]
x(t)	Response of the system	[mm]
$\dot{x}(t)$	Velocity	[mm/s]
$\ddot{x}(t)$	Acceleration	[mm/s^2]

Estimation of Flow in Horizontal Elliptic Channels with Free Overfall at the End of the Channel

Iqbal Khalaf Eraebee

Civil Engineering Department

College of Engineering

Thi-Qar University

Abstract

The aim of this work is to calculate the flow discharge in horizontal elliptic channels with free overfall at the end of the channel. Two methods are used, the first one is Boussinesq approximation to calculate the End- Depth – Ratio (EDR) .The second one is a theoretical procedure applied to compute the flow over a sharp – crested weir.The available experimental data are used to verify the proposed End – Depth – Discharge (EDD) relationship. The calculated discharges, using the proposed EDD relationship, show excellent agreement with the experimental values in subcritical flows. However, the agreement is not so good in supercritical.

Keywords : Open channel flow ; Free overfall ; End – depth.

المستخلص

الهدف من هذا البحث هو حساب كمية التصريف في القنوات ذات الشكل البيضوي من خلال الطفح الحاصل في نهاية القناة .استخدمت لهذا الغرض طريقتان, الطريقة الاولى تمت باستخدام تقريب (Boussineq) لحساب نسبة العمق النهائي الى العمق الحرج. اما الطريقة الاخرى فهي حساب كمية التصريف فوق السد المنحي الحاد في نهاية القناة مع فرض ضغط الماء مساوي صفر عند تلك النهاية . من خلال الاستعانة بالنتائج العملية لدراسات سابقة ومقارنتها مع النتائج النظرية لقيم التصريف وجد ان قيمة التصريف المحسوبة من خلال نسبة العمق النهائي الى التصريف متوافقة تماما مع القيم العملية في حالة الجريان شبة الحرج , بينما ظهر عدم التوافق للنتائج في الحالتين سابقتي الذكر في حالة الجريان في الوضح الحرج جدا".

1. Introduction

A free overfall occurs when the flow detaches from the solid boundary to form a free nappe owing to an abrupt decrease in channel bed elevation (that is a drop structure)[1]. It offers a method of discharge measurement in open channels from a single measurement of the depth at the brink known as end depth . The value of the end depth depends on the shape of the approach channel. If the slope of the channel is negative, zero or mild, the flow at upstream of the fall will be critical. However, if the upstream channel is steep, the flow will be supercritical and normal depth occurs upstream of the brink[2].

The measurement of flow discharge in open channels is useful especially in channels having covers (sewer, duct, tunnel etc.) . Rouse [3], being the first to investigate the end-depth experimentally, proposed a relationship termed End-Depth Ratio (EDR = end-depth/critical-depth), which was found to be 0.715 in mildly sloping rectangular channels.Diskin [4] applied a momentum equation between apparent and end sections and obtained an expression for end-depth ratio (EDR), i.e., ratio of end depth to critical depth, *YC*. Rajaratnam and Muralidhar [5] introduced a pressure coefficient in the momentum equation and calculated EDR = 0.667, 0.731 and 0.775 for subcritical flows in rectangular, parabolic and triangular channels, respectively. Dey [6] extended the use of the momentum equation to calculate EDR for others shapes of channels. The generalized energy method gives EDR = 0.694, 0.734 and 0.762 for subcritical flows in rectangular, parabolic and triangular channels, respectively. Anastasiadou-Partheniou and Hatzigiannakis [7], Ferro [8] and Ahmad [2] simulated the free overfall with a sharp crested weir of zero height. Marchi [9] solved the two dimensional free overfall using cnoidal wave theory.

Dey [10] presented a theoretical and experimental study on free overfall in an inverted semicircular channel. He applied the momentum equation between the apparent section and the end section and found that EDR = 0.705 for subcritical flows up to the ratio of critical depth, and diameter 0.42. However, in the supercritical flow, the EDR decreases with increase in relative bed slope (ratio of critical bed slope, S_C, to bed slope, S). He also found that computed discharges obtained through application of a momentum equation in supercritical flows are not comparable with the experimental ones. The reason for the disagreement is due to neglecting the stream-wise component of the gravity force in the momentum equation.

In this paper, two separate methods are presented to analyze the free overfall in elliptic channels, as shown in Figure (1)(a, b and c). First, an analytical model for a free overfall from smooth elliptic channels is presented, applying a momentum approach based on the Boussinesq assumption. Secondly, an alternate approach for a free overfall from elliptic channels is also presented. The model yields the end-depth ratio and end depth– discharge relationship, which are verified using the experimental data of previous studies.

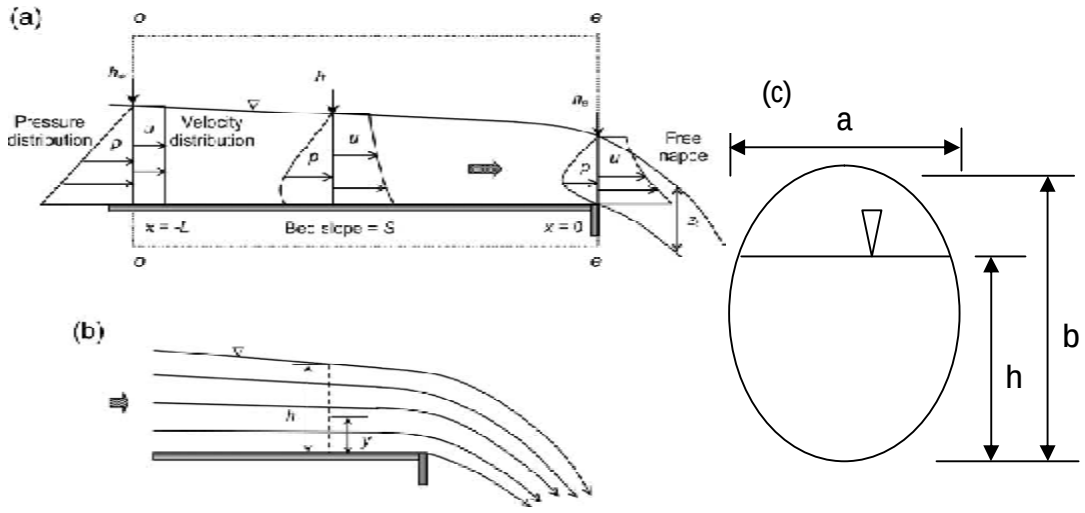

Figure (1). (a) Schematic view of a typical free overfall.

(b) Streamline pattern of a free overfall.

(c) Cross –section of an elliptic channel.

2. Problem Formulation

2.1. Boussinesq approximation

The free surface curvature of a free overfall being relatively small varies from a finite value at the free surface to zero at the channel bed as shown in Figure (1). According to the Boussinesq approximation [11], a linear variation of the streamline curvature with depth y is assumed. Hence, the radius of curvature r of a streamline at y is expressed by:

$$1/r = (y/h)(1/r_s) \quad (1)$$

Where

h =flow depth, and r_s=radius of curvature of the free surface. For the small free surface curvature, it can be approximated by:

$$1/r_s = d^2h/dx^2 \quad (2)$$

Where:

x = streamwise distance. The normal acceleration ay based on the aforementioned assumption is given by:

$$a\ y = k\ y \quad (3)$$

Where:

$$K = \frac{V^2}{h}\frac{d^2\ h}{dx^2} \quad (4)$$

Where V = mean flow velocity. Integrating the Euler equation (see Subramanya [12]), the effective hydrostatic pressure head h_{ep} is expressed by

$$h_{ep} = h + \frac{kh^2}{3g} \quad (5)$$

Where g =gravitational constant. Eq. (5) obtained by Boussinesq [11] is applicable in solving problems with small curvature at the free surface, namely free overfall**.**

The flow velocity at the end section is calculated by applying the Bernoulli equation on a streamline between the upstream section at x =- L and the end section at x = 0. The discharge Q is computed using the following equation:

$$Q = Cd\sqrt{2g}\int_0^{h_0} t\sqrt{(H-y)dy} \quad (6)$$

Where Cd = coefficient of discharge (= $Cv\ Cc$), Cv= coefficient of velocity, Cc = coefficient of contraction, t =channel width at an elevation y, and H = total head. The total head H at the upstream section (x = -L) is given by

$$H = h_0 + \frac{V_0^2}{2g} \quad (7)$$

2.2. End-depth–discharge relationship

The free overfall is a special case of a sharp-crested weir, at the end of the channel and of zero height. The theoretical procedure applied to compute the discharge over a weir can also be applied to a free overfall to get the EDD relationship [8]. The flow velocity at any depth at free overfall is calculated by applying the energy equation between any two points located at sections o–o and e–e (see Figure (1).(a)). It is assumed that all the streamlines at the brink are parallel to each other, i.e., the emerging jet is undeflected. To account for the curvature of streamlines, i.e., the deflection of the jet due to gravity, a coefficient of contraction is considered. Zero pressure at the brink is assumed. The discharge through an elemental strip of thickness d*y* at a height *y* above the bed is given by:

$$dQ = 2g\{H - y\}^{1/2} T\, dy \tag{8}$$

Where g = acceleration due to gravity; $\boldsymbol{H = Y_1 + \frac{V_1^2}{2g}}$, T = top width, given by the following relationship:

$$T = (D_2 - 4y_2)^{1/2} \tag{9}$$

Where D = diameter of the channel. Substituting Eq. (9) into Eq. (8), the total discharge is given by

$$Q = C_C\sqrt{2g}\int_0^{Y1} \frac{(H - y_1)}{2D}\ (1 - \frac{y_2}{D_2})^{1/2} dy \tag{10}$$

Where C_C= coefficient of contraction. Rearranging Eq. (10), one can get

$$F_1 = \frac{V_1}{\sqrt{2gA_1/T_1}} \tag{11}$$

$$A_1 = \frac{D^2}{8}[2sin^{-1}(2X_1) + 4X_1\sqrt{(1 - 4X_1^2)}\ ]$$

$$= \frac{D^2}{8}\emptyset_1(X_1) \tag{12}$$

$$T_1 = D\sqrt{(1 - 4X_1^2)} = D\emptyset_2(X_1) \tag{13}$$

Where:

$$X_1 = \frac{Y_1}{D} \tag{14}$$

$$H = Y_1\left(1 + \frac{F_1^2\ A_1}{2Y_1T_1}\right) \tag{15}$$

Substitution of Eqs. (12) and (13) into Eq. (15) yields

$$\frac{H}{D} = X_1\left[1 + \frac{F_1^2}{16X_1}\frac{\emptyset_1(X_1)}{\emptyset_2\,(X)_2}\right] \tag{16}$$

Ahmad [13] theoretically solved the EDR in circular channels, as was done by Dey [6], who solved equations numerically for the EDR, where Ahmad [13] used a series to solve the equations. He derived the following EDD relationship for subcritical flow :

$$Q^{\wedge} = \frac{Q}{g^{1/2}D^{5/2}} = \frac{1}{16\sqrt{2}}\frac{\emptyset_1\,(X_C)^{3/2}}{\emptyset_2(X_C)^{1/2}} \tag{17}$$

2.3. Theoretical approach

The set of characteristic parameters appropriate for free overfall phenomenon at the end of a channel can be given in functional form as follows:

$$Q = f_1\,(h_e, l, m, g, \mathrm{m}) \tag{18}$$

where l = characteristic length parameter of a channel, and m = dynamic viscosity of fluid. Using the Buckingham p-theorem and selecting the parameters l, g and m as repeating variables, the non dimensional parametric equation in functional form can be given by:

$$Q^{\wedge} = f_2(h_e\hat{}, m) \tag{19}$$

Where $Q^{\wedge} = Q/\,(g^{0.5}\,l^{2.5})$, and $h\hat{}\,\mathrm{e} = he\,/\,l$. As it is not appropriate to use m as a free parameter, a refinement of the above equation can be done as:

$$Q\hat{} = f_3\,(h_e\hat{}\,) \tag{20}$$

Dey [13] theoretically analyzed free overfall in horizontal elliptic channels, using the momentum equation based on the Boussinesq approximation. So, we can use equation (17) to estimate the EDD for elliptic channel with free overfall by substituting the major axis (a) , with the diameter of channel (d) as shown below :

$$Q^{\wedge} = \frac{Q}{g^{0.5}\,.a^{2.5}} \tag{21}$$

respectively, for different values of λ(=a/b), where a is the major axis, and b is the minor axis, as shown in Figure (1.c).

3. Calculation of Flow Discharge in Horizontal Elliptic Channel With Free Over fall

First, the free overfall from elliptic channels has been calculated by applying the momentum equation based on the Boussinesq approximation. The method eliminates the need of an experimentally determined pressure coefficient. In subcritical flows, the EDR has been related to the critical-depth. On the other hand, in supercritical flows, the end-depth has been expressed as a function of the streamwise slope of the channel using the Manning equation. The mathematical solutions allow estimation of discharge from the known end-depth in subcritical and supercritical flows. Streamline curvature at the free surface has been used to compute the upstream flow profiles of a free overfall. The comparisons of the experimental data with this model have been satisfactory for subcritical flows and acceptable for supercritical flows.

The discharge of an elliptic channel with 4 m long and λ (=a/b) ranging from 0.3 to 4 was calculated by using the following equation which was derived by Rohwer [15] :

$$Q = 8.58\ a^{0.62}\ .\ b^{1.82} \qquad (22)$$

While The EDD ($Q^{\wedge}$) is calculated from equation (21) for an elliptic channel with EDR ($h_e^{\sim}$) $= h_e\ /\ h_c$, which can be calculated for two cases:

3.1 Subcritical Flow

The EDR predicated from momentum equation is:

$$h_e^{\sim} = \left(\frac{2F_1^2}{1 + 2F_1^2}\right)^{\frac{2}{3}} \qquad (23)$$

Where $F_1 = \frac{Q}{(g\ d\ h_0^4)^{0.5}}$ (24)

3.2 Supercritical Flow

In supercritical flow, the EDR $h_e^{\sim}$ is expressed as a function of relative slope S and $h_c^{\wedge}$ using Manning equation . Figure (2) show the relationship between EDR ($h_e^{\sim}$) and $h_c^{\wedge} = (h_c/\ a\ )$, Figure (3) present the variations of $h^{\wedge}_e$ (=h_e/a) with $Q^{\wedge}$.

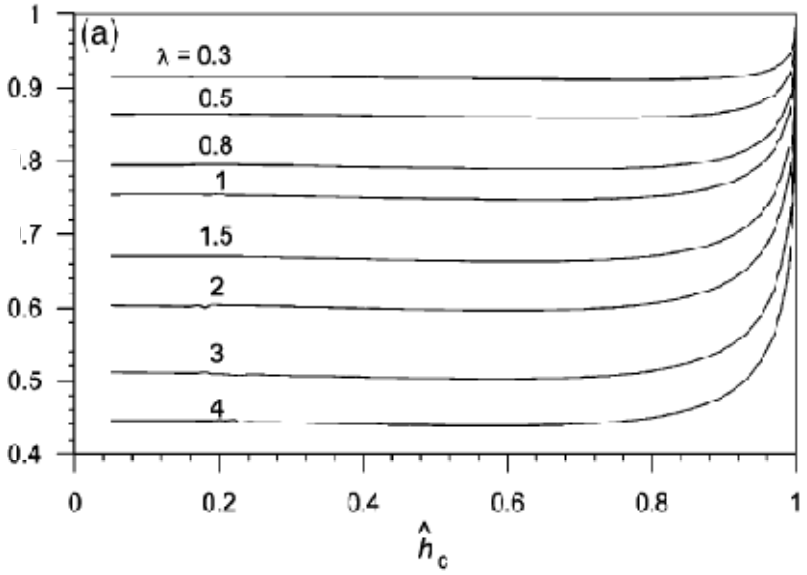

Figure (2). Dependency of EDR $h_e^{\sim}$ on $h_c^{\wedge}$ for different λ.

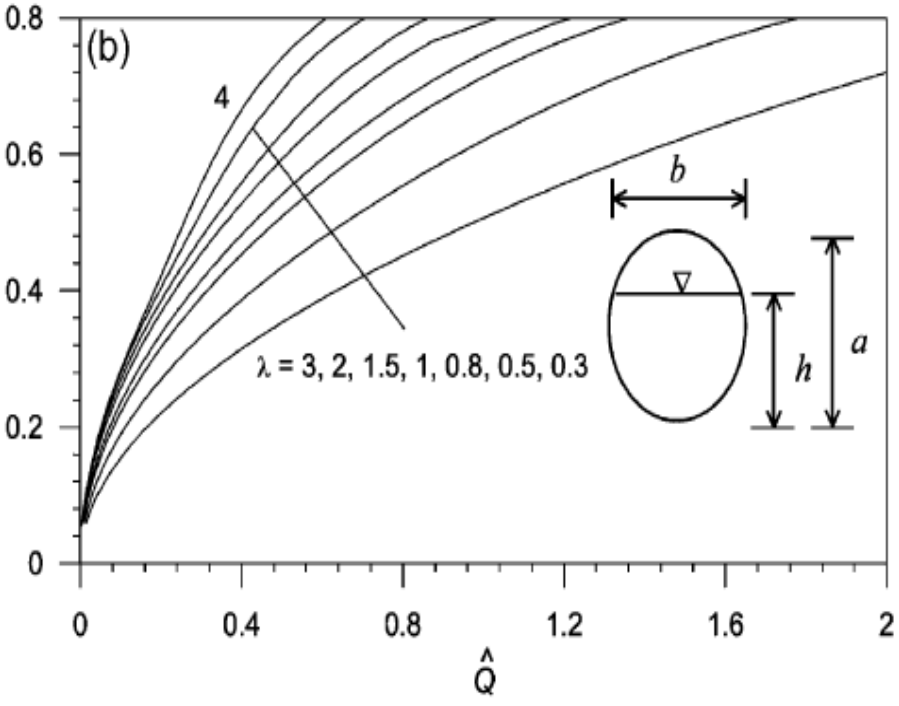

Figure (3). Variation of $h_e^{\wedge}$ with $Q^{\wedge}$ for different λ in elliptic free over fall.

4. Results and discussion

From the computations of flow discharge in the end of the channel and comparative the variations of EDR $h\tilde{}_e$ with $h\hat{}_c$ as shown in Figure (2) , we can notice that the value of EDR $h\tilde{}_e$ is approximately 0.725 for a wide range of $h_c^{\wedge}$. Figure (3) show that The EDD $Q^{\wedge}$ increases with increase in $h_e^{\wedge}$. Table (1) shows that the computed values of $Q\hat{}$ have a slight variation from the experimental observations of Dey [13] due to the assumption of pseudo-uniform flow and the use of the Manning equation in small channels. The calculated discharges, using the proposed EDD relationship, show excellent agreement with the experimental values in subcritical flows. However, the agreement is not so good in supercritical.

Table (1). Comparisons of experimental data of Dey [1] with computational data obtained from present analysis.

End – Depth - Ratio			Experimental	Computed
$h_c^{\wedge}$	$h_e^{\wedge}$	$h_{\tilde{e}}$	$Q^{\wedge}$	$Q^{\wedge}$
0.206	0.149	0.721	0.0865	0.0917
0.2462	0.175	0.711	0.1138	0.113
0.45	0.325	0.721	0.2984	0.340
0.478	0.345	0.723	0.3296	0.367
0.529	0.38	0.719	0.3911	0.412
0.497	0.357	0.718	0.3477	0.380
0.323	0.232	0.719	0.1753	0.227
0.361	0.261	0.726	0.2092	0.262
0.169	0.124	0.736	0.0673	0.075
0.193	0.144	0.749	0.0825	0.090

5. References

[1] Dey, S., 2002," Free overfall in Circular Channels with Flat Base: A Method of Open Channel Flow Measurement", Flow Measurement and Instrumentation Vol. 13, pp. 209–221.

[2] Ahmad, Z., 2005, " Flow Measurement Using Free Overfall In Inverted Semi-Circular Channel", Flow Measurement and Instrumentation Vol. 16 , pp. 21–26.

[3] Rouse, H., 1936, " Discharge Characteristics Of The Free Overfall", CivilEngineering ASCE Vol.6 , pp. 257–260.

[4]Diskin, M., H., 1961, "The End Depth At A Drop In Trapezoidal Channels", Journal of Hydraulic Division ASCE Vol. 87, pp. 11–32.

[5] Rajaratnam, N., Muralidhar, D., 1968, " Characteristics Of Rectangular Free Overfall", Journal of Hydraulic Research Vol.6, pp. 233–258.

[6] Dey, S., 1998, " End Depth In Circular Channels", Journal of Hydraulic Engineering ASCE Vol. 124, pp. 856–863.

[7] Anastasiadou-Partheniou, L., Hatzigiannakis, E., 1995, " General End Depth- Discharge Relationship At Free Overfall In Trapezoidal Channel", Journal of Irrigation and Drainage Engineering ASCE Vol. 121, pp. 143–151.

[8] Ferro, V., 1992, " Flow Measurement With Rectangular Free Overfall", Journal of Irrigation and Drainage Engineering ASCE Vol. 118, pp. 956-970.

[9] Marchi, E., 1993, " On The Free Overfall", Journal of Hydraulic Research Vol. 31 , pp.777–790.

[10] Dey, S., 2001, " Flow Measurement By The End-Depth Method In Inverted Semi-Circular Channels", Flow Measurement and Instrumentation Vol. 12, pp.253–258.

[11] Jaeger, C., 1957, " Engineering Fluid Mechanics", St. Martin's Press, Inc.

[12] Subramanya, K., 1997, " Flow in Open Channels", Tata McGraw Hill Publishing Company, Inc., New Delhi, India.

[13] Dey, S., 2001, " Flow Metering By End-Depth Method In Elliptic Channels", Dam Engineering Vol.12 , pp. 5–19.

[14] Ahmad, Z., 2002, "End-Depth-Discharge Relationship For Circular Free Overfall", Journal of Institution of Engineers (India) Vol.83 , pp. 21–24.

[15] Rohwer, C., 1943, " Discharge Of Pipes Flowing Partly Full", Civil Engineering ASCE Vol.13,pp. 488–490.

6. Nomenclature

a	Major axis of elliptic channel (m)
A	Flow area (m^2)
b	Minor axis of elliptic channel (m)
C_c	Coefficient of contraction
C_d	Coefficient of discharge
C_v	Coefficient of velocity
d	Channel diameter (m)
E	Specific energy (m)
F	Froude number of approaching flow
g	Gravitational constant ($m.s^{-2}$)
h	Flow depth (m)
$h\hat{}$	h/a
$h\tilde{}$	h/h_c
h_{ep}	Effective hydrostatic pressure head (m)
H	Total head (m)
l	Characteristic length of channel (m)
L	Length of control section (m)
Q	Discharge ($m^3.s^{-1}$)
$Q\tilde{}$	Free over low of elliptic $Q/(g^{0.5} . a^{2.5})$
S	Streamwise slope
T	Top width of flow (m)
V	Mean velocity of flow ($m.s^{-1}$)
λ	= a/ b

Subscripts

c	Critical flow
e	End section
o	Upstream section

Experimental and Theoretical Studies on Mechanical Properties of Composite Materials

Zainab Talib Abidzaid Al-Sharify

Environmental Engineering

College of Engineering

Al-Mustansiryia University

Iraq – Baghdad / Bab-AL- Muthem / P.O. Box 14150

Zainab_talib2009@yahoo.com

Abstract

Resistible composites have been suggested to be used instead of carbon steel pipes to overcome a number of common problems during commercial applications, especially the problem of fixing dead-beat carbon steel pipes within these systems. The new composites used are resistible materials of unsaturated polyester sponsored with glass fiber and aluminum honeycomb. Mechanical properties of resistible composites have been studied using ASTM in order to find the best conditions to create a system of pipes. It have been seen clearly that the best concentration of aluminum powder is 3٥ % of the composite mixture, which represent the most suitable mechanical properties. Also, it was found that aluminum honeycomb samples were a very good mechanical properties suitable for certain applications**.**

Key Words: Composite Material, Carbon Steel Pipes, Polyester, Mechanical Properties, ASTM.

الدراسة العملية والنظرية للخصائص الميكانيكية للمواد المركبة

المستخلص

تم اقتراح مواد مركبة بديلة لتصنيع الأنابيب الناقلة للتغلب على المشاكل الحاصلة في التطبيقات التجارية و خاصة مشاكل الاستهلاك في أنابيب الكاربون ستيل المستخدمة. المواد المركبة المستخدمة كبدائل هي مواد مقاومة تتكون من بولي استر غير المشبع مقوى بألياف الزجاج و خلايا الالمنيوم. تم دراسة الخواص الميكانيكية للمواد المركبة باستخدام الفحوصات القياسية ASTM لإيجاد افضل الظروف لإنشاء منظومة الأنابيب. وجد أن أكثر مواصفات ميكانيكية ملائمة تكون في تركيز% ٣٥ من مسحوق الالمنيوم في الخليط و كذلك وجد ان النماذج التي تحتوي على خلايا الالمنيوم تكون ذات مواصفات ميكانيكية جيدة و مفيدة للاستخدامات الخاصة.

1. Introduction

Composite materials were known to mankind in the Paleolithic age (also known as Old Stone Age). The 300 ft high ziggurat or temple tower built in the city center of Babylon was made with clay mixed with finely chopped straw [1]. In recent years, polymeric based composite materials are being used in many applications, such as automotive, sporting goods, marine, electrical, industrial, construction, household appliances, etc. Polymeric composites have high strength and stiffness, light weight, and high corrosion resistance [2].

Nowadays market challenges, based on economy and efficiency of the manufacturing process, as well as various customers' needs, resulted in the development of new and high quality materials, such as composites. Scientists have defined composite materials in many ways [3, 4], but, the common idea of all these definitions is that composites represent artificial materials, made of two basic, not-mixable, components represented by the *matrix* and the *reinforcing elements* [5]. Composite materials (or composites for short) are engineered materials made from two or more constituent materials with significantly different physical or chemical properties which remain separate and distinct on a macroscopic level within the finished structure. The physical properties of composite materials are generally not isotropic (independent of direction of applied force) in nature, but rather are typically orthotropic (different depending on the direction of the applied force or load) [6]. In contrast, isotropic materials (for example, aluminum or steel), in standard wrought forms, typically have the same stiffness regardless of the directional orientation of the applied forces and/or moments [7]. The relationship between forces/moments and strains/curvatures for an isotropic material

can be described with the following material properties: Young's Modulus, the Shear Modulus and the Poisson's ratio, in relatively simple mathematical relationships. For the anisotropic material, it requires the mathematics of a second order tensor and up to 21 material property constants. For the special case of orthogonal isotropy, there are three different material property constants for each of Young's Modulus, Shear Modulus and Poisson's ratio—a total of 9 constants to describe the relationship between forces/moments and strains/curvatures [8].

A number of investigations have been conducted on several types of natural fibers such as kenaf, hemp, flax, bamboo, and jute to study the effect of these fibers on the mechanical properties of composite materials [9, 10, 11, 12]. Mansur and Aziz [1٠] studied bamboo-mesh reinforced cement composites, and found that this reinforcing material could enhance the ductility and toughness of the cement matrix, and increase significantly its tensile, flexural, and impact strengths. On the other hand, jute fabric-reinforced polyester composites were tested for the evaluation of mechanical properties and compared with wood composite [12]. A pulp fiber reinforced thermoplastic composite was investigated and found to have a combination of stiffness increased by a factor of 5.2 and strength increased by a factor of 2.3 relative to the virgin polymer [13]. In dynamic mechanical analysis, Laly et al., [13] have investigated banana fiber reinforced polyester composites and found that the optimum content of banana fiber is 40%. Mechanical properties of banana–fiber–cement composites were investigated physically and mechanically by Corbiere-Nicollier et al. [14]. It was reported that kraft pulped banana fiber composite has good flexural strength. Joseph et al. [15] tested banana fiber and glass fiber with varying fiber length and fiber content as well. The analysis of tensile, flexural, and impact properties of these composites revealed that composites with good strength could be successfully developed using banana fiber as the reinforcing agent. The source of banana fiber is the waste banana trunks or stems which are abundant in many places in the world. Therefore, composites of high–strength pseudo-stem banana woven fabric reinforcement polymer can be used in a broad range of applications. Wei Sun and Jerome in 2002 [16] developed model to predict the mechanical properties of the composite conductor based on two-level homogenization hierarchies. The developed model provides a theoretical basis and an accurate calculation for effective mechanical constants that are often difficult to be accurately determined through an experimental approach due to the structural heterogeneity and material anisotropy of the composite conductor. Wilson et al., in 2005 [17] developed Alumina-based composites in order to improve the mechanical properties of the monolithic matrix and to replace the WC-Co material for cutting tool applications. Al_2O_3

reinforced with refractory carbides improves hardness, fracture toughness and wear resistance to values suitable for metalworking applications. Al_2O_3-NbC composites were uniaxially hot-pressed at 1650 °C in an inert atmosphere and their mechanical properties and microstructures were analyzed. Maleque et al., 2007 [1] study the tensile, flexural, and impact properties of pseudo-stem banana fiber reinforced epoxy composites. They found that the tensile strength on the pseudo-stem banana woven fabric reinforced epoxy composite is increased by 90% compared to virgin epoxy. The results of the impact strength test showed that the pseudo-stem banana fiber improved the impact strength properties of the virgin epoxy material by approximately 40%. Higher impact strength value leads to higher toughness properties of the material. Maleque showed that the banana fiber composite exhibits a ductile appearance with minimum plastic deformation. Mihaiela et al., 2009 [5] represented experimental and theoretical studies for determining random reinforced glass fiber polymeric composite material mechanical characteristics, pointing out the importance of knowing real values of these characteristics in parts designing.

In this work resistible composites are suggested to be used instead of carbon steel pipes to overcome a number of common problems during commercial applications, especially the problem of fixing dead-beat carbon steel pipes within these systems. This work also studies the mechanical properties of resistible composites using ASTM to find the best conditions to create a system of pipes.

2. Theory

The use of the composite material in the engineering applications depends greatly on its good mechanical properties, especially its high strength and low weight [18]. Generally the mechanical properties describe the behavior of the composite material under the influence of different forces [19].

2.1 Flexural Strength (F.S.) ASTM-D790

The flexural test measures the force required to bend a beam under three point loading conditions. The data is often used to select materials for parts that will support loads without flexing. Flexural modulus is used as an indication of a material's stiffness when flexed. Since the physical properties of many materials (especially thermoplastics) can vary depending on ambient temperature, it is sometimes appropriate to test materials at

temperatures that simulate the intended end user environment [20]. The capability of composite material to bend under centric stresses was located using the following equation:

$$F.S. = \frac{3pL}{2bd^2} \quad (1)$$

and

$$\tau = \frac{3p}{4bd} \quad (2)$$

2.2 Bending ASTM-D790

An **elastic modulus**, or **modulus of elasticity**, is the mathematical description of an object or substance's tendency to be deformed elastically (i.e., non-permanently) when a force is applied to it [21]. The elastic modulus of an object is defined as the slope of its stress-strain curve in the elastic deformation region:

$$\lambda \stackrel{\text{def}}{=} \frac{\text{stress}}{\text{strain}}$$

Where lambda (λ) is the elastic modulus; *stress* is the force causing the deformation divided by the area to which the force is applied; and *strain* is the ratio of the change caused by the stress to the original state of the object. If stress is measured in pascals, since strain is a unitless ratio, then the units of λ are pascals as well [22].

Since the denominator becomes unity if length is doubled, the elastic modulus becomes the stress needed to cause a sample of the material to double in length. While this endpoint is not realistic because most materials will fail before reaching it, it is practical, in that small fractions of the defining load will operate in exactly the same ratio. Thus for steel with an elastic modulus of 30 million pounds per square inch, a 30 thousand psi load will elongate a 1 inch bar by one-thousandths of an inch, and similarly for metric units, where a thousandth of the modulus in Giga Pascal will change a meter by a millimeter.

Specifying how stress and strain are to be measured, including directions, allows for many types of elastic module to be defined. The three primary ones are:

- *Young's modulus* (*E*) describes tensile elasticity, or the tendency of an object to deform along an axis when opposing forces are applied along that axis; it is defined as the ratio of tensile stress to tensilestrain. It is often referred to simply as the *elastic modulus*.
- The *shear modulus* or *modulus of rigidity* (*G* or μ) describes an object's tendency to shear (the deformation of shape at constant volume) when acted upon by opposing forces; it is defined as shear stress over shear strain. The shear modulus is part of the derivation of viscosity.
- The *bulk modulus* (*K*) describes volumetric elasticity, or the tendency of an object to deform in all directions when uniformly loaded in all directions; it is defined as volumetric stress over volumetric strain, and is the inverse of compressibility. The bulk modulus is an extension of Young's modulus to three dimensions.

From the change of deflection caused by variable masses, the specific modulus of elasticity (E) can be calculated from the following equation [21]:

$$E = \frac{mgL^3}{48fI} \tag{3}$$

(Mass/deflection is the slope of the curve)

(Which means load/ deflection is the slope of the curve)

I is the moment of inertia and:

$$I = {bt^3}/{12} \tag{4}$$

2.3 Impact Strength ISO-179

Because of the outer impacts on the composite materials in the industry, this test is important. The fracture means the separation or fragmentation of a solid body into two parts or more under the influence of a stress higher than it can bear, that means it consists of two stages, the first is crack initiation and the other is crack propagation [23]. The impact strength can be calculated from the following equation [22]

$$Impact\ strength = \frac{U}{A} \tag{5}$$

2.4 Brinell Hardness

The Brinell scale characterizes the indentation hardness of materials through the scale of penetration of an indenter, loaded on a material test-piece. It is one of several definitions of hardness in materials science. Johan August Brinell proposed the brinell scale in 1900; it was the first widely used and standardized hardness test in engineering and metallurgy. The large size of indentation and possible damage to test-piece limits its usefulness[24]. The typical test uses a 10 mm diametersteel ball as an indenter with a 3,000 kgf (29 KN) force. For softer materials, a smaller force is used; for harder materials, a tungsten carbide ball is substituted for the steel ball [26]. The Brinell hardness (Br. H.) is an important surface mechanical property and it's known as a resistance of the material to deform [21]. The Brinell hardness can be calculated from the following equation:

$$\mathrm{HBW} = 0.102\frac{2F}{\pi D(D-\sqrt{(D^2-d^2)})} \tag{6}$$

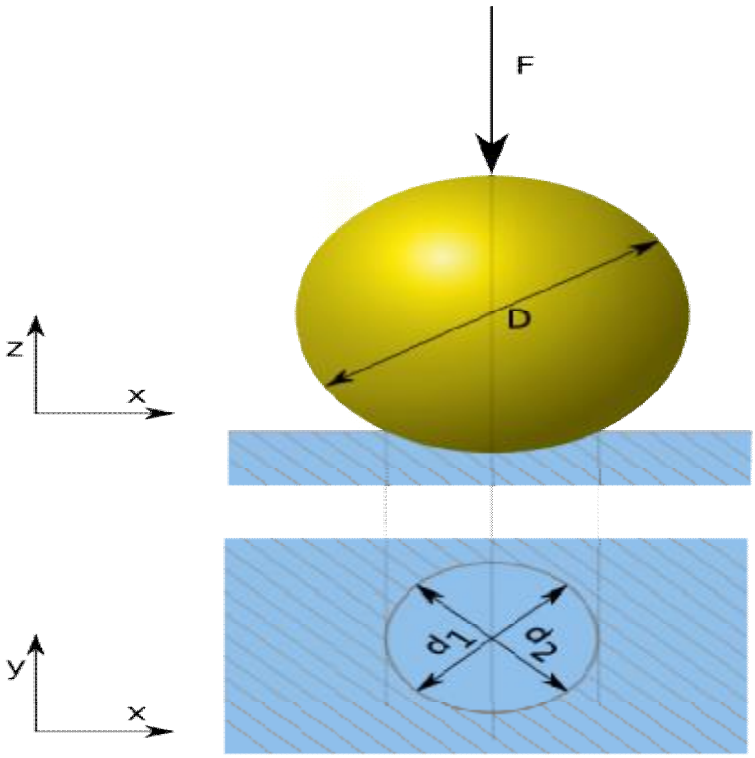

Figure (1). Force diagram.

3. Experimental work

Four mechanical tests were made to the composites and to the carbon steel specimens to make a good comparison between them:

3.1 Impact Strength (ISO-179)

The impact strength test was made by using Charpy impact device. The dimensions for the specimens used were 6*2*0.6 cm. The device consists of a pendulum hummer with an energy gage to measure the energy needed to break the specimen (breaking energy, j). Equation (5) was used to calculate the impact strength.

3.2 Bending Test (ASTM D-790)

The bending test device of Phywe Company was used to calculate the modulus of elasticity of the composite specimens 10*1*0.5 cm. The masses were hanged in the middle of the specimen using a holder. These masses will cause a deflection in the specimen, that measured by a deflection gage. Equations (3) and (4) were used to calculate the specific modulus of elasticity.

3.3 Flexural Strength (ASTM D-790)

Most commonly the specimen lies on a support span and the load is applied to the center by the loading nose producing three points bending at a specified rate [25]. The parameters for this test are the support span, the speed of the loading, and the maximum deflection for the test [26]. These parameters are based on the test specimen thickness and are defined differently by ASTM and ISO. For ASTM D790, the test is stopped when the specimen reaches 5% deflection or the specimen breaks before 5%. For ISO 178, the test is stopped when the specimen breaks. If the specimen does not break, the test is continued as far as possible and the stress at 3.5% (conventional deflection) is reported.

The test carried out made using a hydraulic compressor of Ley Bold Harris No.36110 type. The dimensions of the specimens were 10*1*0.5 cm. This test (three-point test) was carried out using the apparatus shown in figure (2) and with the gage in the hydraulic compressor; the load needed to break the specimen was read. Equations (1) and (2) were used to calculate the flexural strength and shear stress.

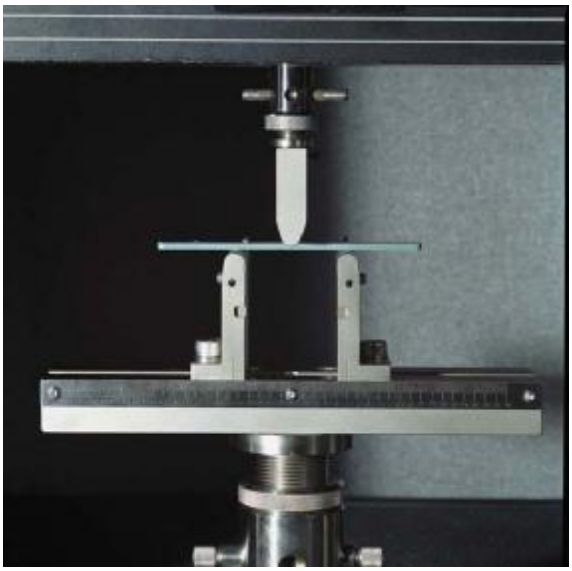

Figure (2). Flexural apparatus.

3.4 Brinell Hardness Test

Using a carbide ball penetrator, and applying loads of up to 3,000 kgf, Brinell hardness tester following ASTM E-10 is widely used on castings and forgings. This method requires optical reading of the diameter of ball indentation, and using a chart to convert the average measurement to Brinell hardness value.

The same hydraulic compressor was used with a stainless-steel semi-cone with diameters of the free end 5.0 and 2.5 mm, respectively. A specific load was put on the specimen for about 10-15 seconds, and then was appeared a hole on the specimen with specific diameter. Equation (6) was used to calculate Brinell hardness was found.

4. Results and discussion

4.1 Bending test

The important goal from this test is to see the Hookean behavior for the material under loading. Figures (3), (4) and (5) show that the deflection was increased proportionally with the load on the specimen and when the load disappears the specimen goes to its original state and it means that these specimens were under Hook's law. Also the percentage between mass deflections is constant and represents the slope in all these figures by using equations (3) and (4) to calculate the specific modulus of elasticity (E) for all the specimens (8-spesimens).

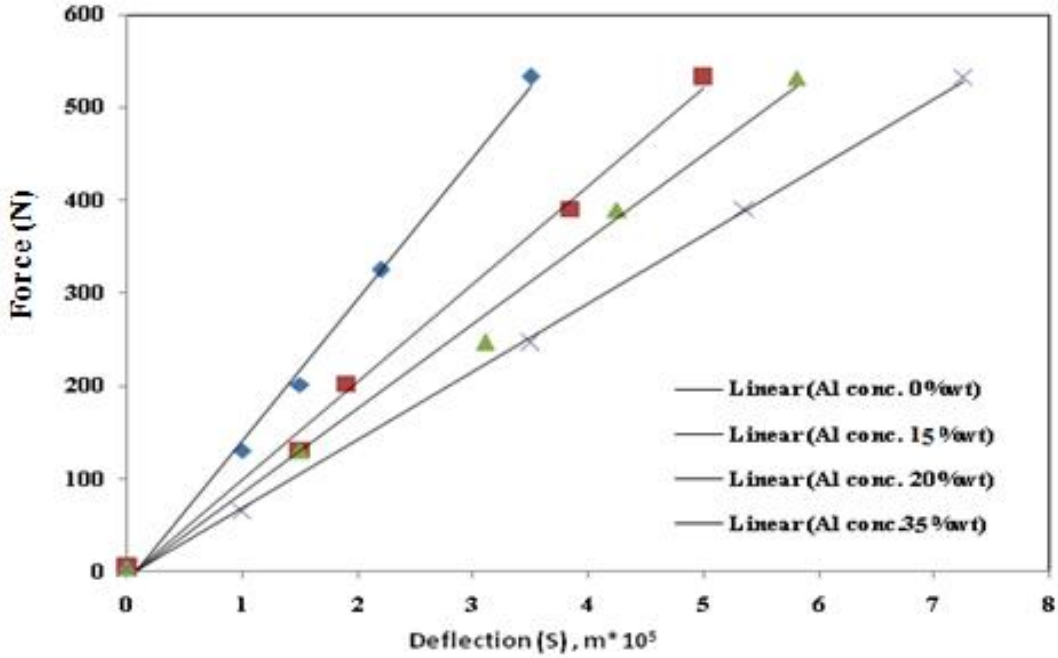

Figure (3) .Deflection against force of bending test.

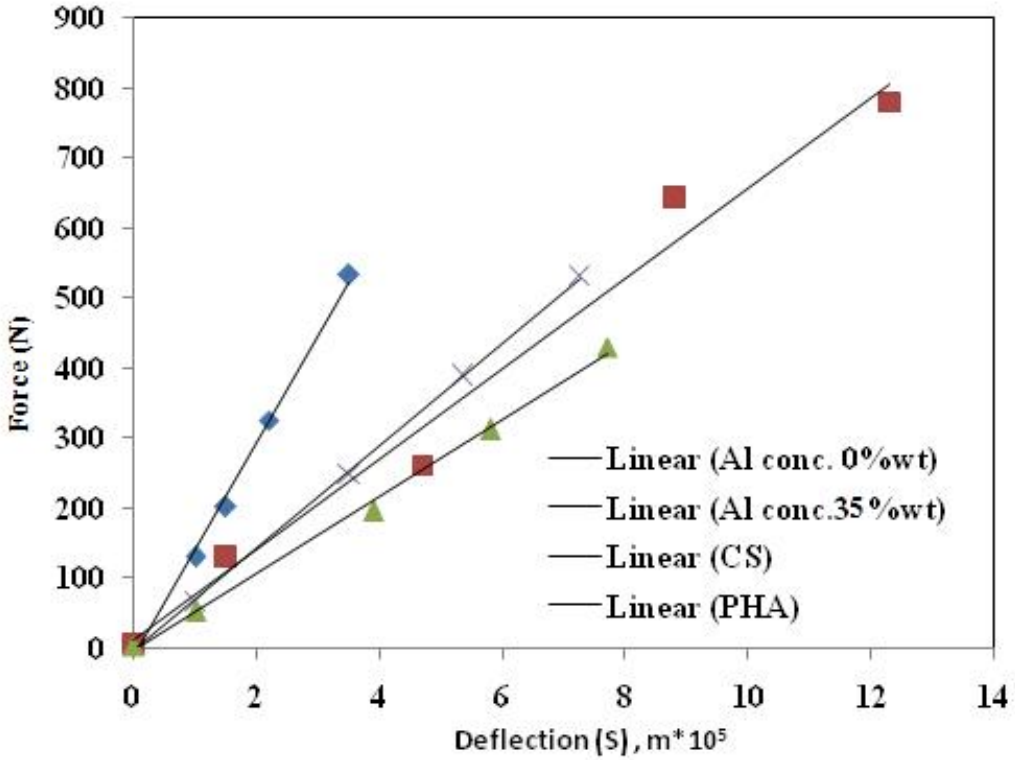

Figure (4). Deflection against force of bending test.

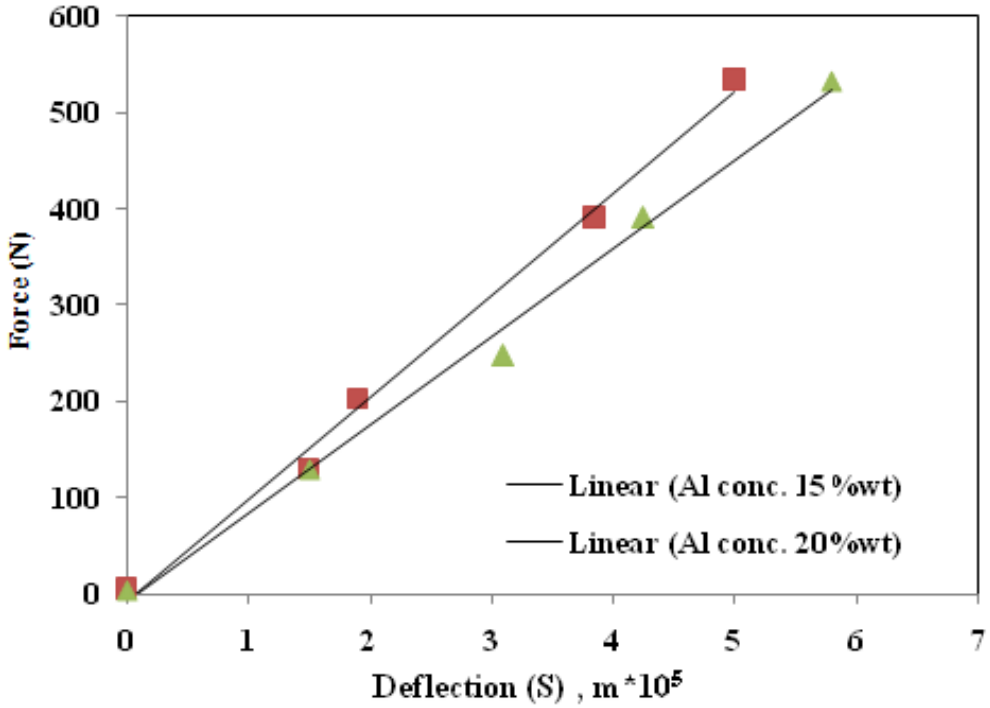

Figure (5). Deflection against force of bending test.

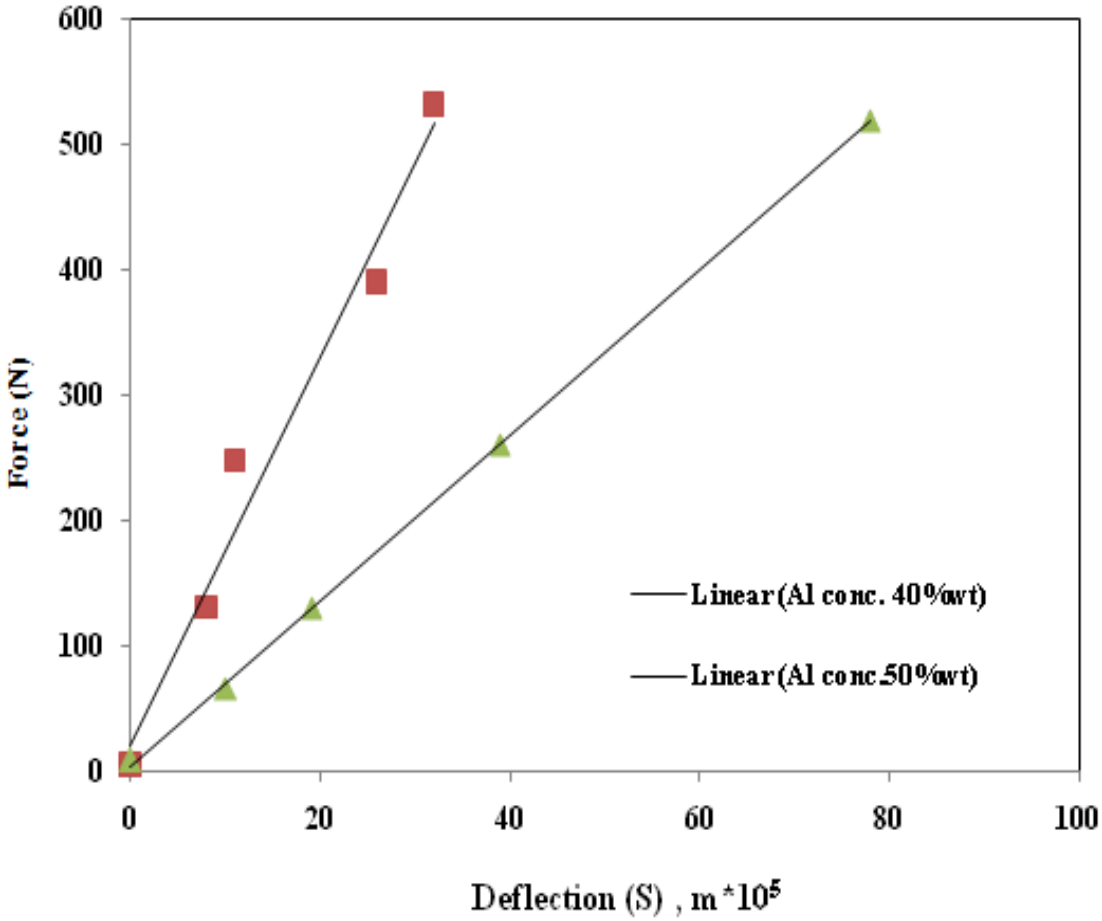

Figure (6) .Deflection against force of bending test.

Figure (6) shows that the samples of 40 and 50 wt % aluminum powder show a high influence of deflection than the other samples.

Figure (7) below shows that the specific modulus inversely proportional with the aluminum powder concentration, it decreases when the aluminum powder concentration in the specimens' increases and that means the cross-link density between the unsaturated polyester molecules decreases with increasing the aluminum powder concentration. It can be seen that the specific modulus of the aluminum honeycomb was low compared with the other specimens; this means that the glass fiber departs loads more than the aluminum honeycomb.

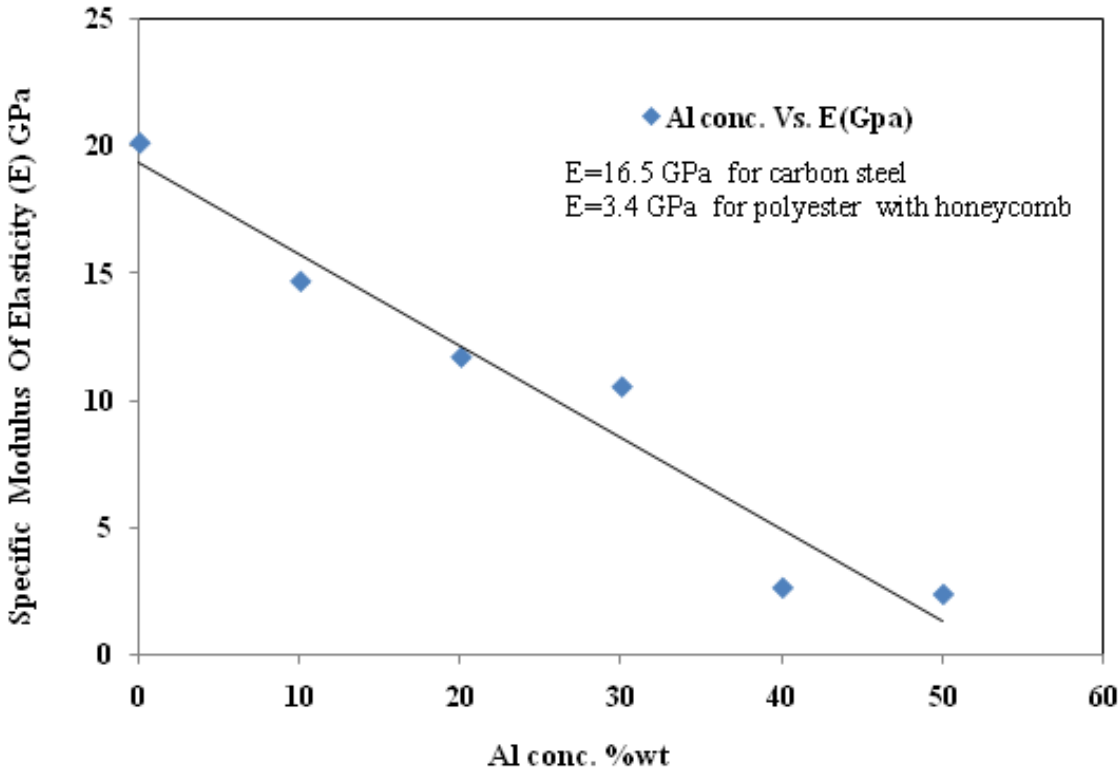

Figure (7). Effect of Aluminum powder concentration on the specific modulus.

4.2 Flexural strength test

This test was used to specify the highest twisting stress that the specimens can afford. There are three kinds of failure happened at different places in the same time and its [26]:

1. The tensile stresses failure:

This will cause matrix chapping and will load the fibers to be on the surface and when the load increases this chapping will grow faster from fiber to another in the transverse direction.

2. Compressive stresses failure:

   At usual the primary failure of the specimens in this test will happen on the other surface of these specimens. This compression will cause a micro-buckling phenomenon to the fiber and when the loading increases the fibers will breakout.

3. Shear stresses failure:

   The generated shear chapping could grow both in transverse and longitudinal directions. When the cross-link density between the fibers and the polymer and the polymer itself increases, the shear strength will increase too. There are many factors that influence these failure kinds such as: the fiber type, the fiber length and diameter, the fiber direction and the volume fraction of the fiber [23].

Figure (8) represents the failure happened on the prepared samples by the flexural strength test.

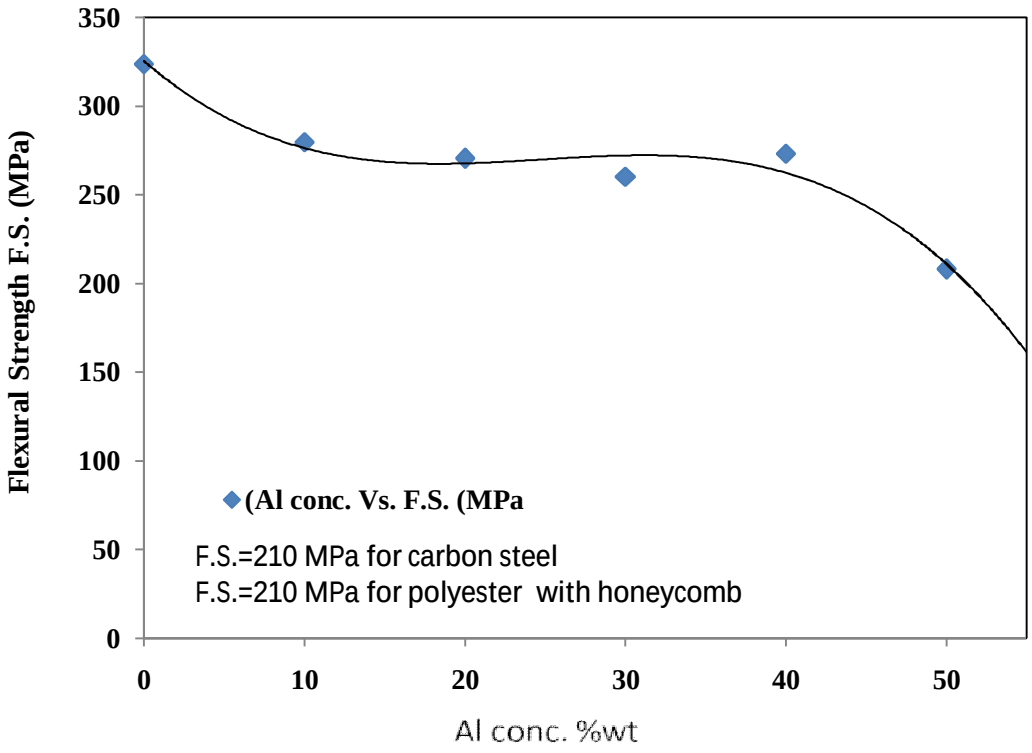

Figure (8) .Effect of Aluminum powder concentration on the flexural strength.

Figures (8) and (9) show the effect of the aluminum powder concentration in the specimens, on the flexural strength and shear stress it can be seen that when the concentration of the aluminum powder increases the flexural strength and shear stress decreases because of the particles of the aluminum powder decreases the cross-link density of the polymer with the glass fiber and with each other. Also it can be seen from that shear stress values are very much less than the flexural strength because it is only a surface stresses, not for all the body.

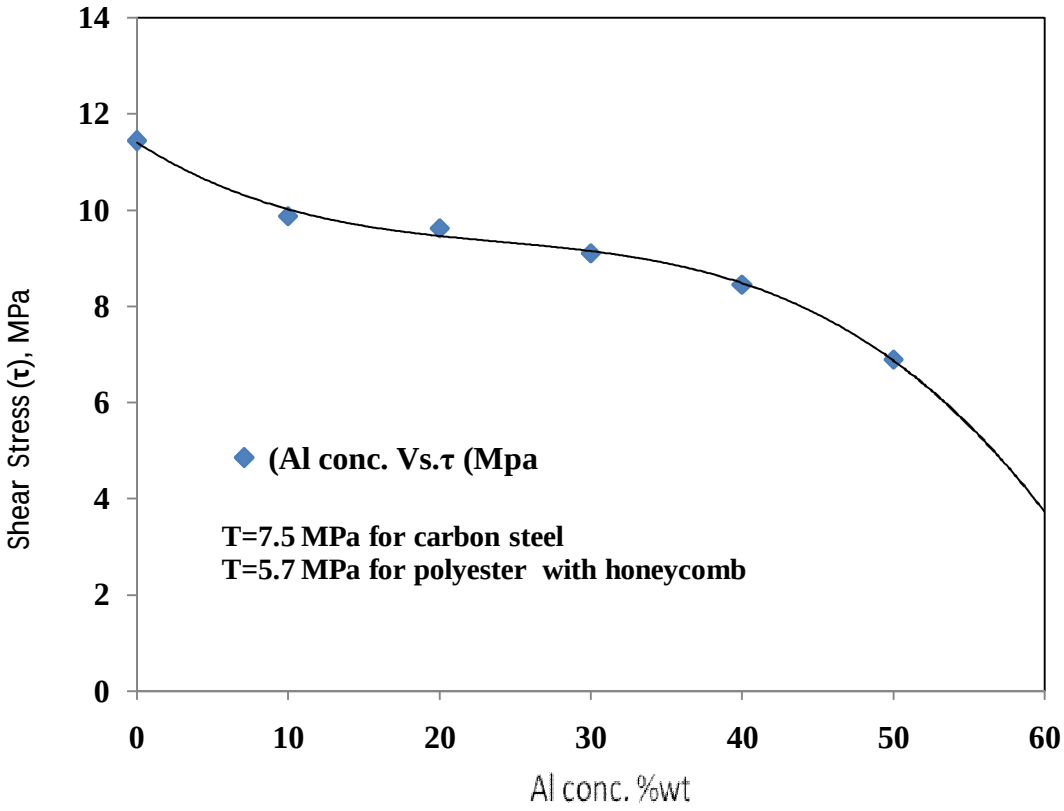

Figure (9). Effect of Aluminum powder concentration on the shear strength .

4.3 Impact test

The failure caused by fast stresses is one of the most mechanical properties that get attention lately, because sometimes the polymeric material is flexible under static stresses, but it looks like a shooing one under fast stresses [21].

Equation (5) has been used to calculate the impact strength for all the specimens. From Figure (10) below it can be seen clearly that when the aluminum powder concentration

increases, the impact strength decreases, while the carbon-steel specimens have the highest value of impact strength because it's a flexible material.

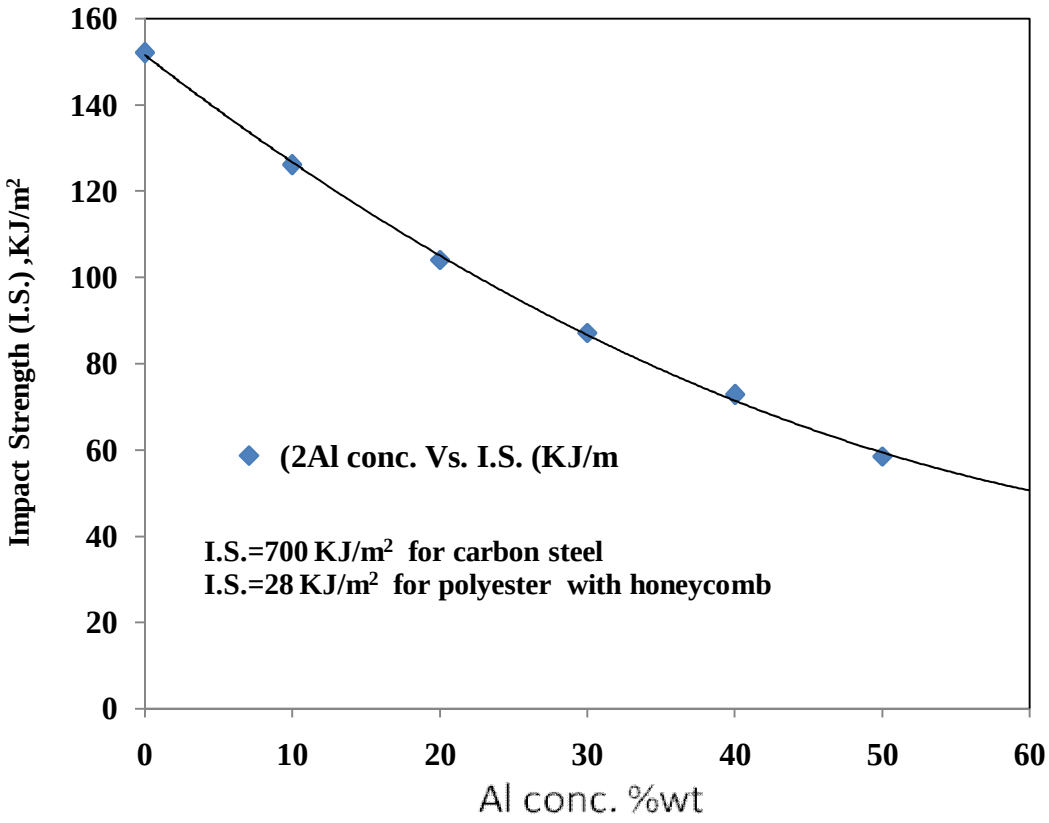

Figure (10). Effect of Aluminum powder concentration on the impact stress.

4.4 Brinell Hardness Test

Brinell hardness (Br. H.) test is used to measure the resistance of the material to plastic deformation on the surface.

Figure (11) shows the values of Br. H. calculated from equation (6), it can been seen that when the aluminum powder concentration increasing, the Br. H. decreasing and this means that the particulate filler minimizing the mechanical properties values specially when adding a 40-50 wt% of aluminum powder. While at 0, 15, 20 and 3°wt% samples the mechanical properties values were close to of carbon-steel specimen, while the aluminum honeycomb has a different mechanical property.

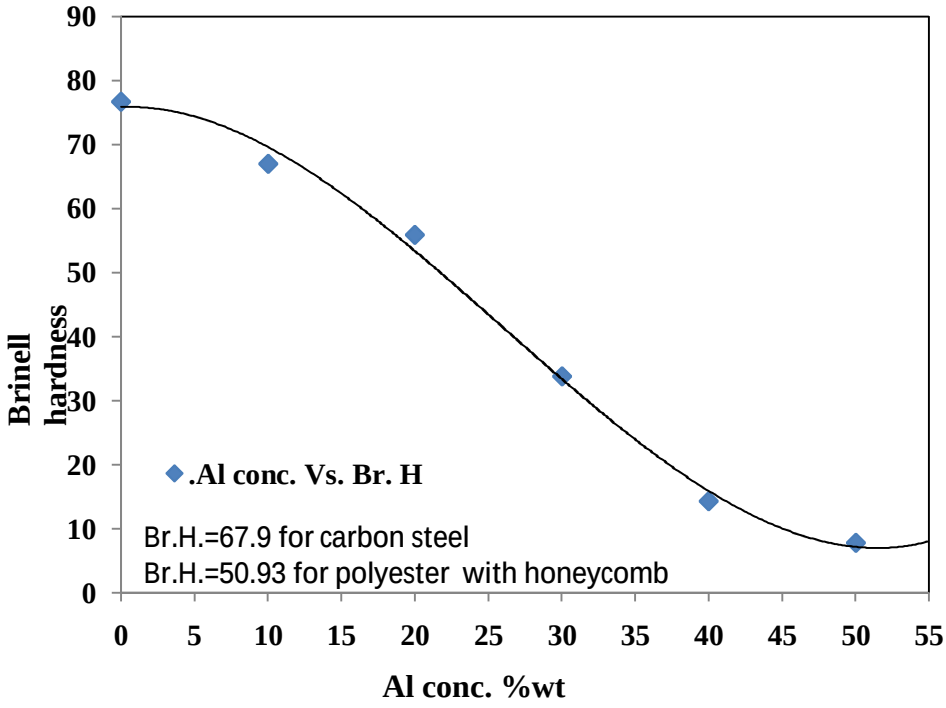

Figure (11) .Effect of Aluminum powder concentration on the Brinell hardness.

5. Conclusions

In this work, the specimens were under Hook's law this is because the proportionally increasing of the deflection with the load on the specimen, as well as when the load disappears the specimen goes to its original state.

The cross-link density between the unsaturated polyester molecules decreases with increasing aluminum powder concentration. The mechanical properties decrease with the increasing of aluminum powder concentrations.

The glass fiber departs loads more than the aluminum honeycomb, this is due to the fact that the specific modulus of the aluminum honeycomb was low compared with the other specimen.

Increasing the aluminum powder concentration led to a decrease in the impact strength, while the carbon-steel specimens have the highest value of impact strength because it's a flexible material.

The most suitable weight percent of the aluminum powder is 3°wt% which gives mechanical properties values close to the mechanical properties of carbon-steel. Aluminum honeycomb samples were very good mechanical properties suitable for certain applications such as aircraft engine parts, spacecraft parts, assemblies,air/light directionalization, energy absorption, etc..

6. References

[1] M. A. Maleque, F. Y. Belal and S.M. Sapuan, 2007, "Mechanical Properties Study Of Pseudo-Stem Banana Fiber Reinforced Epoxy Composite". *The Arabian Journal for Science and Engineering*, Vol. 32, No. 2B, pp. 359-364.

[2] F. T. Wallenberger and N. Weston, 2004 "Natural Fibers, Plastics and Composites Natural", *Materials Source Book* from C.H.I.P.S. Texas.

[3] G. Zgura and I. Severin, 1999, "Caracterizareamaterialelor composite cu matricemetalicaprintehniciavansate de investigare", Editura BREN, Bucuresti.

[4] G. Iordache., 1996, "Componente de maºini din material polimerice". Calcul. Constructie. Tehnologie; EdituraTehnica, Bucuresti.

[5] I. Mihaiela, S. Paulina, N. Emil and LiviuMihon, 2009, "Experimental and Theoretical Studies on Mechanical Characteristics of an Important Composite Material". Materiale Plastic, Vol. 46, No. 1, pp. 62-66.

[6] "Rubbn' Repair Composite Repair System". CRG Industries, LLC. Retrieved 2009-10-02.http://www.rubbnrepair.com/

[7] L. A. Pothan, T. Sabu, and Neelakantan, 1997, "Short Banana Fiber Reinforced Polyester Composites: Mechanical, Failure and Aging Characteristics", *J. Reinforced Plastics and Composites*, **16**(**8**), pp. 744–765.

[8] K. G. Satyanarayana, K. Sukumaran, P. S. Mukherjee, C. Pavithran and S. G. K. Pillai, 1990, "Natural Fiber–Polymer Composites", *J Cement and Concrete Composites*, **12**(**2**), pp. 117–136.

[9] K. G. Satyanarayana, K. Sukumaran, A. G. Kulkarni, S. G. K. Pillai, and P. K. Rohatgi, 1986, "Fabrication and Properties of Natural Fiber-Reinforced Polyester Composites", *J. Composites*, **17**(**4**), pp. 329–333.

[10] M. A. Mansur and M. A. Aziz, 1983, "Study of Bamboo-Mesh Reinforced Cement Composites" *Int. Cement Composites and Lightweight Concrete*, **5**(**3**), pp. 165–171.

[11] T. M. Gowda, A. C. B. Naidu, and R. Chhaya, 1999, "Some Mechanical Properties of Untreated Jute Fabric-Reinforced Polyester Composites", *J. Composites Part A: Applied Science and Manufacturing*, **30**(**3**), pp. 277–284.

[12] L. Lundquist, B. Marque, P. O. Hagstrand, Y. Leterrier and J. A. E. Månson, 2003, "Novel Pulp Fiber Reinforced Thermoplastic Composites", *Composites Science and Technology*, **63**(**1**), pp. 137–152.

[13] A. LalyPothana, O. Zachariah and Sabu Thomas, 2003, "Dynamic Mechanical Analysis of Banana Fiber Reinforced Polyester Composites", *Composites Science and Technology*, **63(2)**, pp. 283–293.

[14] T. Corbière-Nicollier, B. G. Laban, L. Lundquist, Y. Leterrier, J. A. E. Månson, and O. Jolliet, 2001, "Life Cycle Assessment of Biofibers Replacing Glass Fibers as Reinforcement in Plastics", *Resources, Conservation and Recycling*, **33(4)**, pp. 267–287.

[15] S. Joseph, M. S. Sreekala, Z. Oommen, P. Koshy, and T. Sabu, 2002, "A Comparison of the Mechanical Properties of Phenol Formaldehyde Composites Reinforced with Banana Fibers and Glass Fibers", *Composites Science and Technology*, **62(14)**, pp. 1857–1868.

[16] Wei Sun and Jerome T. Tzeng, 2002, "Homogenization Modeling for Mechanical Properties of Composite Conductor with Cooling Channel". *Army Research Laboratory*, Aberdeen Proving Ground, MD 21005-5069, ARL-TR-2872.

[17] A. Wilson, A. C. Carlos and M. S. Ana, 2005, "TEM study of a hot-pressed Al_2O_3-NbC composite material". Materials Research. Vol.8, No.1, pp. 26-29.

[18] د. اكرم عزيز محمد، "كيمياء اللدائن" ، دار الكتب للطباعة و النشر، جامعة الموصل (١٩٩٣)

[19] M. D. Baijal, 1982, "Plastics polymer science and technology", John Wiley and sons, New York.

[20] Telf, G. and Clarin, P., 1984, "Fiber science and technology", Vol. 21, No. 4, pp 319-326.

[21] ديتر، جي. اي.، ترجمة د.عبد الرزاق اسماعيل خضر و د.عبد الوهاب محمد عبد الله، " المتالوجيا الميكانيكية"، الجامعة التكنلوجيه، قسم هندسة الانتاج و المعادن، ١٩٩٤.

[22] D. Tabor, (2000), The Hardness of Metals, Oxford University Press, ISBN 0198507763, http://books.google.com/books?id=b-9LdJ5FHXYC

[23] ASTM, 1984, "Annual Book of ASTM Standards", Vol. 8.02.

[24] Callister, W. D., 1999, "Material Science and Engineering", 5th Ed.

[25] W. Y. Chiang and S. Y. Yang, 1989, *J. App. Polymer Sci.*, Vol. 37, Pp 499-512.

[26] G. C. Shin and L.J. Ebert, 1986, *J. Composites*, Vol. 17, No. 4, Pp 309-320.

7. Nomenclature

A Cross-sectional area of the sample (m^2)

.b Width of the specimen (m)

D Stainless-steel semi-cone diameter (mm)

.d Diameter of the hall on the specimen (mm)

F Loaded force (KN)

f Deflection

F.S. Flexural strength (MPa)

g Acceleration 9.81 m/s^2

L Length of the specimen (m)

m Mass (kg)

.τ Shear stress (MPa)

p Load (N)

.t Thickness of the specimen (m)

U Breaking energy (J)

Microstructural Investigation on Severe Cold work and Treated Copper Drawn Wires

Adnan A.Ugla, Khalid A. M. ,Talib H. A. , Sadiq M. I. and Fadhil A.H.

Mechanical Engineering Department

College of Engineering

Thi-Qar University

Abstract

The aim of this work is to study the microstructure of severe cold work copper wires, which its already processed at Ur Foundation (Nasyeria) which in Ur are cold drawn from 10 mm to 2 mm in diameter, then at final process it will be treated automatically by treated box by 200^{o} C (semi treatment). Our work dealing with taken the final drown wire (2 mm in dia.) and doing a laboratory treatment by 200^{o} C, 300^{o} C, 400^{o} C, and 500^{o} C, one hour at this temperature and the furnace cooled. The result which concluded that the Ur treatment is hot full treatment but a stress relief one with almost same wire property. While the treated wires show a recrystallized structure with inclination by 45^{0} angle for this structure. The high treated temperature shows grain growth and demises the 45^{0} angle structure.

المستخلص

تهدف هذه الدراسة إلى التعرف على البنية البلورية للأسلاك النحاسية بعد إجراء عمليات السحب على البارد ولنسبة سحب أكثر من ٩٠% وما ينشأ عن ذلك خلال إجراء المعاملة الحرارية التي تبدأ من الاسترجاع (Recovery) وصولاً إلى إعادة التبلور و التي من خلالها يمكن التعرف على تأثيرها في استخدامات هذه الأسلاك. حيث تم استخدام أسلاك نحاسية مسحوبة من قطر ١٠ ملم و لغاية ٢ ملم و خلال أكثر من عشرة مراحل سحب على البارد ثم في نهاية المطاف أخذت عينات من تلك الأسلاك و أجريت عليها معاملة حرارية بدرجات حرارية ٢٠٠ م، ٣٠٠ م، ٤٠٠ م ، و ٥٠٠ م داخل الفرن و لفترة ساعة واحدة ثم تركت تبرد في داخل الفرن الحراري عند تلك الدرجة الحرارية وتم مقارنة البنية البلورية لتلك الأسلاك مع السلك الذي يجرى عليه معاملة حرارية بدرجة ٢٠٠ م بعد سحبه داخل وحدة المعالجة الحرارية المرفقة مع ماكنة السحب. كل عمليات السحب أجريت في شركة اور (الناصرية) اما المعاملة الحرارية فاجريت في مختبرات كلية الهندسة-جامعة ذي قار. كانت النتائج قد بينت ان بنية السلك في نهاية عمليات السحب الى قطر ٢ملم دون اي معاملة حرارية لا توجد اي حدود بلورية وكانت البنية محطمة نهائياً نتيجة السحب العالي بحدود ٩٦% CW. اما السلك المعامل في شركة أور فانه يبين ذات البنية التي حصلنا عليها دون المعاملة الحرارية، اما السلك المعامل في المختبر بدرجة حرارة ٢٠٠ م فانه يبين بداية اعادة بناء و تبلور بزاوية اقل من 45^{0}. اما السلك المعامل بدرجة حرارة 400^{o} C فانه أعيدت حبيباته إلى الوضع الطبيعي.

1. Introduction

High quality wires have been widely used as electrical wires in microelectronics, telecommunication, network and transportation. Several approaches have been developed to manufacture copper wires, such as continuous casting and rolling, dipping and upward casting. However, the electrical conductivity and elongation of the copper wires with polycrystals fabricated by these approaches are limited due to transverse grain boundaries in the rods. Besides, fabrication of fine Cu wires without breaking is another challenge and many efforts to solve the problem have been made [1-4].

2. Effect of Cold Work on Recrystallization of Copper Wire During Drawing Process

Recrystallization is the rearrangement of the atoms or molecules of the solid into an entirely new set of crystals. This results in drastic changes in the properties such as tensile strength and ductility. For cold-worked metals and alloys recrystallization usually occurs at temperatures of about 0.3 T_m in pure metals and of about 0.5 T_m in alloys [5]. Recrystallization results in the formation and growth of new grains. Distorted elongated grains disappear, and new grains are formed. During the period of grain growth, the layer recrystallized grains grow at the expense of the smaller ones (figure 1) [6]. The temperature of recrystallization depends on the degree of deformation of cold –worked metal. The greater the degree of work hardening is, the lower the temperature of recrystallization is. Also, the purer the metal is, the lower the recrystallization temperature is. There is a value of strain, called the critical strain, below which there is no recrystallization (figure 2) [6]. At this critical strain a few recrystallized grains form and grow extremely large. This technique is some times used to grow single crystals (table1).

Table (1). Recrystallization and melting temperatures of some metals, ^{o}C[6].

metal	recrystallization	melting	Metal	recrystallization	melting
Al	150	660	Ni	620	1452
Cd	50	321	Pt	450	1710
Cu	200	1083	Ag	200	960.5
Fe	450	1535	Ta	1020	3000
Pb	0	327	Sn	0	232
Mg	150	651	W	1210	3400

Cold work processes are accompanied by a marked decreases in ductility and a slight decrease in density and in electrical conductivity. The cold work distorts the equated microstructure of metals, causes the formation of crystal defects, particularly dislocations, and frequently results in elongated grains in the direction of deformation. The percent of cold work (CW) can be calculated from reduction in thickness or in area as follows:

$$\% CW = 100(d_o^2-d^2)/d_o^2 \quad \text{or} \quad \%CW = 100(A_o-A)/A_o$$

Where d_o is the initial thickness, d is the thickness after deformation, A_o is the initial cross-section area, and A is the cross-section area after deformation [7-8].

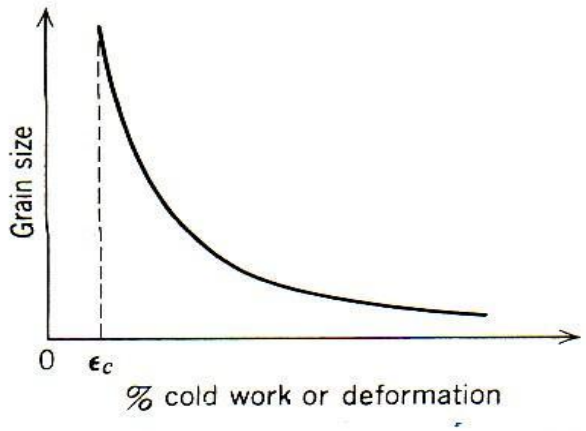

Figure (1). Effect of cold work on recrystallized grain is the critical strain below which there is no recrystallization [5].

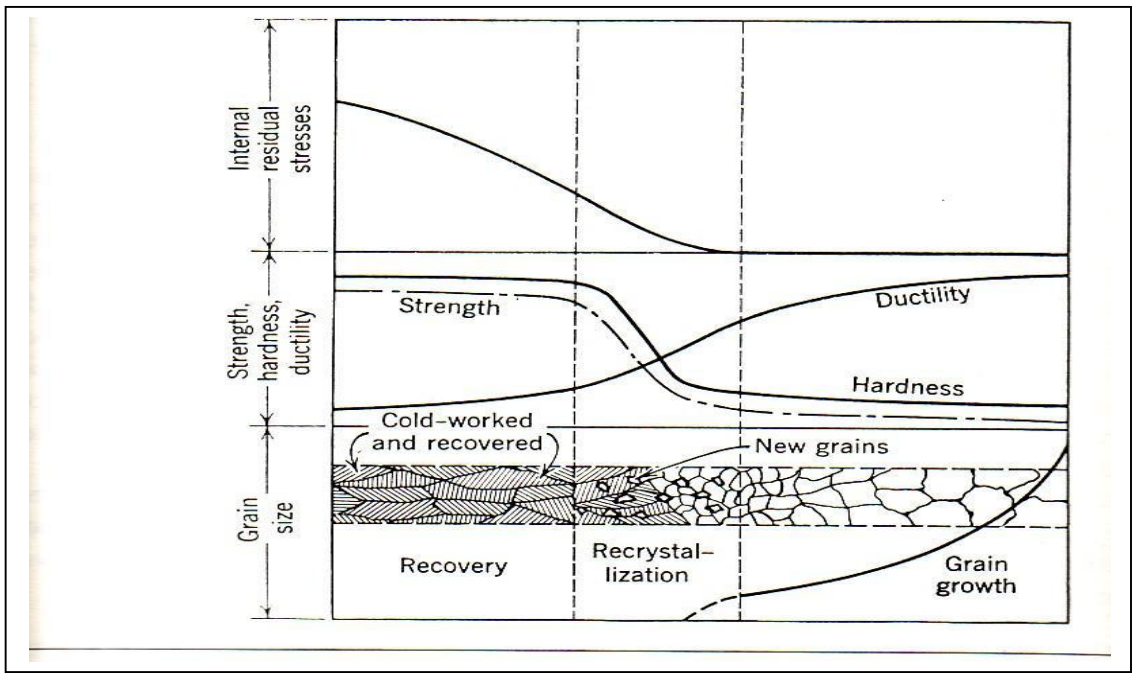

Figure (2). Effect of annealing on cold – worked metal[5].

3. Experimental work

Twelve specimens were taken. Two specimens drawn to 2mm diameter without treatment, two specimens treated by Ur process, eight specimens (2mm diameter) heated to 200^o C, 300^o C, 400^o C, and 500^{o}C which staying one hour at each temperature and finally furnace cooled. Optical microstructures were reveals by well preparation (grinding and polishing) for these twelve specimens and then examined by optical microscope.

4. Results and discussion

From the samples microstructure for the different treated drowns copper wires. The cold drawing is reach 100% cold worked samples. Which calculated by the below formula:

$\%CW = 100(A_o-A)/ A_o$

Where : A_o = original area mm^2

A = final area mm^2

This type of cold work will increase the wire hardness to duplicate [9]. The structure of this wires was shown in figure 3-a.The destroyed lamellar structure wasshown clearly in figure 3-b.

Figure 2 points out the Ur treated process which showed clearly the lamellar structure with out any recrystallization process as in (a) and (b). Figures 5 and 6 represent the samples which were full treated at 200 C^0. From these figures, it can be clearly shown the organized oriented at 45^0 angles of the started recrystallized grains with lamellar structure. The recrystallization process which accumulated in , 45^0angles, is likely happens as Lüder bands in tensile yielding, which may can explain due to well- defined yielding, the unlocking of dislocation that occurs at the upper yield point is a localized phenomenon. The unlocked dislocation move at a very high speed, because the stress required to unlock is much higher than the stress required to move them, until they are stopped at grain boundaries [9]. For this reason that drawing will done by more than one stage (in this work about ten stages from 10mm to 2mm in diameter). The clearly etched figure 5 and 6 showing that the high energy inclined lines (by 45^o) due to the dislocation moving clearly appear by the treatment process (200^{o}C) which is in recrystalization temperature. And by increasing the treatment temperature

these inclined lines will disappear and by 400°C and 500°C, figures 8 and 9 shows horizontal lines (energy lines).

5. Conclusions

The main conclusion from this work is that the severe cold work [more than 96% CW] will lead to make easy the dislocation movement at or near the grain boundaries in destroyed structure. This will be preferred to make growth at 45° angles. And this phenomenon is likely to the slipping process in tensile testing for metals (Lüder bands).

6. References

[1] B. Aritzur, Trans, ASME Ser B90(1968) 79-91.

[2] C.C.Chen,S.I.Oh,S.Kobayashi,Trans,ASME.101(1979) 23-44.

[3] H. Tanaka, K. J. Yoshida. Jpn. Inst.Met. 43(1979) 618-625.

[4] H. Tanaka, K. J. Yoshida. Jpn. Soc. Technol. Plasticity24 (1983) 737-743.

[5] Zbigniew D. Jastrezebski, " The Nature and Properties of Engineering Materials" , Second Edition, John Wiley and Sons, 1977.

[6] Argon, A. S., Editor Physics of Strength and Plasticity, The M.I.T. Press, Cambridge, Mass , 1969.

[7] Cottrell, A. H., The Mechanical Properties of Matter, John Wiley and Sons, Inc, New Tork, 1964.

[8] Honeycmbe, R.W.K., The Plastic Deformation of Metals, Edward Arnold, Ldt., Lendon, 1968.

[9] M. A. Meyers, and K.K. Chawla " Mechanical Behavior of Materials", Prentice Hall, New Jersey, 1999.

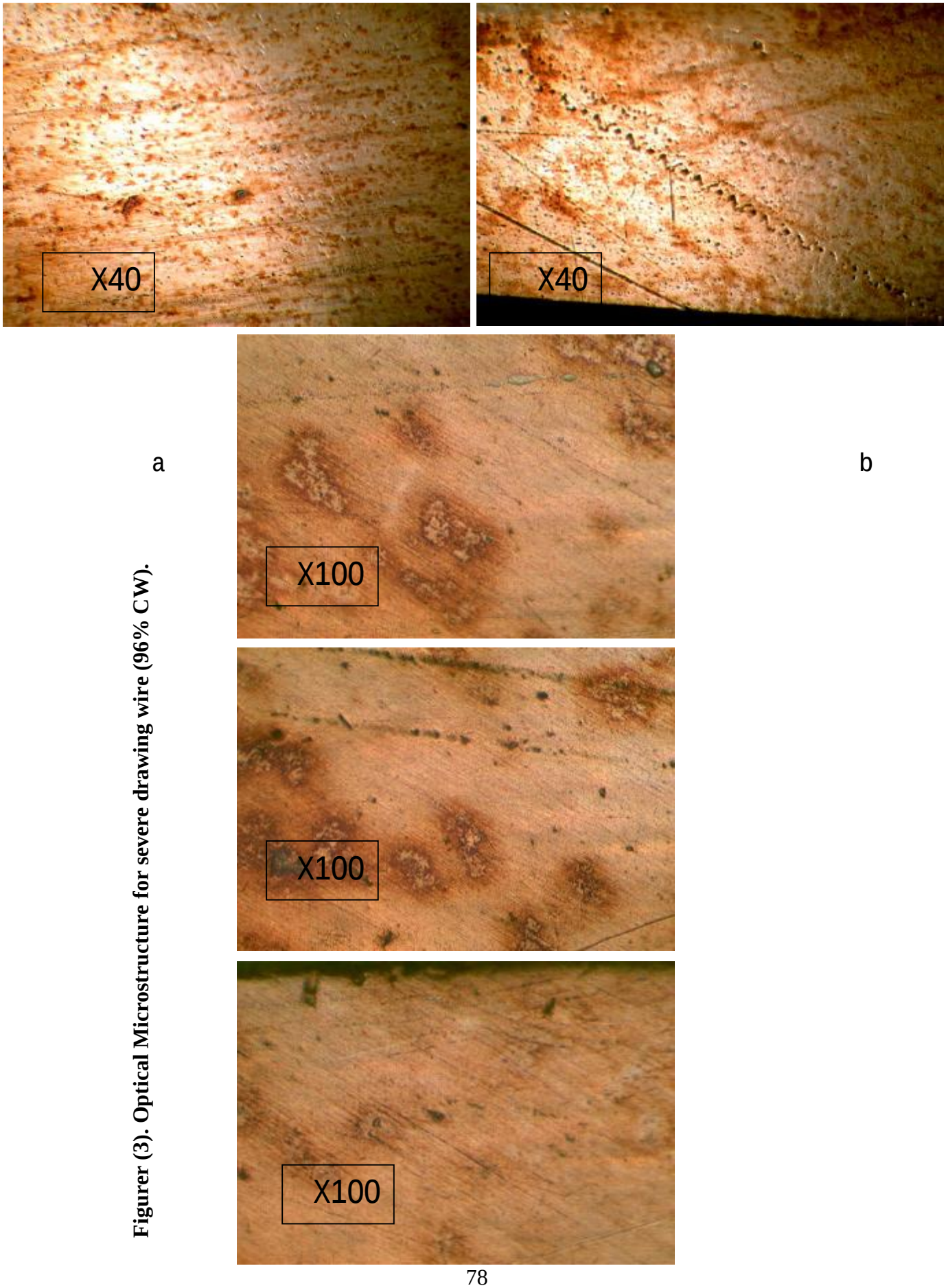

Figurer (3). Optical Microstructure for severe drawing wire (96% CW).

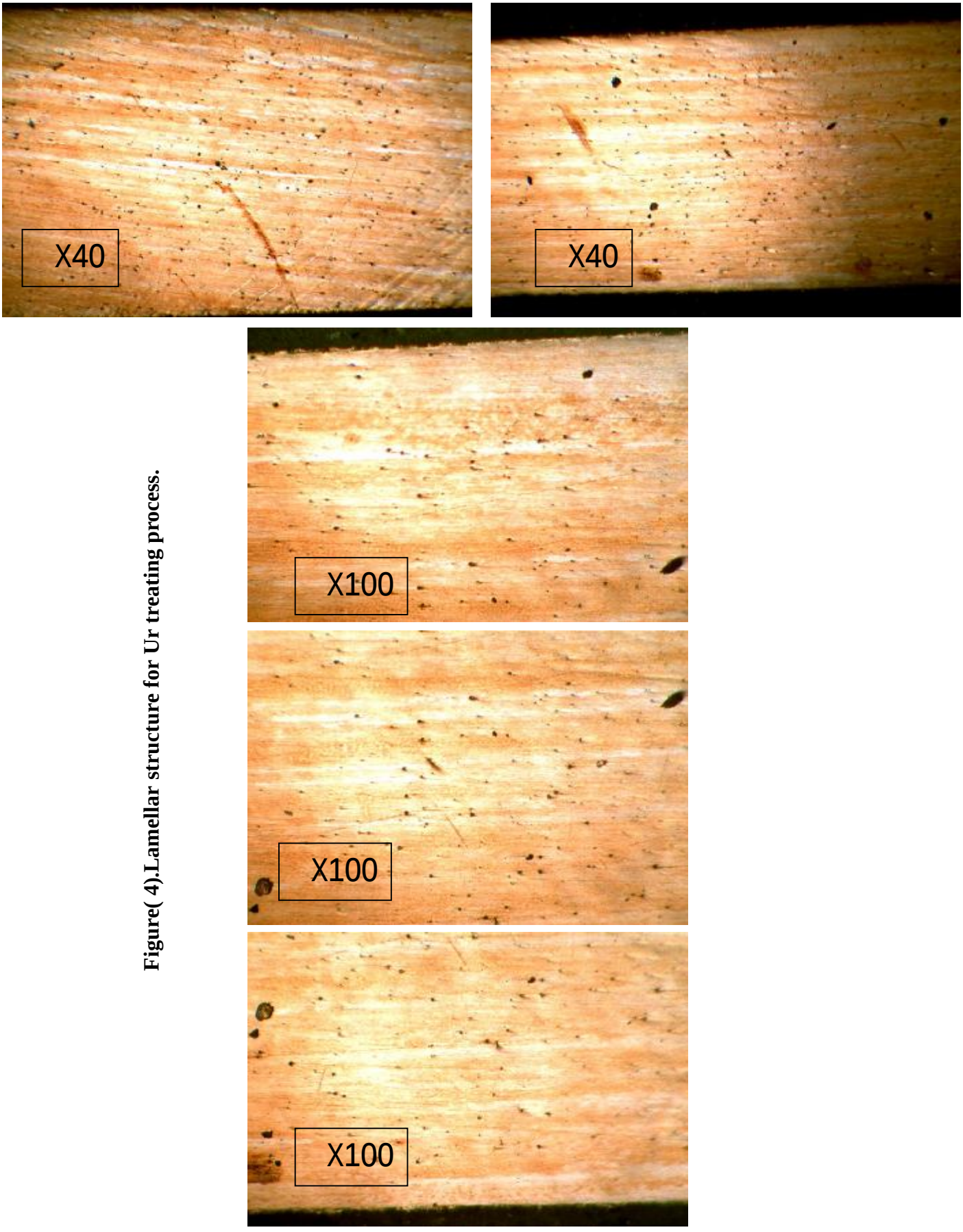

Figure(4).Lamellar structure for Ur treating process.

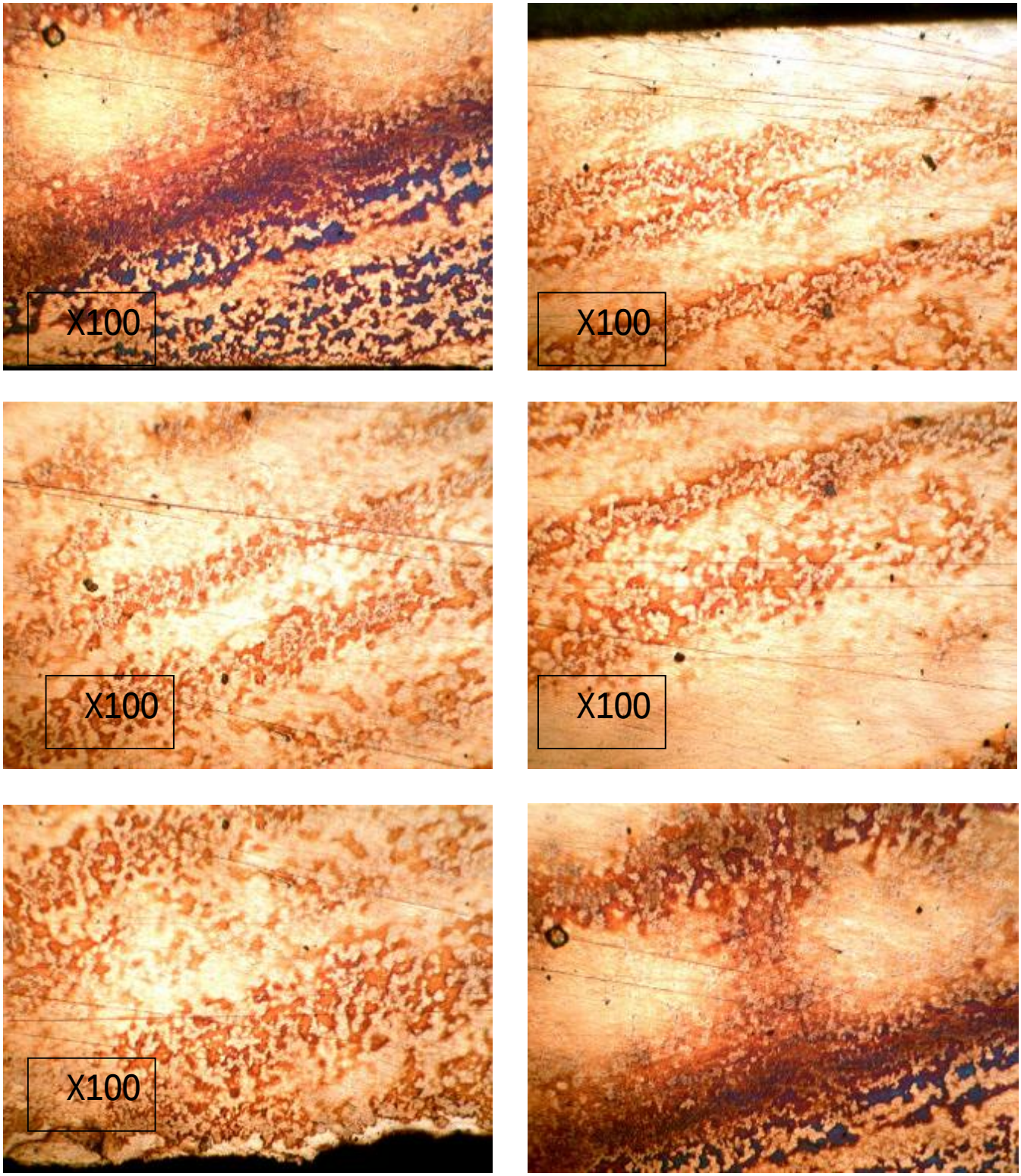

Figure (5). Lamellar recrystallized growth for the wire from the top surface to the down surface laboratory treated at 200 ^{o}C.

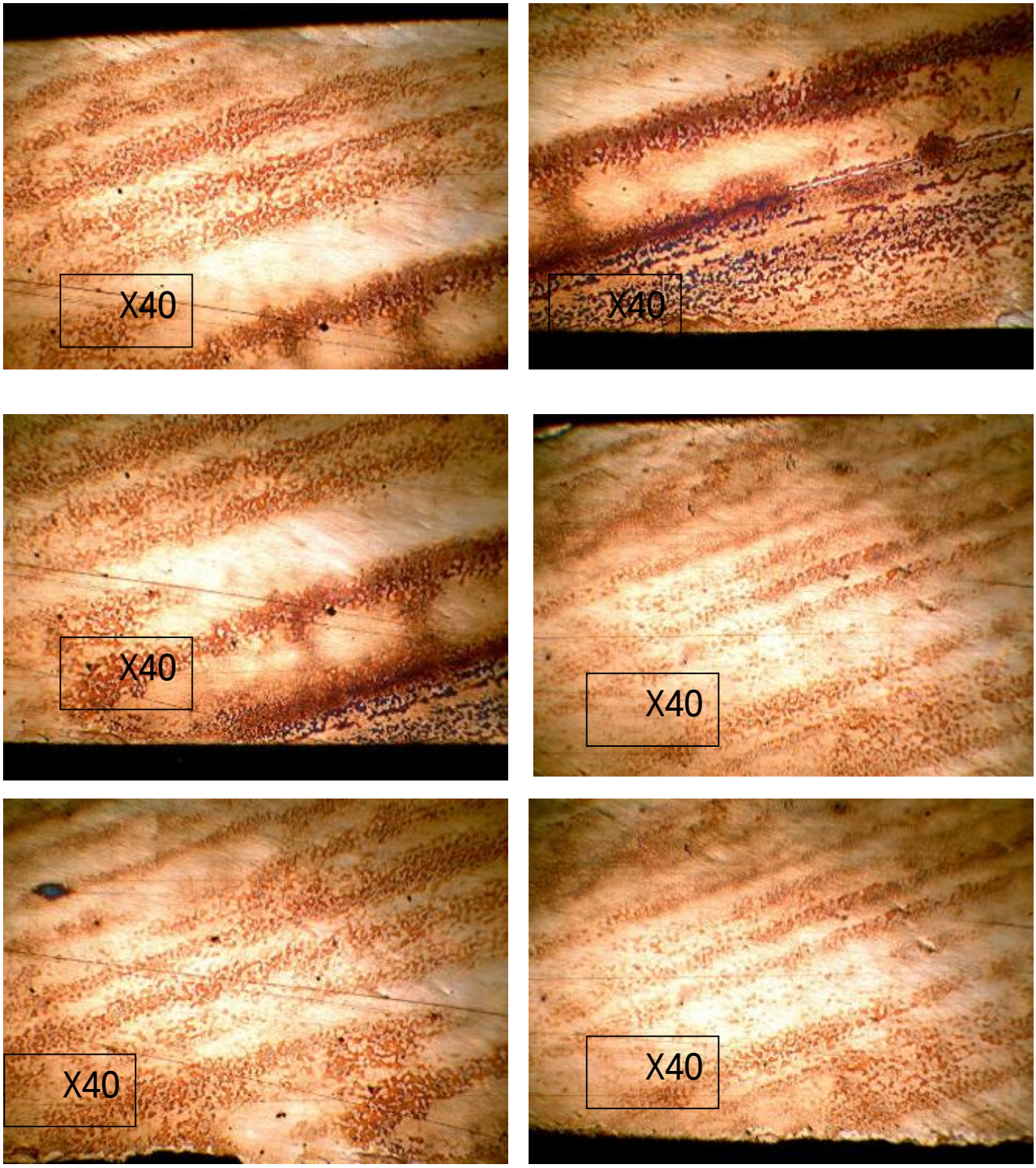

Figure (6). Another region for treated wire at 200^{o} C.

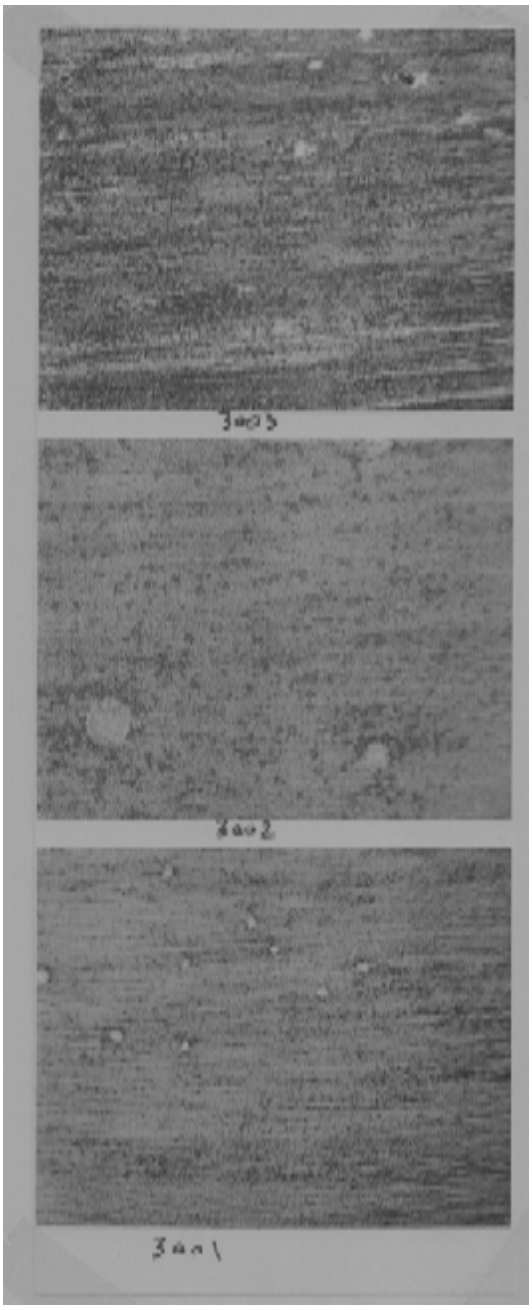

Figure (7). Lamellar growth in parallel lines, which shows the wire treated at 300 C°, X100 .

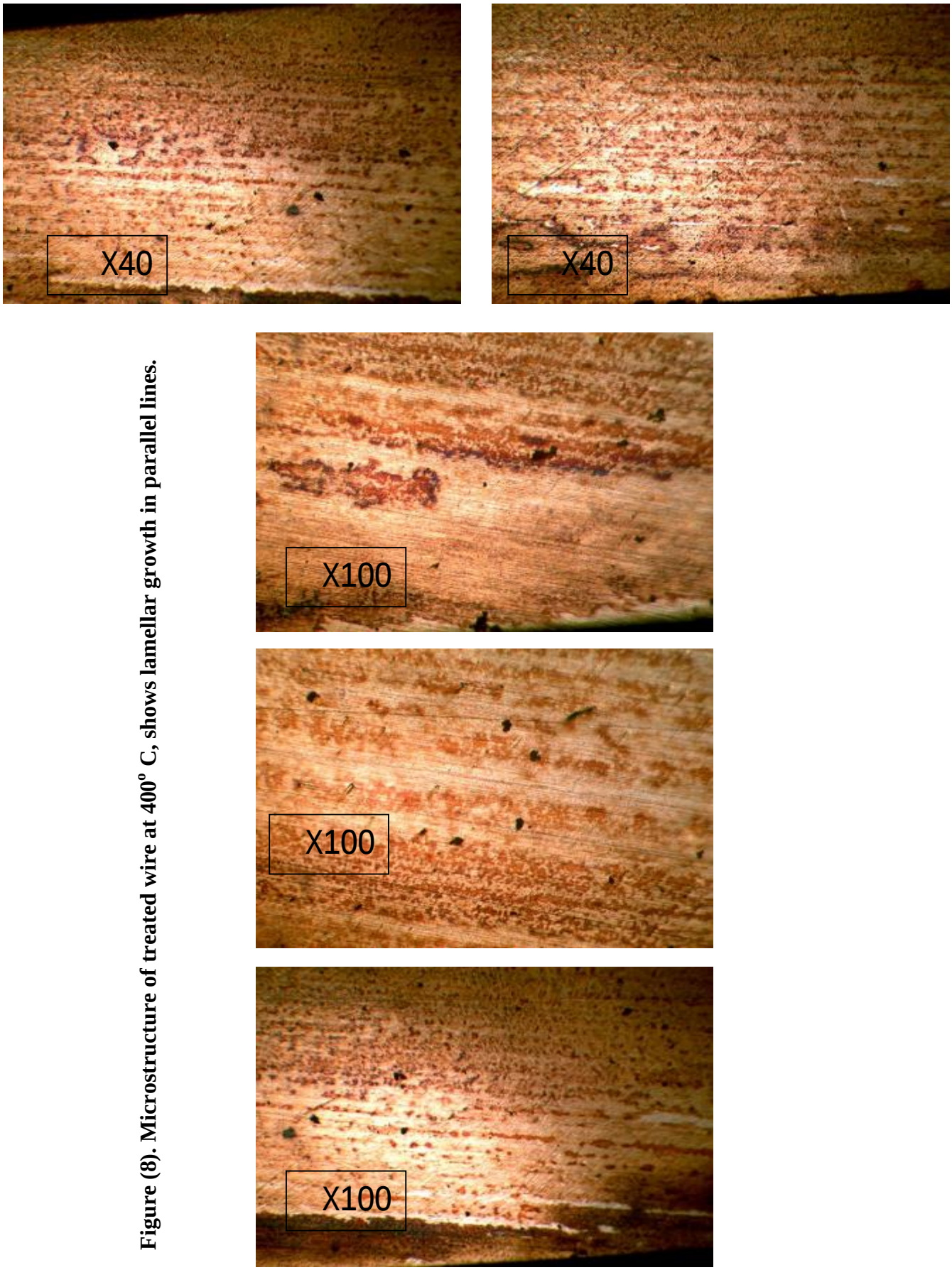

Figure (8). Microstructure of treated wire at 400° C, shows lamellar growth in parallel lines.

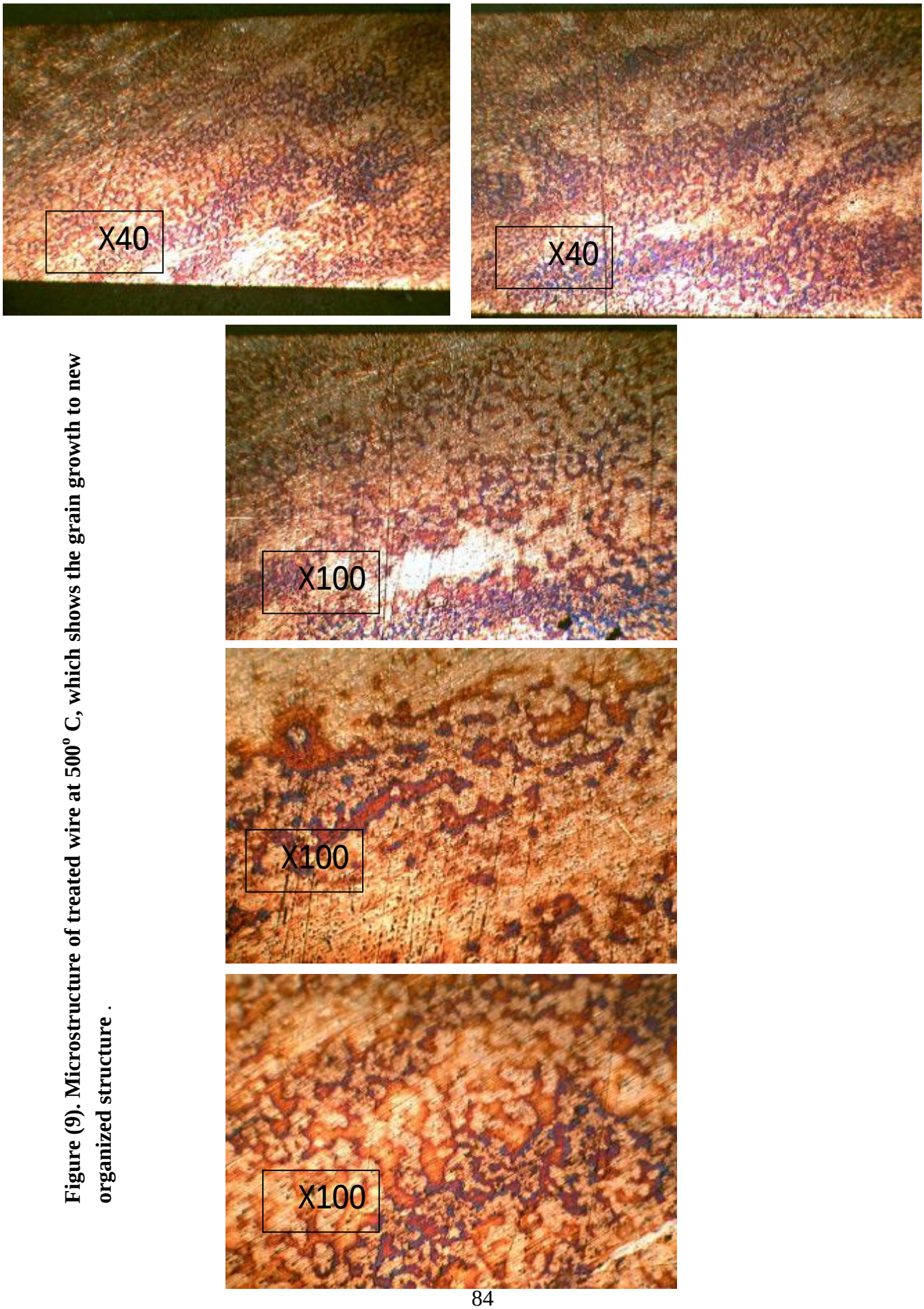

Figure (9). Microstructure of treated wire at 500° C, which shows the grain growth to new organized structure .

Porosity Control During Preparation of Bronze Filter Materials by Powder Metallurgy

Saleh K. Jabur
Engineering College
University of Basrah

Adnan S. Jabur
Engineering College
University of Basrah

Abstract

The ability to achieve close control of porosity and pore size is the main reason that filters are produced by powder metallurgy. This study was performed using bronze alloy powder (Cu-7.5%Sn- 0.1%Fe-0.3%Pb-0.15%Zn). The samples were prepared by two methods :(1) cold die compacting at different particle size, compacting pressure, sintering time, and sintering temperature, and (2) loose powder sintering. The compacts were sintered under controlled atmosphere. After surface preparation of the samples, the microstructure was used to compute the apparent porosity. It was found that the(Loose Powder Sintering) method is optimum method to produce highly porous materials with (~59%) porosity when selecting the proper conditions. The porosities obtained using cold die compaction are ranging between (5-41%) and sintered density ranging between (58.6-94.3%) of the theoretical mean density of the starting materials.

Keywords: Powder Metallurgy,Porous Materials and Porosity.

المستخلص

أن السبب الرئيس في استخدام المرشحات ألمصنعة من مساحيق المعادن هوقابلية الحصول على نسبة مسامية مسيطر عليها. الدراسة أنجزت باستخدام سبيكة برونز على شكل مسحوق. تم تحضير النماذج بطريقتين:(١) كبس على البارد عند ضغوط كبس مختلفة وحجم حبيبات المسحوق مختلفة (Cu-7.5%Sn- 0.1%Fe-0.3%Pb-0.15%Zn) كذالك زمن وحرارة التلبيد مختلفين, (٢) الطريقة الأخرى لتحضير العينات هي Loose Powder Sintering.المكبوسات لبدت في جو مسيطر عليه. بعد تحضير السطح, العينات عولجت لحساب المسامية الظاهرية. لقد وجد أن الطريقة الأفضل لإنتاج المواد ذات المسامية العالية حوالي (59%) هي (Loose Powder Sintering) عند استخدام الظروف الملائمة. المسامية التي تم الحصول عليها باستخدام كبس على البارد والتلبيد تتراوح بين(5-41%) والكثافة تتراوح بين (58.6- 94.3%) من الكثافة النظرية للمادة الخام.

1. Introduction

Powder metallurgy is the most common method to produce porous metallic products, where the level of porosity and the size distribution of pores are controlled. The three groups of porous materials produced commercially differ primarily in their porosity. These include [1];

1. Metallic materials in which the porous structure serve as reservoir for lubricant, such as self-lubricating bearings.
2. Metallic materials which has a controlled rate of permeation of fluids (liquid or gas) through the porous structure and which serve primarily as filters.
3. Metallic materials which contain a very high internal surface area and serve as porous electrodes for batteries and fuel cell.

A rigid, permeable structure can be created using P/M by forming a network of sintered powder particles and interconnected pore channels. Using similar manufacturing equipment and technology as structural P/M components, porous P/M materials are normally sintered to densities between 25% and 85% of theoretical mean density [2].By varying the compaction pressure, particles properties, sintering temperature and time, a range of porosity could be achieved [3]. Materials can be selected from wide varieties depending on the combination of application requirements and economics. The porosity is determined by the powder particle shape, the particle size, size distribution, surface texture, and other powder characteristics that depend on the material processing method. The four most common porous P/M materials are bronze, stainless steel, nickel, and nickel-base alloys [4].

The aim of this work was to study the effect of the following four parameters on the porosity of the sintered bronze filter compacts. These parameters are:compaction pressure, sintering temperature, sintering time and powder particle size.

Two methods were used to produce filter materials; loose powder sintering and cold die compaction.

2. Experimental procedures

The bronze powder was prepared by filing process, which gave a different particle sizes with an irregular particle shape as shown in the figure (1). The composition of the bronze powder was achieved by analysis the alloy using X-ray fluorescent spectrometer with specification of: high resolution peltier cooled Si-PIN detector, 40 KV tube voltage and Ag

target. Different particle sizes were obtained after sieving of the prepared powder for (15 min.) as shown in Figure (2). 0.7%wt of synthetic wax as a binder was mixed with the powder to promote powder compaction and ejection from the die and obtaining adequate green strength toreduce die wall friction [5]. The compaction die consisted of cylindrical bushing as cavity to fill with powder and two punches; upper and lower which were used to apply the load by manual operation press.

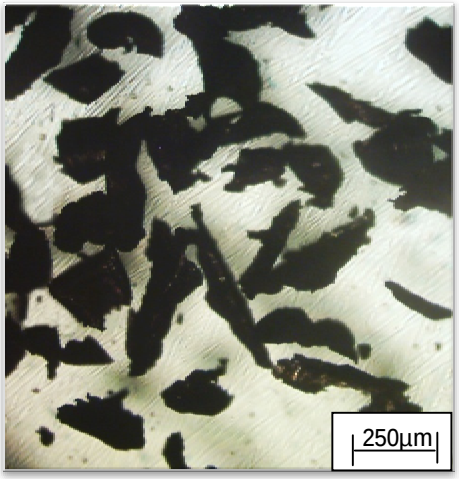

Figure (1) .Optical micrograph showing powder particle shape.

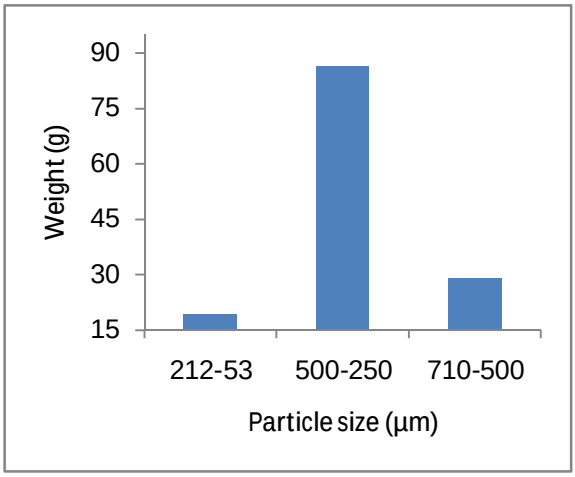

Figure (2). Bar chart of particle size distribution.

After compaction, the samples were sintered at specified temperatures (700, 800, 850, and 900)ºC under argon atmosphere. The sintering furnace is shown in Figure (3). The compacts were pre sintered at a temperature of (450 ºC) for (20 min) in order to remove the lubricant and to avoid sample blistering [6].

Figure (3). Vacuum tube furnace.

The following samples were used:

a) Compacting pressure effect:

Four samples with a particle size of (250-500 µm), were compacted under (200,300,400 and 500 MPa) pressures and sintered at 900 ºC for 30 min under controlled atmosphere (Argon gas).

b) Particle size effect:

Three samples with different particle size ranges (53-212,250-500 and 500-710 µm), were compacted under 300 MPa pressure and sintered at 900 ºC for 30 min under controlled atmosphere (Argon gas).

c) Sintering time effect:

Four samples with a particle size of (250-500 µm), were compacted under 300 MPa pressure and sintered at 900 ºC for (15, 30, 45, 60) min under controlled atmosphere (Argon gas).

d) Sintering temperature effect:

Four samples with a particle size of (250-500 µm) were compacted under300MPa pressure and sintered at (700, 800,850,900) ºC for 30 min under controlled atmosphere (Argon gas).

e) Particle size effect under Loose powder sintering:

Particle size ranges (53-212,250-500,500-710 µm) were studied. This process involved pouring of loose powder (non compacted) into small steel dishes, then this dishes was inserted into the sintering furnace. The sintering temperature was 900 ºC for 30 min under controlled atmosphere (Argon gas).

The following steps applied to testing the samples experimentallyaccording to ASTM C373 [7]:

i. Dry the test samples to constant mass by heating in an oven at 150°C (302°F), followed by cooling. Determine the dry mass, *D*, to the nearest 0.01 g.

ii. Place the samples in a pan of distilled water and boil for 5 h, taking care that the samples are covered with water at all times.

After the 5-hr boil, allow the samples to soak for an additional 24h.

iii. After impregnation of the test samples, determine to the nearest 0.01 g the mass, *S*, of each sample while suspended in water.

iv. After ejecting the samples from water, use cotton cloth to remove all excess water from the surface, and determine the saturated mass, *M*, to the nearest 0.01 g.

The following calculation can do[7]:

1. Calculate the exterior volume, V, in cubic centimeters, as follows:

$$V = M - S \quad (1)$$

2. Calculate the volumes of open pores V_{op} and impervious portions V_{Ip} in cubic centimeters as follows:

$$V_{op} = M - D \quad (2)$$

$$V_{\mathrm{IP}} = \mathrm{D} - \mathrm{S} \quad (3)$$

3. The apparent porosity, *P*, expresses, as a percent, the relationship of the volume of the open pores of the sample to its exterior volume. Calculate the apparent porosity as follows:

$$P = \left[\frac{M-D}{V}\right] * 100 \quad (4)$$

4. The bulk density, B, in grams per cubic centimeter, of a sample is the quotient of its dry mass divided by the exterior volume, including pores. Calculate the apparent density as follows:

$$B = \frac{D}{V} \quad (5)$$

3. Image processing

The samples were mounted and ground using emery paper of grades (320, 400, 1000, and 1200). The polishing process was carried out using aluminapowder suspensionof (0.5 µm) particle size [8]. The microstructure images were taken using an optical microscope and digital camera, and then they were treated by the (Photoshop CS2 and Image J) to estimate the apparent porosity computationally, which will be compared with the experimental data.

1. Image Treatment

a. Selection Stage

The aim of this stage is to select a suitable region. This step can be done in the following steps:

- The picture opens with "Photoshop CS2" program.
- Suitable area select from the picture using "Rectangular Marquee Tool M" from the tool list.
- New picture saves as a JPG type (figure 4b).

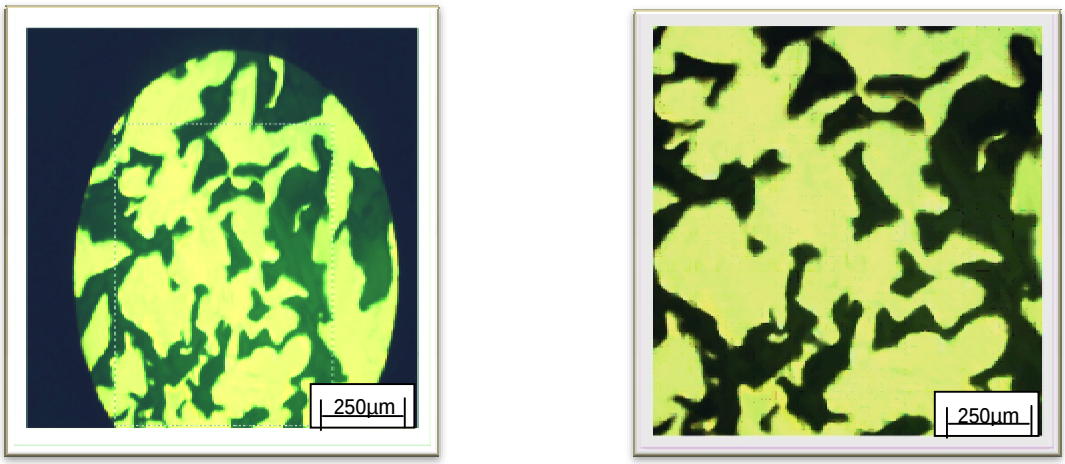

(a) (b)

Figure (4). Selection Stage.

b. Porosities Planning

- The new picture opens with Photoshop CS2 program, and improving its contrast and level by
- pressing on Adjustment then Auto Contrast from the image list.
- The porosities plan by "Brush Tool" (B) from the tool list.

New picture saves as JPG type (figure 5).

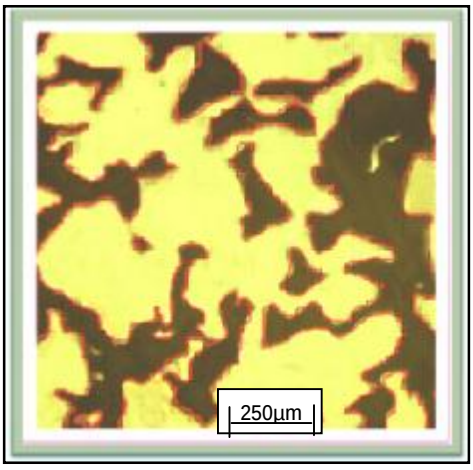

Figure (5). Porosities Planning.

c. Image Threshold

- The new picture opens with Photoshop CS2 program.
- The images changes to black and white colors by pressing on Adjustment then threshold command from the image list with a suitable level depending on the image nature, the final requirement, and the operator experience.
- Pressing on Noise then Dust &Scratches from the filter list and choosing a suitable radius value for the image. Figure (6) shows the all steps of this stage.

(a) (b)

Figure (6). Threshold stage, (a) Threshold step, (b) Dust and scratches step.

2. The Apparent Porosities Estimation

Using the Image J program, the estimation of the apparent porosities of sintered compacts can be done by these following steps:

- Opening final picture with Image J program and processing this picture as follows:
- Process → Binary → Threshold.
- Image → Adjust → Threshold → Black &White.
- Analysis → Analysis of particles.

The program measures and scans all the picture and gives results box, this involves:

i. Count of particles (pores)
ii. Total area of particles (pores)
iii. Average size of particles (pores)
iv. Area fraction (which represents the apparent porosity of sample).

(a) (b)

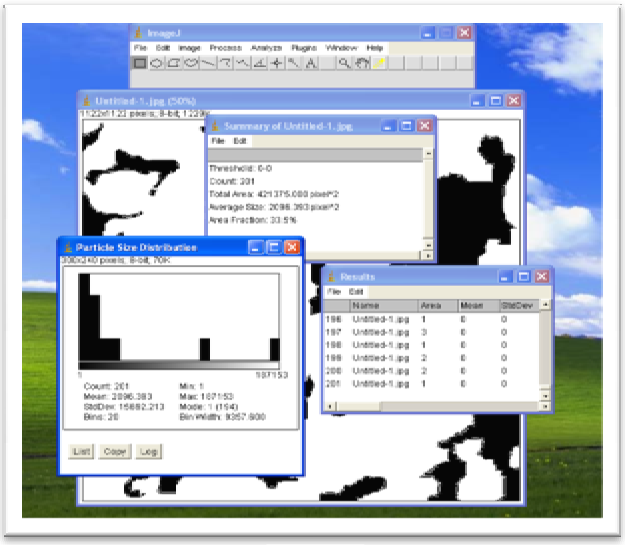

(c)

Figure (7). Estimation process of porosity,(a) Threshold,(b)black&White, (c)Analysis particles.

The shrinkage percentage can be determined from the following equation [8]:

$$\text{Shrinkage (or growth)}\ \% = \frac{Change\ in\ Length}{Sintered\ Length} \times 100 \qquad (6)$$

4. Results and discussion

4.1 The Effect of Compacting Pressure

Figure (8) shows the variation of the green density of compacts with compacting pressure. It is clear that the green density increased with increasing compacting pressure, which is due to decreasing the spacing between particles by particles movement and plastic deformation. The highest green density of ($7.15\,g/cm^3$) was obtained at a compaction pressure of 500 MPa.Apparent porosity which is the amount of pores in the volume of sintered compact is shown in Figure (9) as a function of compacting pressure.It is clear that the apparent porosity decreased with increasing the compacting pressure due tothe reduction in the number and size of pores. Figure (12) shows this variation.

In Figure (10), the water adsorption of the sintered compacts decreased with increasing the compacting pressure. The large drop of water adsorption appeared as linear function with compacting pressure until 400MPa. However, the volume fraction of pores reaching steady state. Figure (11) shows the variation of the bulk density of sintered compacts with compacting pressure. It increased with increasing compacting pressure due to increasing contact regions which enhance necking and diffusion between particles during sintering.

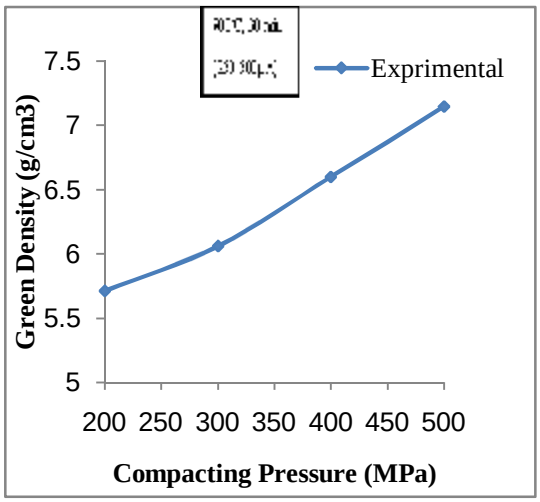

Figure (8). Green density as a function of compacting pressure .

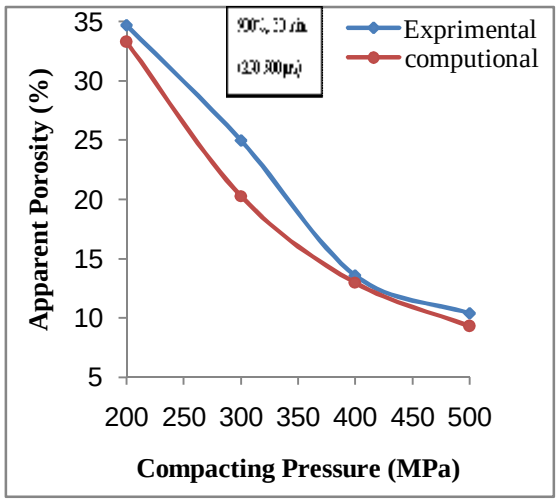

Figure (9). Apparent porosity as a function of compacting pressure .

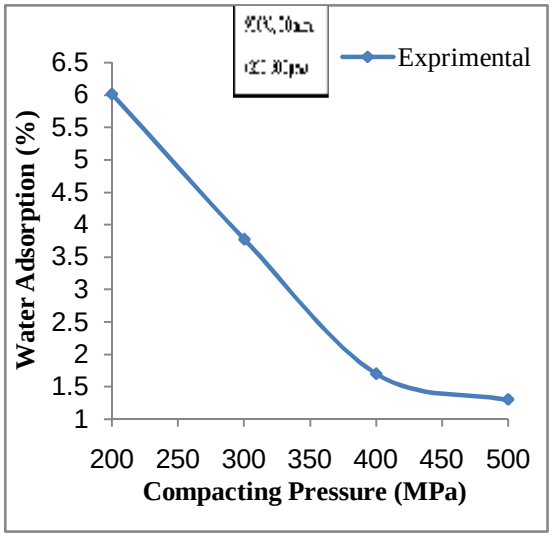

Figure (10). Water adsorption as a functionof compacting pressure.

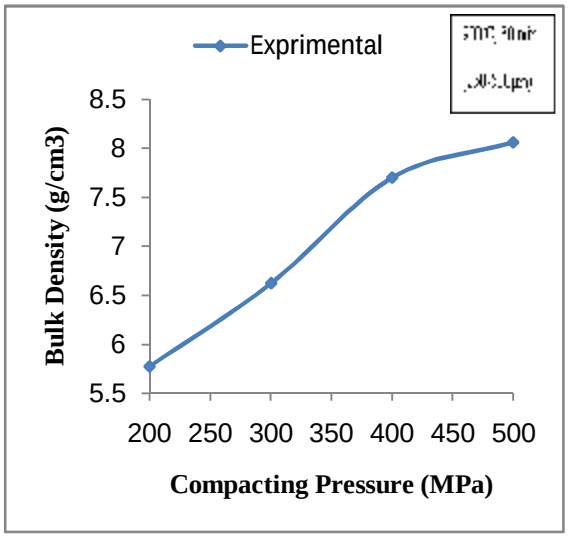

Figure (11). Bulk density as a function of compacting pressure.

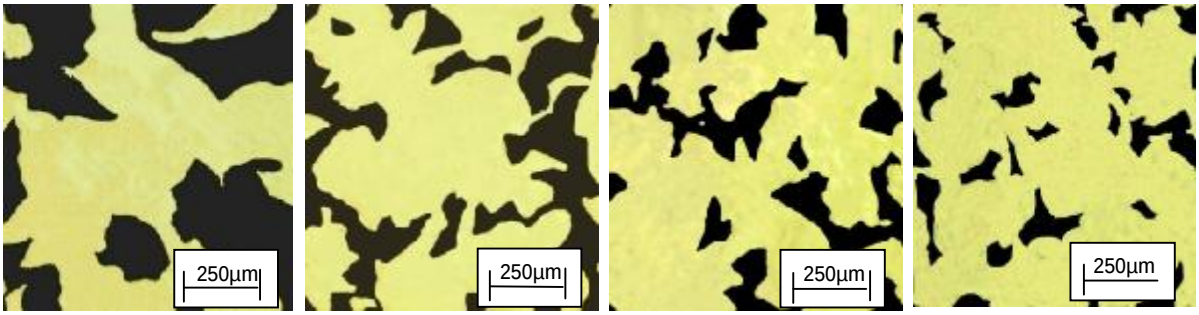

(a) (b) (c) (d)

Figure (12). The microstructural images of sintered samples with different compacting pressures; (a) 200 MPa (b) 300 MPa (c) 400 MPa (d) 500 MPa.

4.2 The Effect of Sintering Time

From Figure (13), it was found that the apparent porosity of compacts decreased linearly with the sintering time. The increasing of sintering time process at high temperature (900 ºC) causes particles growth which relatively leads to close the voids between particles. Figure (17) shows this variation. Water adsorption behavior resembles the porosity behavior with sintering time as shown in Figure (14).

Variation of bulk density with sintering time at 900 ºC of sintering temperature is shown in Figure (15). It is clear that bulk density of sintered compacts increased with sintering time up to (45 min.) reaching a steady state. Figure (16) presents the influence of the sintering time on the shrinkage of sintered samples. It is clear that, the shrinkage percent increased with increasing the sintering time.

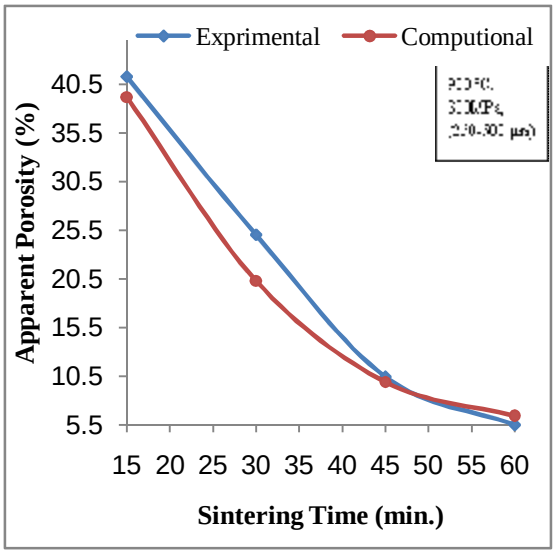

Figure (13). Effect of sintering time on apparent porosity.

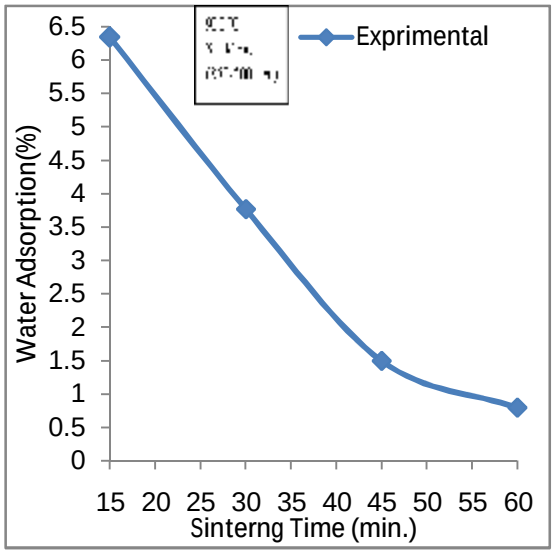

Figure (14). Relationship between water adsorption and sintering time.

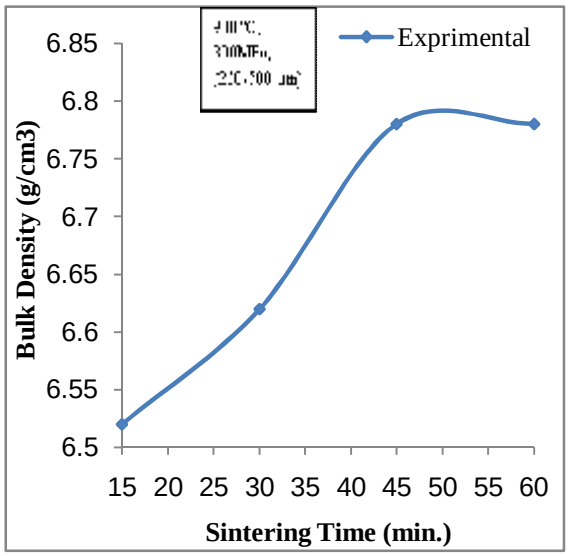

Figure (15). Effect of sintering time on bulk density of prepared alloy.

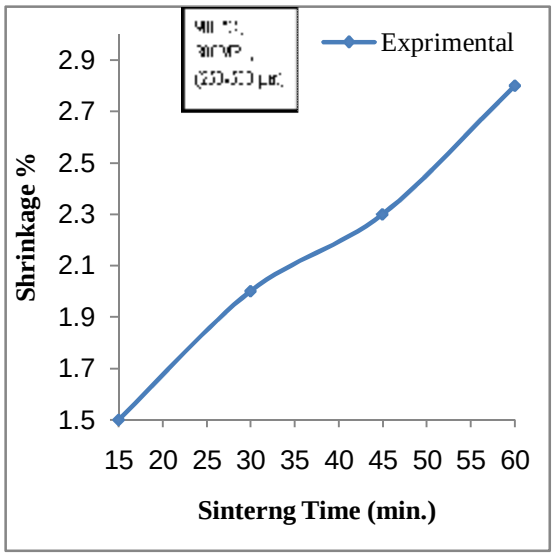

Figure (16). Shrinkage of bronze powder compacts as a function of sintering time.

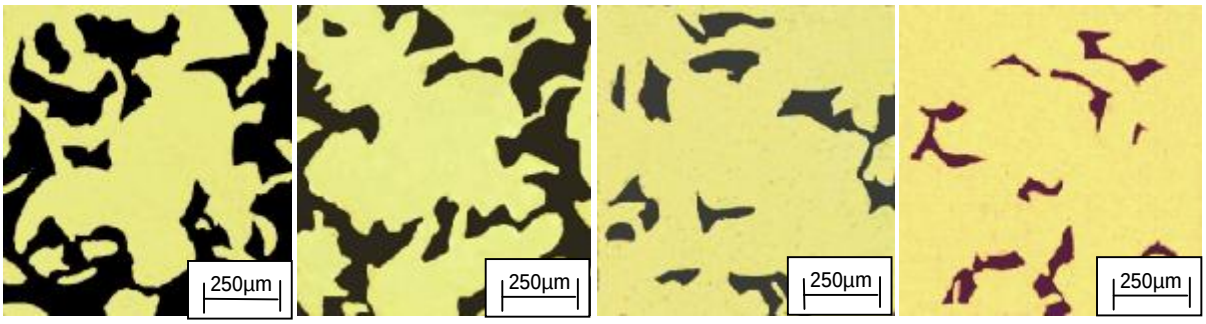

(a) (b) (c) (d)

Figure (17). The microstructure images of samples sintered for, (a) 15min. (b) 30min. (c) 45min. (d) 60 min.

4.3 The Effect of Sintering Temperature

Figure (18) shows the effect of sintering temperature on the apparent porosity of sintered samples. It can be seen that the porosity of the sintered compacts decreased with increasing the sintering temperature because of growth and swelling of particles which leads to close the voids between them. Figure (22) shows this variation.

Also, the water adsorption as a function of the sintering temperature is shown in the Figure (19). It decreased with increasing the sintering temperature.Bulk density as a function of sintering temperature is shown in Figure (20). It increased with low rate up to (850 ºC), so it showed a rapid increasing which may be due to the reduction of pore size and number. Figure (21) shows the influence of sintering temperature on the shrinkage percentage of sintered compacts. It shows that the shrinkage percentage increased with increasing sintering temperature.

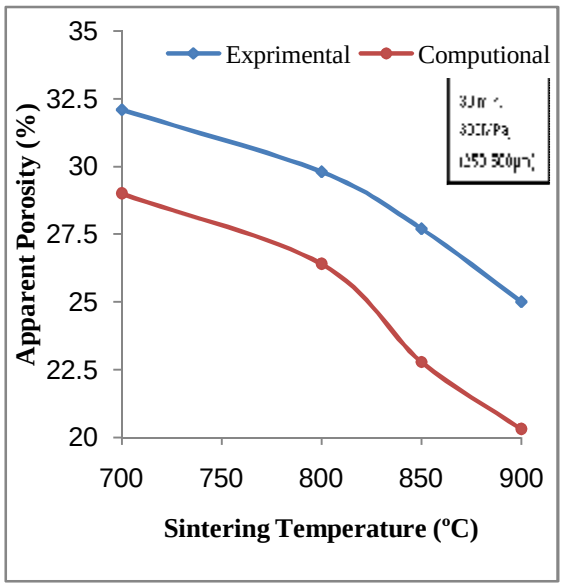

Figure (18). Effect of sintering temperature on apparent porosity.

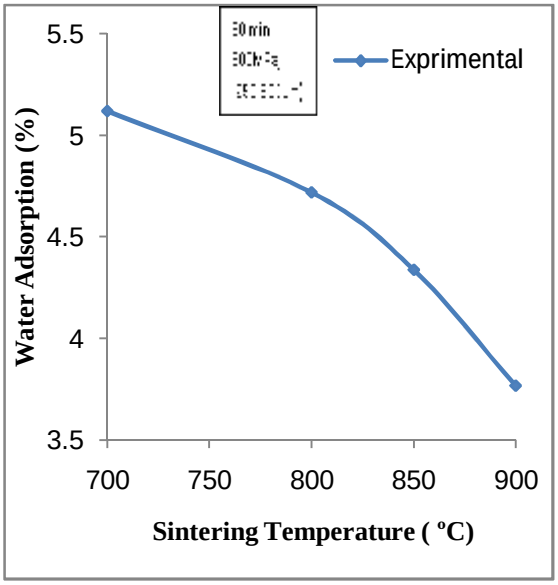

Figure (19). Water adsorption as a function of sintering temperature.

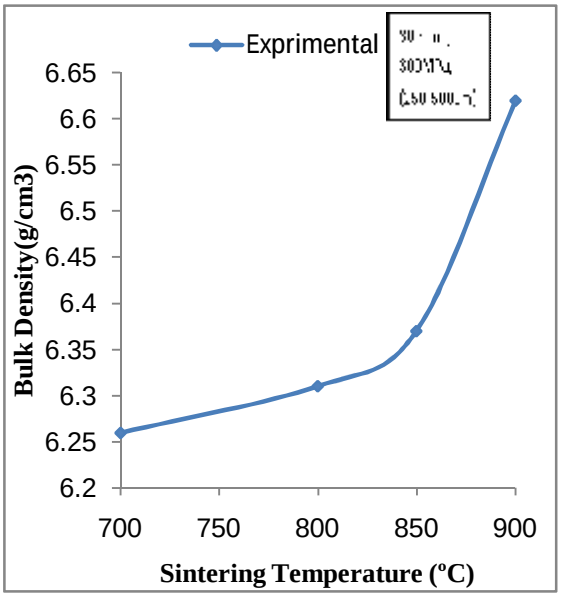

Figure (20). Effect of sintering temperature on the bulk density of prepared alloy.

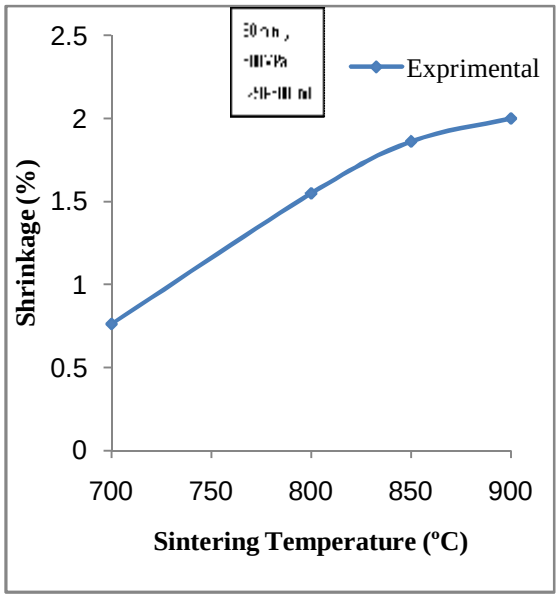

Figure (21). Shrinkage of bronze powder compacts as a function of sintering temperature.

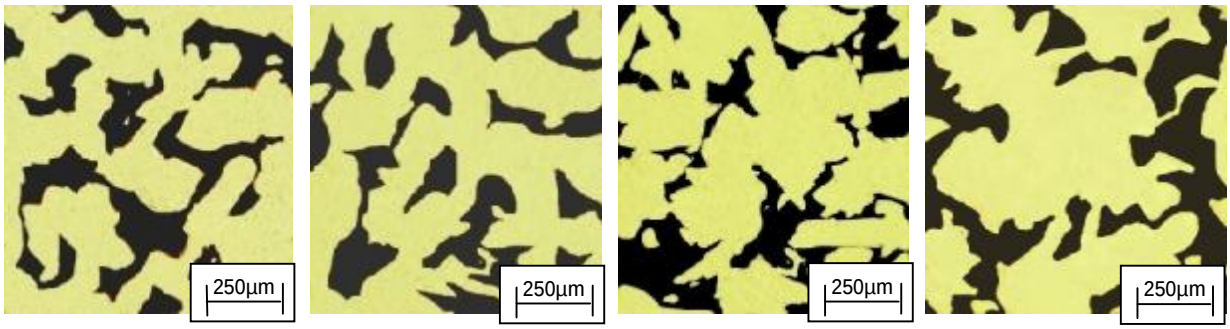

(a) (b) (c) (d)

Figure (22) .The microstructure images of samples sintered at, (a)700 ºC (b) 800 ºC (c) 850 ºC (d) 900 ºC, for (30 min).

4.4 The Effect of Powder Particle Size

As shown in the Figure (23) the apparent porosity of sintered samplesincreased with increasing the particle size of the powder. This is due to the number of contacts in the fine particles is larger than coarse particles which causes the increasing of sintering rate, reducing of apparent porosity and increasing of bulk density (Figure 25).

Figure (26), also shows these changes. The relationship between the water adsorption and powder particle size is shown in the Figure (24). From this figure, it is clear that the water adsorption increased with increasing the powder particle size.

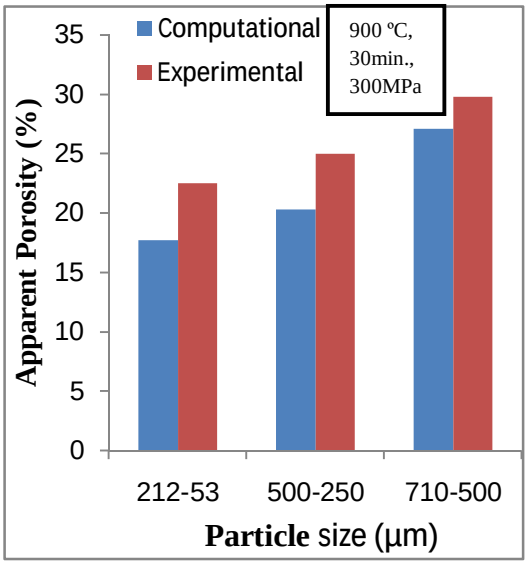

Figure (23). Effect of powder particle size on the apparent porosity.

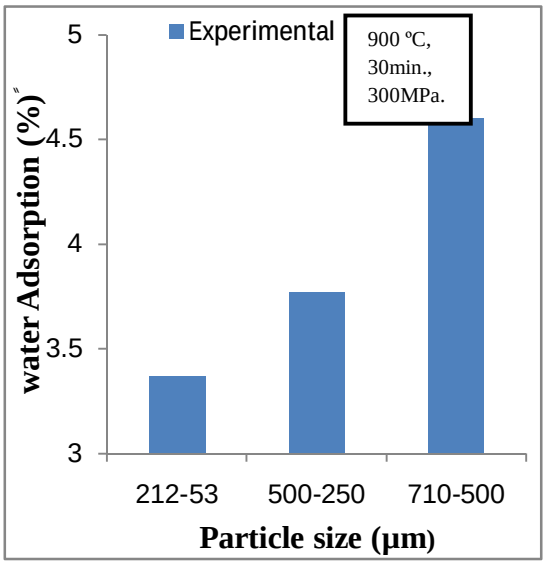

Figure (24).Water adsorption as a function of the powder particle size.

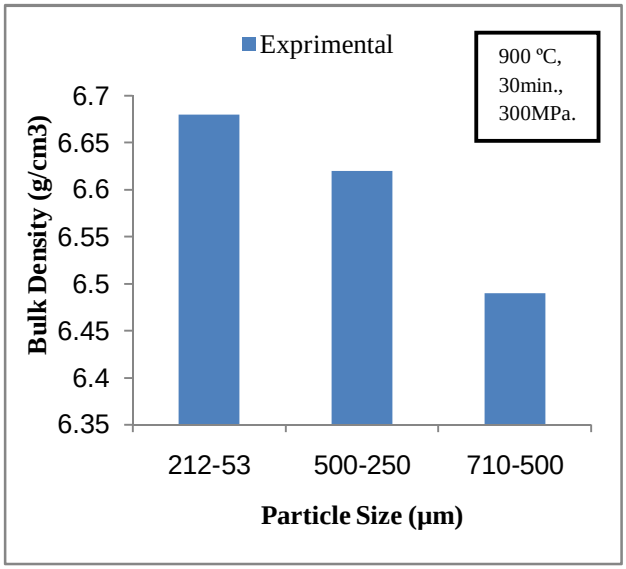

Figure (25). Effect of powder particle size on the bulk density of prepared alloy.

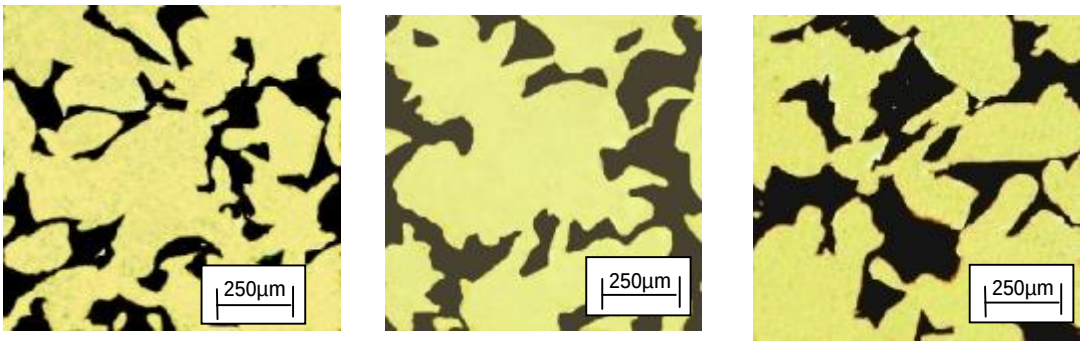

(a) (b) (c)

Figure (26) .The microstructure images of samples prepared at different particle sizes (a) (53-212 µm) (b) (250-500 µm) (C) (500-710 µm).

4.5 The Effect of Loose Powder Sintering

Here, the effect of particle size on the apparent porosity, water adsorption and bulk density of loose sintered samples (Figures 27, 28, 29 and 30) are similar to that in Figures (23, 24, 25 and 26). These behaviors can also be explained by the same way. But when comparing between loose sintered and compacted sintered samples behaviors, the formers developed higher apparent porosity and water adsorption and lower bulk density.

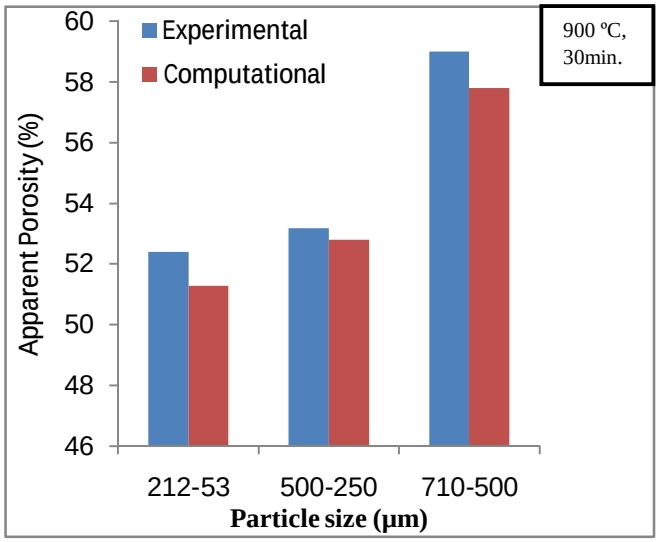

Figure (27). Effect of powder particle size on the apparent porosity.

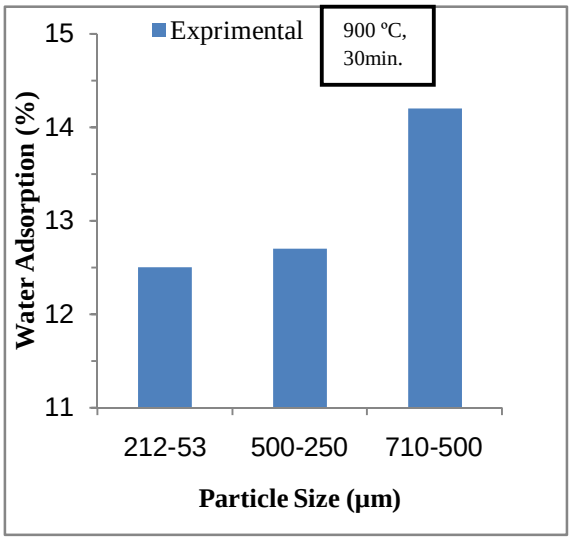

Figure (28). Water adsorption as a function of powder particle size.

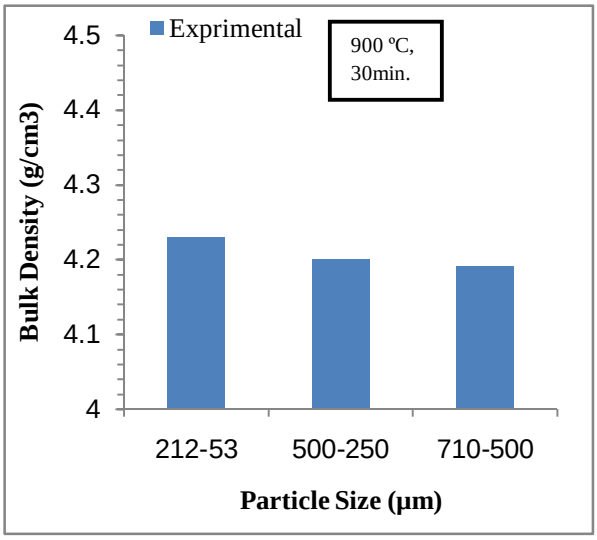

Figure (29). Effect of powder particle size on the bulk density of prepared alloy.

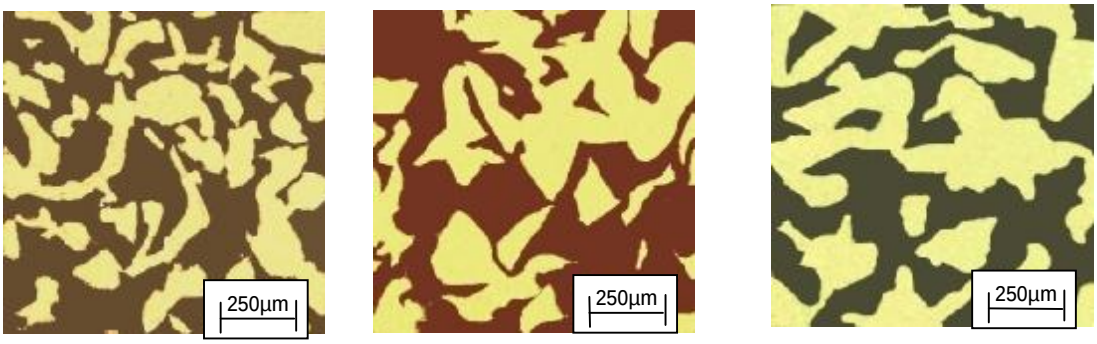

(a) (b) (c)

Figure (30). The microstructure images of samples prepared by loose powder sintering (a) 53-212 µm (b) 250-500 µm (c) 500-710 µm.

5. Conclusions

1. Loose Powder Sintering method is an optimum method to produce highly porous materials with porosity percent of about (59%) with proper conditions.
2. The higher sintering time was undesired because it reduced the porosity value to about (5.5%).
3. Using powder particles with a flake, acicular and irregular shape was proper to prepare the bronze filter materials with porosities ranging between (5-59%).

6. References

[1] M.Can and A.B.Etemoglu,"Porosity Measurement of Stainless Steel Filters Produced by Electric Discharge Technique", Powder Metallurgy International, Vol.17, PP340-349, No.5, 2004.

[2] M.Eisenmann, "Porous P⁄M Technology",ASMHandBook, Vol.17,2000.

[3] D. Poquillon, J. Lemaitre, V. Baco-Carles, Ph. Tailhades, J. Lacaze,"Cold compaction of iron powders—relations between powder morphology and mechanical properties Part I: Powder preparation and compaction", Powder Technology, Vol.126, PP65-74, 2002.

[4] L.Albano-MÜLLER,"Filters Elements of Highly Porous Sintered Metals", Powder Metallurgy International, Vol.14, No.2, 1982.

[5] I.Vida-Simiti, N.Jumate and T.Bolog, "Experimental Research of Sintered Porous Materials of Bronze Powders ", Journal of Optoelectronics and Advanced materials, Vol.8, No.2, PP716-719, April 2005.

[6] D. Garg, K. Berger, D. Bowe, and J. Marsden," Effect of Atmosphere Composition on Sintering of Bronze:, Gas Interactions in Non Ferrous Metal Processing, Minerals, Metals and Materials Society, PP17-26, 1996.

[7] ASTM C373, "Standard Test Method for Water Absorption, Bulk Density, Apparent Porosity, and Apparent Specific Gravity of Fired Whiteware Products", 1999.

[8] "Powder Metal Technologies and Applications", Vol.7,ASM HandBook,ASM International, 1998.

7. Nomenclature

A list of symbols are given with a brief description and unit used

Latin Symbols

Symbols	Definition	Unit
B	Bulk Density	g/cm^3
D	Dry Mass of the Samples	g
M	Saturated Mass of samples	g
m	Green Mass of Compacts	g
P	Apparent Porosity	—
P/M	Powder Metallurgy	—
S	Mass of Samples While Suspended in Water	g
V	Volume of the Compacts	cm^3

Greek Symbols

Symbols	Definition	Unit
ρ	Density	g/cm^3

Subscripts

Symbols	Definition
g	Green
op	Open Pores
Ip	Impervious portions

Effect of Operating Conditions on Co_2 Absorption into Aqueous Alkanol amine Solutions in Packed Column

Saleh E. Najim
Engineering College
University of Basrah

Adnan A. Ateik
Basrah Technical College

C. K. Haweel
Engineering College
University of Baghdad

Abstract

This paper highlights the importance of operating parameters to mass-transfer in CO_2 absorption in columns with different packings. The study compares the performance of two packings, Gempak 4A and Raschig ring. Mass-transfer efficiency of these packings was determined by carrying out absorption experiments in a pilot-scale absorption unit with aqueous solutions of monoethanolamine (MEA), Diethanolamine (DEA),2-amino-2-methyl-1-propanol (AMP) and methyldiethanolamine (MDEA) as test solvent.

The overall mass-transfer coefficient ($K_G a_v$) can be considered to be indicative of the CO_2 removal efficiency of the system and can be calculated from experimentally gas-phase CO_2 concentration profiles within the test columns. The results of this study indicate that mass-transfer coefficient of these packings tested varies significantly not only with operating parameters such as liquid load, liquid CO_2 loading, solvent concentration, solvent type and feed CO_2 concentration but also with packing arrangement.

In absorption experiments the results show the typical behavior of liquid controlling system. Gas flow rate has no influence on overall mass transfer coefficient (KGav), and an increase in liquid flow rate yields a greater (KGav). CO2 loading lowers the (KGav) and an increase in amine concentration induces a higher (KGav). Increasing the CO2 concentration within the feed gas was found to reduce the value of (KGav) within the system.

Structured packing offers superior performance to random packings, structured packing provides almost twice greater (KGav) than random packings.

Keywords: operating conditions; carbon dioxide; Amine solution, packed column.

تأثير الظروف التشغيلية على عملية امتصاص غاز ثاني أوكسيد الكربون باستخدام المحاليل الأمينية خلال الأبراج المحشوة

المستخلص

يسلط هذا البحث الضوء على الاحداثيات المهمة في عمليات انتقال المادة عن طريق امتصاص غاز ثاني اوكسيد الكربون في الابراج المحشوة كما يهدف البحث الى المقارنة بين الحشوات المنتظمة والحشوات العشوائية للأبراج. تم بحث كفاءة انتقال المادة بأجراء تجارب عملية في وحدة امتصاص ريادية باستعمال محاليل أمينية مختلفة ولكلا النوعين من الحشوات.

أن معامل انتقال المادة الاجمالي يمكن ان يعد دليل على كفاءة ازالة غاز ثاني اوكسيد الكربون الذي يحسب من خلال التجارب العملية باتباع تدرج التركيز لغاز ثاني اوكسيد الكربون في جزء البرج المعد لذلك. دلت النتائج على ان معامل انتقال المادة يتغاير ليس فقط مع احداثيات التشغيل (تركيز المذيب ونوعه، تركيز غاز ثاني أوكسيد الكربون في السائل والغاز الداخل ومعدل جريان السائل) ولكن أيضاً مع ترتيب الحشوات. تبين أن طور السائل هو المسيطر على عملية الامتصاص وأن معدل جريان الغاز ليس لهتأثير على معامل انتقال المادة الاجمالي بينما ينتج زيادة معدل جريتان السائل وتركيزه زيادة في معامل انتقال المادة الاجمالي وان زيادة تركيز غاز ثاني اوكسيد الكربون في الغاز الداخل يؤدي الى تقليل معامل انتقال المادة الاجمالي. أن الحشوات المرتبة بانتظام تعطي اداء افضل بالمقارنة مع الحشوات العشوائية حيث وجد ان هذا الترتيب للحشوات يعطي تقريبا" ضعف قيمة معامل انتقال المادة الاجمالي بالمقارنة مع الحشوات العشوائية.

1. Introduction

The removal of carbon dioxide from gas streams, commonly referred to as acid gas treating, is necessary in many industrial processes. In natural gas processing, CO_2 is removed to reduce the costs compression and transportation. In ammonia manufacture, CO_2 needs to be removed from the hydrogen streams, since it poisons the catalyst for the reaction between hydrogen and nitrogen. Power plant flue gases are a new application of CO_2 removal processes, compared to the first two. In this case, CO_2 is removed only to reduce greenhouse emissions. This issue is of increasing interest, because global warming is an important environmental and political issue. With the Kyoto protocol of 1997 forty-one industrialized countries agreed to cut the carbon dioxide emissions to approximately 5% less than the emissions in 1990, in a five year period going from 2008 to 2012[1].To achieve the agreement target, separation of CO_2 from industrial waste gases, which would otherwise be vented to atmosphere, becomes essential. A wide range of technologies currently exist for separation and capture CO_2 from gas streams. There are a number of methods available for effectively

capturing CO_2 and depending on the nature of the problem one process will be favored over another. Some of the more common separation methods includes absorption, low temperature distillation, adsorption, and membrance[2]. The most common method used to remove carbon dioxide is absorption into a liquid solvent, particularly aqueous alkanolamine solutions. The alkanolamine treating process was first introduced in 1930 when R. R. Bottoms patented the process[3]. Since that time, the process has remained virtually unchanged.The objective of this study is to obtain the mass transfer performance of the CO_2 absorption process using different packing type and different aqueous alkanolamine solutions as the column internal and absorption solvent, respectively. The performance of the process is presented in terms of the volumetric overall mass transfer coefficient. The effect of various operating parameters, such as the liquid flow rate, gas flow rate, CO_2 feed percent, and liquid CO_2 loading were also evaluated.

2. Theory

The height of the absorption column required to reduced the concentration of a particular component in the gas stream to a certain level can be calculated by combining the degree of mass transfer and the differential material balance. Considering a segment of the column with height *dZ* as shown in Figure (1), the material balance of the transferred component A can be written as:

$$N_A A_e = G_i A_c dY_{A,G} \tag{1}$$

$$N_A A_e = G_i \frac{V_c}{dZ} d\left[\frac{y_{A,G}}{1-y_{A,G}}\right] \tag{2}$$

Generally, the gas - liquid interfacial area for mass transfer is presented in terms of the area per unit volume of the absorption column. Therefore, Equation (2) can be expressed by:

$$N_A a_V dZ = G_i d\left[\frac{y_{A,G}}{1-y_{A,G}}\right] \tag{3}$$

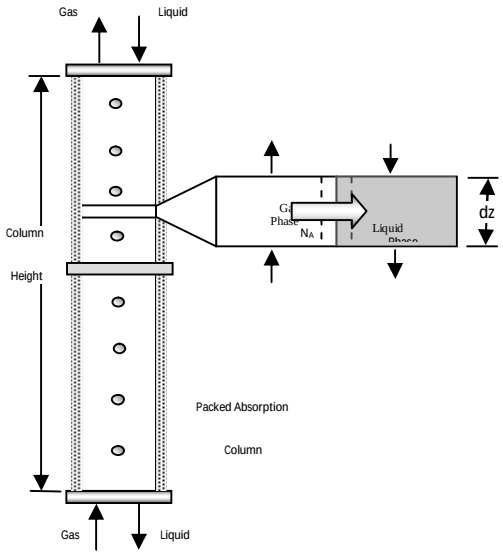

Figure (1) Schematic diagram of a packed column.

According to the aforementioned mass flux equation, the material balance equation can be further arranged as:

$$K_G\left(Py_{A,G} - HC_{A,L}\right)a_V\,dZ = G_i d\left[\frac{y_{A,G}}{1-y_{A,G}}\right] \tag{4}$$

Based on equation (4), the required height (Z) can be integrating over the column:

$$Z = G_i \int_{Bottom}^{Top} \frac{1}{K_G a_V}\frac{dy_{A,G}}{\left(1-y_{A,G}\right)^2\left(Py_{A,G} - HC_{A,L}\right)} \tag{5}$$

In many cases it is assumed that the mass transfer coefficient is independent of the concentration of the absorbed component in the system[4], in other words the volumetric $K_G a_V$ coefficient is constant over the height of the column. Thus this term can be removed from the integral and equation (5) may be simplified as:

$$Z = \left(\frac{G_i}{K_G a_V P}\right)\int_{Bottom}^{Top} \frac{dy_{A,G}}{\left(1-y_{A,G}\right)^2\left(y_{A,G} - HC_{A,L}/P\right)} \tag{6}$$

The term ($G_i/K_G a_V P$) has the dimension of length and is designated the height of packing required for transfer unit, commonly known as the height of a transfer unit (*HTU*).

The integral on the right hand side of equation (6) is dimensionless and represents the total number of these transfer units required to make up the whole column. Consequently, it is called the number of transfer units (*NTU*). Equation (6) may therefore be written as:

$$Z = (HTU)\,(NTU) \tag{7}$$

Where

$$HTU = \left(\frac{G_i}{K_G a_V P} \right) \tag{8}$$

and

$$NTU = \int_{Bottom}^{Top} \frac{dy_{A,G}}{(1-y_{A,G})^2 \left(y_{A,G} - HC_{A,L}/P\right)} \tag{9}$$

By differentiating Equation (6) we get:

$$dZ = \left(\frac{G_i}{K_G a_V P} \right) \left(\frac{dy_{A,G}}{(1-y_{A,G})^2 \left(y_{A,G} - HC_{A,L}/P\right)} \right) \tag{10}$$

Rearranging and simplifying, the final expression for $K_G a_V$ can be given as:

$$K_G a_V = \left(\frac{G_i}{P y_{A,G} - HC_{A,L}} \right) \left(\frac{dY_{A,G}}{dZ} \right) \tag{11}$$

The first term on the right-hand side of equation (11) was determined from the values of the operating conditions of the absorption experiment. The second term of the equation (concentration gradient ($dY_{A,G}/dZ$)) was obtained from slope of the measured CO_2 concentration profile, which was converted to a plot of the mole ratio $Y_{A,G}$. Figure (2) aid in illustrating the mechanics of the problem. It should be noted that this slope was not the global measure of entire profile but the local value, determined at a specific point of interest to give the $K_G a_V$ value at that particular condition. Finally, the relationship between mole fraction and mole ratio is defined:

$$y_{A,G} = \frac{Y_{A,G}}{1+Y_{A,G}} \tag{12}$$

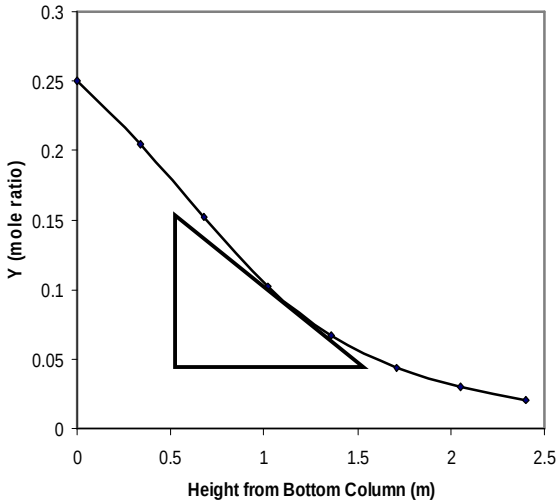

Figure (2) .Determining dY_A/dZ from the CO_2 mole ratio concentration profile.

3. Absorption System

The absorption columns are made out of acrylic plastic and have a height of 2.4 m and diameter of 0.2 m. Sampling points for the gas composition are located at regular intervals along the sides of each column. Column A has ten sampling points, while column B has eight gas sampling points. This is because of the types of packing used in the columns. The absorption process is carried out in a counter–current mode of operation. The feed gas composed of CO_2 and air enters at the bottom of the column and flows upwards. The prepared alkanolamine solution is pumped to the top of the column and flows downwards by gravity. The absorption CO_2 into alkanolamine solution occurs as the counter-current gas and liquid phases contact one another inside the absorption column. The packing promotes mixing and provides a surface area for contact between the two phases. Treated gas leaves at the top of the absorption column and the rich solution leaves at the bottom.

Column A is randomly packed with 19 mm Raschig rings. Column B is packed with Gempak 4A and rotated 90º with respect to each other in succession[5], and the data for the packing types used in this study are provided in Table (1). This is standard arrangements for structured packing in order to achieve optimum performance, as recommended by the manufactures.

Table (1). Packing data [6].

Packing Type	Surface area (m^2/m^3)	% Voids
19 mm Raschig	245	80
Gempak 4A	446	92

4. Experimental Procedures

In the present work, CO_2 absorption experiments were carried out to generate mass transfer efficiency data of different solvents over ranges of operating and design parameters. The experiments were carried out in the Engineering Process Laboratory, School of Chemical Engineering and Analytical Science, The University of Manchester as shown in Figure (3). Prior to a specific experimental run of the pilot plant, the variables for considerations had to be determined. Such variables consisted of the Amine solution concentration, the solution CO_2 loading, the percent of CO_2 in the feed gas, the liquid flow rate, the inert gas flow rate and the column packing type.

An aqueous solution of MEA, DEA, AMP, or MDEA was prepared in the feed tank, at a given concentration. The absorption experiment began by introducing a gas mixture of compressed air from air from a central supply and CO_2 from a cylinder to the bottom of an absorption column at a desired flow rate. The prepared aqueous solution was simultaneously pumped to the top of the column to create counter current contact between gas and liquid. The operation was continued for at least 30 minutes to allow the system to reach the steady state. At this point, the CO_2 concentrations in the gas phase at different positions along the column were measured through a series of a sampling points by switching the sampling point from one port to another using the IR analyzer. Finally, a liquid sample was taken from the bottom of the column and analyzed for its composition. The system operating conditions used in the present work are summarized in Table (2).

Table (2). List of operating conditions.

Conditions	Range
Liquid Flow Rate ($m^3/m^2.hr$)	7.69-19.22
Gas Flow Rate ($mol/m^2.s$)	9-17
CO_2 Feed %	5-20
Amine Concentration ($kmol/m^3$)	1-3
Inlet CO_2 loading (mol CO_2/mol MEA)	0-0.2
Inlet Gas Temperature (ºC)	23-27
Inlet Liquid Temperature (ºC)	23-26

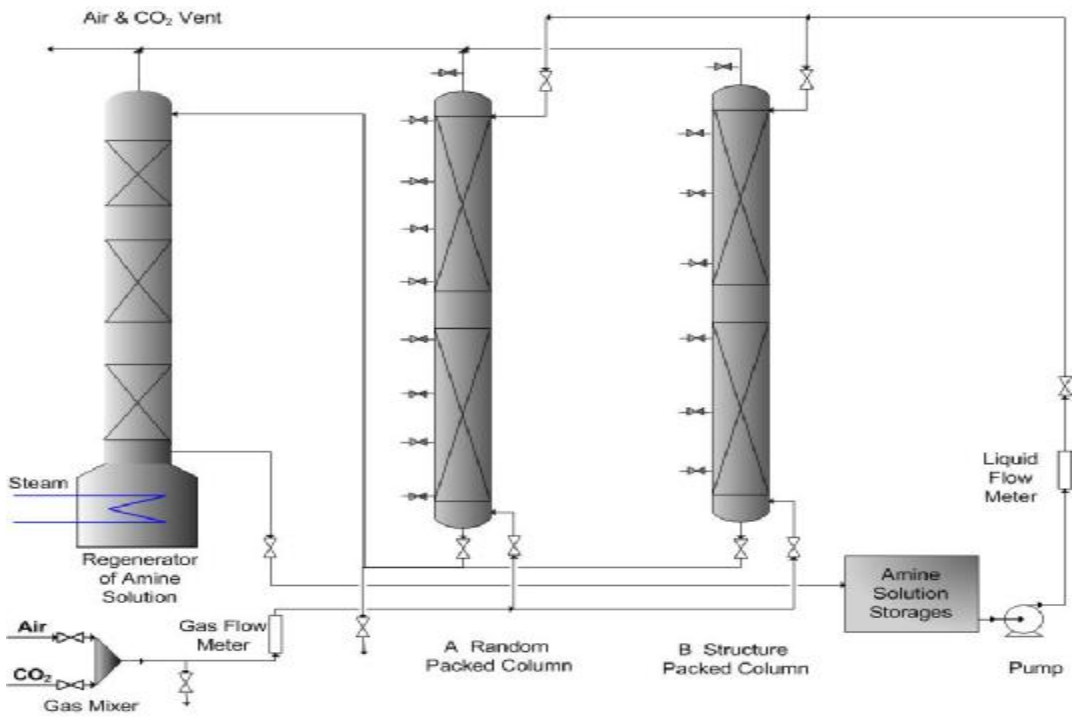

Figure (3). Experimental apparatus for CO_2 absorption.

5. Results and Discussion

5.1.Effect of Liquid Flow Rate

Figure (4) shows that the liquid load or flow rate has an influence on the value of $K_G a_v$; i.e., an increase in liquid load generally yields a greater $K_G a_v$ value. The possible reason for this behavior is that a higher liquid load leads to a greater liquid side mass-transfer coefficient, which is directly proportional to the overall $K_G a_v$ in the case of liquid-phase controlled mass transfer, and a greater effective area, which is caused by more liquid spreading on the packing surface.

5.2.Effect of Gas Flow Rate

According to Figure (5), the $K_G a_v$ value unaffected by the gas flow rate through the absorber over a range of 9-17 mol/m^{2}s. Logically, an increase in the gas load allows more CO_2 molecules to travel from gas bulk to the gas liquid interface, which would result in higher

mass transfer performance. However, the rate of gas absorption is not exclusively dependent upon the mass-transfer phenomenon in the gas phase. The mass-transfer behavior in the liquid phase also plays an important role. In the case when the $K_G a_v$ value is unaffected by an increasing gas load, the liquid-phase mass transfer is considered to be the major factor controlling the absorption process.

5.3.Effect of Solvent Concentration

According to Figure (6), an increase in the solvent concentration induces a higher $K_G a_v$. This effect is simply due to an increase in the enhancement factor, which is functionally related to the absorbent concentration. The possible explanation for this behavior is that increasing the solvent concentration reflects higher amounts of solvent molecules per unit volume available for absorbing more CO_2 at the gas-liquid interface. $K_G a_v$ values rise to a maximum and then fall as solution concentration increase beyond 3 kmol/m^3. The reduction in $K_G a_v$ values is blamed on an increase in solution viscosity as concentration rise, thus hindering molecular diffusion.

5.4.Effect of Feed CO2 Loading

The effect of feed CO_2 loading on overall mass transfer coefficient $K_G a_v$ of absorption column is shown in Figure (7). As feed CO_2 loading increases the concentration of free amine decrease, which leads to lower absorbent concentration. The enhancement factor is expected to reduce and the $K_G a_v$ decreases.

5.5.Effect of Feed CO2 Concentration

From Figure (8), $K_G a_v$ is reduced by 72% when the feed CO_2 concentration is raised from 5% to 20%. However, the opposing effects of the reducing $K_G a_V$and the increasing inlet CO_2 partial pressure caused the actual mass flux of CO_2 absorbed in the system to remain relatively constant. The restricted diffusion of solvent molecules in the liquid phase is speculated to be the cause of this behavior. As mentioned previously, the restricted diffusion in the liquid phase basically results in a constant amount of CO_2 absorbed. Therefore, higher CO_2 concentrations lead to a reduction in the $K_G a_v$ value.

5.6.Effect of Solvent Type

The $K_G a_v$ comparison between the all systems at a specific operating condition is also illustrated in Figure (9), the CO_2-MEA system provides approximately 3 times higher $K_G a_v$ than the CO_2-AMP system does. The difference between the $K_G a_v$ values of the absorption systems is primarily influenced by the rate constant (k_2). The greater the rate constant, the higher the $K_G a_v$ value would be expected.

The $k_{2,MEA\text{-}CO2} > k_{2,DEA\text{-}CO2} > k_{2,AMP\text{-}CO2} > k_{2,MDEA\text{-}CO2}$ thus leading to higher $K_G a_v$. Besides the influence of k_2, the surface tension of the liquid solvents also plays an important role on $K_G a_v$. In general, a lower surface tension would allow a greater effective mass transfer area, resulting in a greater $K_G a_v$.

5.7.Effect of Packing Type

The column packing plays a very important role in the absorption process as it provides a surface area for the gas and liquid phases to contact upon. Furthermore, it also promotes mixing of the two phases. Figure (10) shows the $K_G a_V$ values obtained for the two types of packings used in this study. These experimental runs are conducted under identical conditions. With only difference being the packing itself. The Gempak 4A packing produces $K_G a_V$ values are well over twice as large as those obtained in a randomly packing of Rasching ring. This due to the significantly larger contacting surface area and improved flow distribution for the contacting phases.

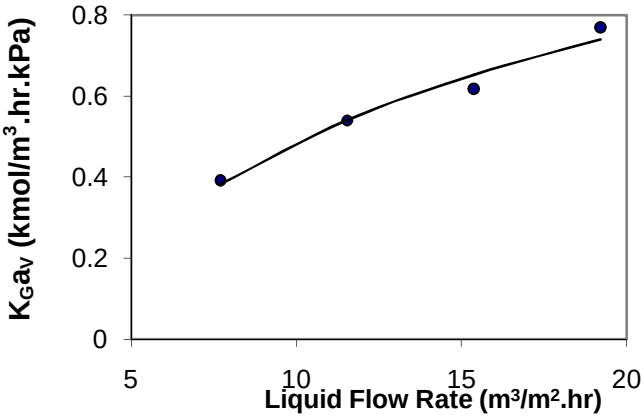

Figure (4). Effect of liquid flow rate on overall mass transfer coefficient for CO_2-MEA system (gas flow rate 9 mol/m^2.s, solution concentration 3 kmol/m^3, CO_2 feed 20% , CO_2 loading of lean solution 0.18 mol/mol).

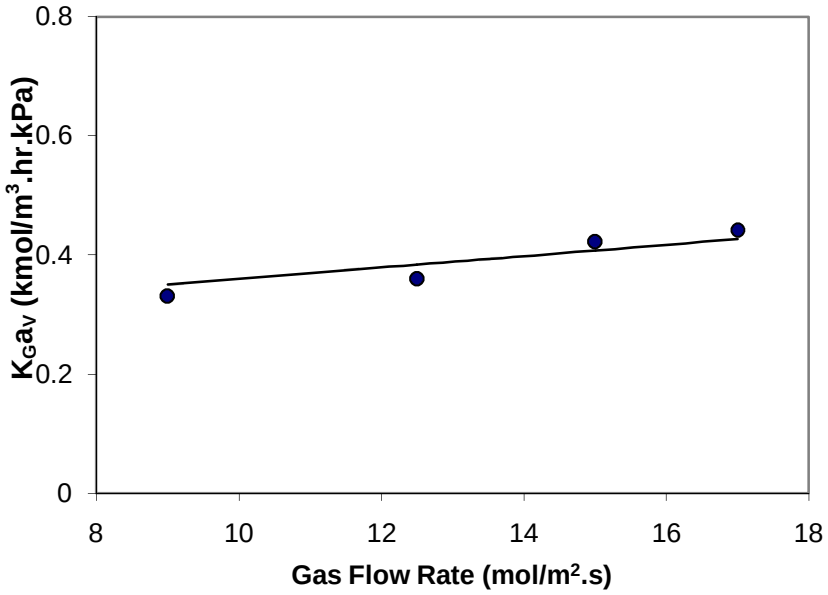

Figure (5). Effect of gas flow rate on overall mass transfer coefficient for CO_2-MEA system (liquid flow rate 7.69 m^3/m^2.hr, solution concentration 3 $kmol/m^3$, CO_2 feed 20% , CO_2 loading of lean solution 0.2 mol/mol).

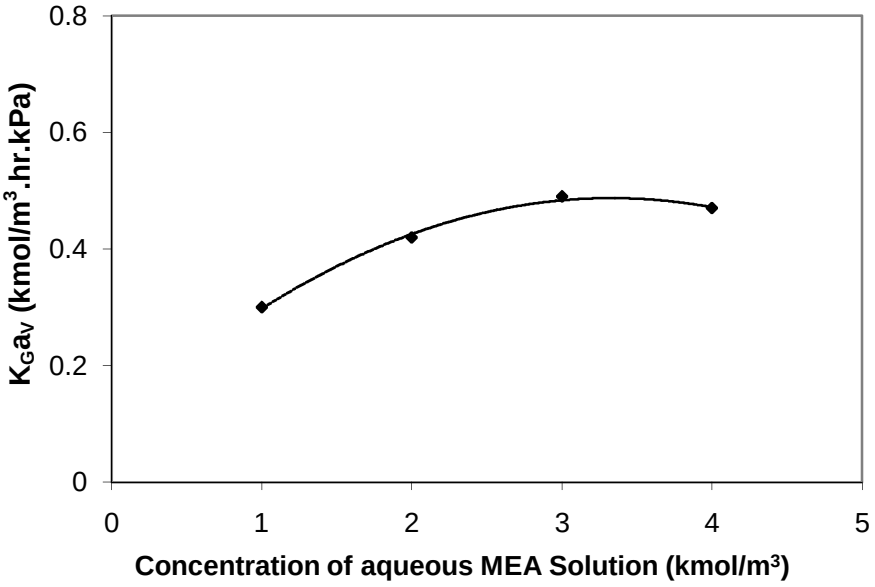

Figure (6). Effect of solution concentration on overall mass transfer coefficient for CO_2-MEA system (gas flow rate 9 mol/m^2.s, liquid flow rate 7.69 m^3/m^2.hr, CO_2 feed 10% , CO_2 loading of lean solution 0.18 mol/mol).

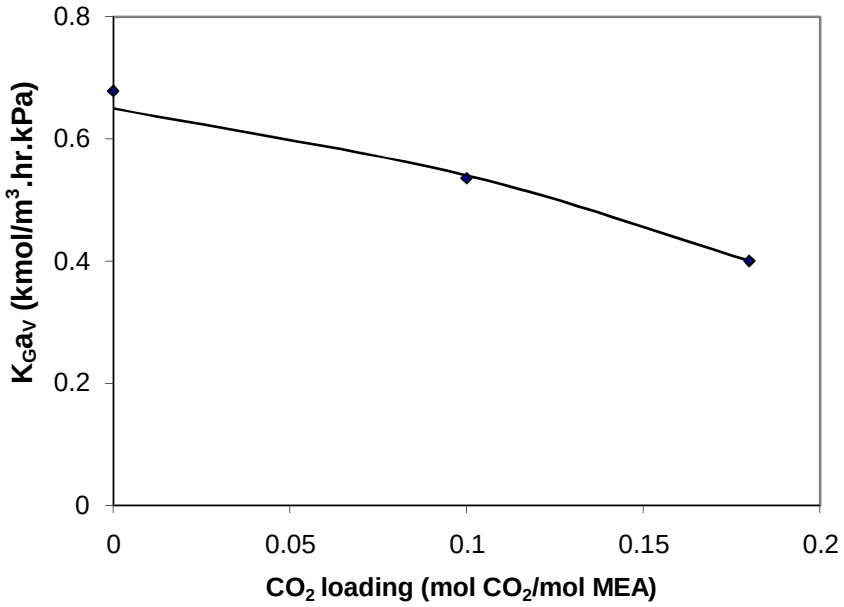

Figure (7). Effect of CO_2 loading of lean solution on overall mass transfer coefficient for CO_2-MEA system (gas flow rate 9 mol/m^2.s, liquid flow rate 7.69 m^3/m^2.hr, solution concentration 3 kmol/m^3, CO_2 feed 15%).

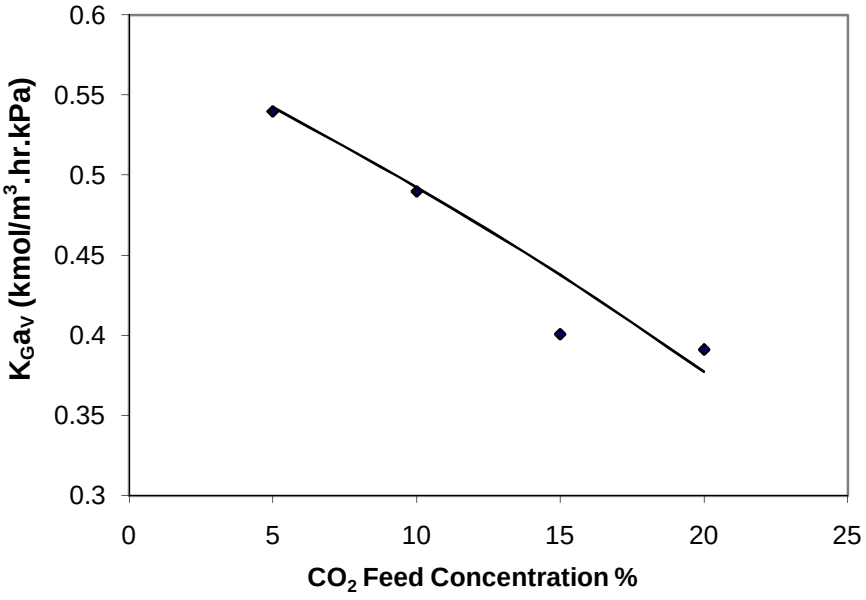

Figure (8). Effect of feed CO2 concentration on overall mass transfer coefficient for CO2-MEA system (gas flow rate 9 mol/m2.s, solution concentration 3 kmol/m3, , liquid flow rate 7.69 m3/m2.hr, CO2 loading of lean solution 0.18 mol/mol).

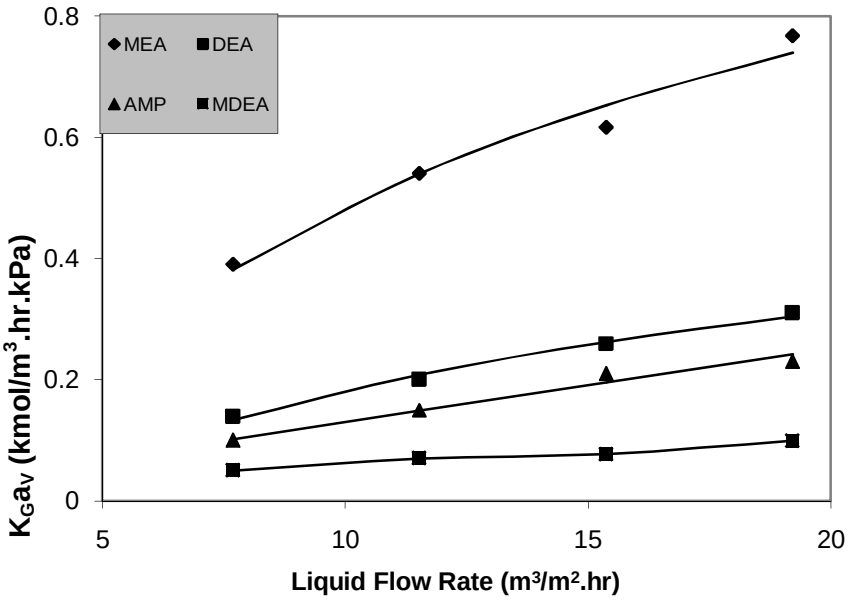

Figure (9). Effect of liquid flow rate on overall mass transfer coefficient for CO2-MEA system (gas flow rate 9 mol/m2.s, solution concentration 3 kmol/m3, CO2 feed 20%, CO2 loading of lean solution 0.18 mol/mol).

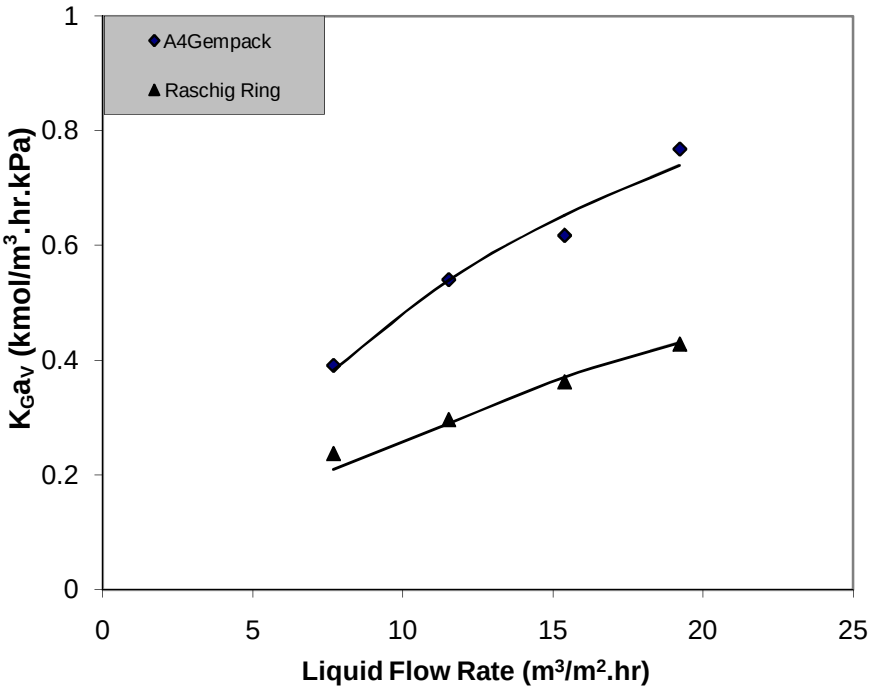

Figure (10) .Effect of packing type on overall mass transfer coefficient (gas flow rate 9 mol/m2.s, solution concentration 3 kmol/m3, CO2 feed 20% , CO2 loading of lean solution 0.18 mol/mol).

6. Conclusions

The following conclusions may be drawn:

(1) An increase in liquid load generally yields a greater $K_G a_v$.

(2) Gas load has no influence on $K_G a_v$.

(3) Increasing the reagent concentration therefore increases the value of $K_G a_v$ and improves the CO_2 removal performance of the system.

(4) Solvent type also has an effect on $K_G a_v$. In summary the$K_G a_v$ of the systems investigated can be expressed in the order CO_2-MEA> CO_2-DEA> CO_2-AMP> CO_2-MDEA.

(5) Structured packing offers superior performance to random packings. Structured packing (Gempak4A) provides almost twice greater $K_G a_v$ than random packings (Raschig rings).

(6) Increasing the CO_2 concentration within the gas stream to values of up to 20% was found to reduce the value of $K_G a_V$ within the system.

(7) As the CO_2 loading increases the concentration of active reagent molecules in the liquid is reduced and hence the $K_G a_V$ value decreases.

7. References

[1] Freguia, S. (2002). Modeling of CO_2 Removal from Flue Gases with Monoethanolamine, M.Sc. Thesis, The University of Texas at Austin.

[2] Geankoplis, C. J. (1993). Transport Process and Unit Operation, 3rd Ed., Prentice Hall Inc., New Jersey, USA.

[3] Kohl, A. L. and R. B. Nielsen (1997). Gas Purification, Gulf Publishing Company, Houston.

[4] Levenspiel, O. (1999). Chemical Reaction Engineering: Third Edition, John Wiley, Inc., New York.

[5] Aroonwilas, A. et al. (1999). Behaviour of the Mass-Transfer Coefficient of Structured Packings in CO_2 Absorbers with Chemical Reactions, Journal of Industrial Engineering Chemical Research, 38:2044–2050.

[6] Perry, R. H. and Green, D. (1997). Perry's Chemical Engineers' Handbook: 7th Edition, McGraw-Hill, New York.

8. Nomenclature

symbol	Description	Unit
A_C	cross-section area of column	m^2
A_e	gas-liquid interfacial area	m^2
a_v	effective interfacial area per unit volume of packing	m^2/m^3
C_A	concentration of component *A*	$kmol/m^3$
$C_{A,i}$	concentration of component *A* at gas-liquid interface	$kmol/m^3$
$C_{A,L}$	concentration of component *A* in the liquid bulk	$kmol/m^3$
G_i	inert molar gas load	$kmol/m^2.s$
H	Henry's law constant	$m^3.kPa/ kmol$
K_G	overall gas mass-transfer coefficient	$kmol/m^2.s.kPa$
N_A	mass transfer flux of component A	$kmol/m^2.s$
P	total pressure	kPa
Y_A	mole ratio of component *A* in gas bulk	mol/mol
$y_{A,G}$	mole fraction of component *A* in gas bulk	mol/mol
$y_{A,i}$	mole fraction of component *A* at gas-liquid intertface	mol/mol
Z	packing height	m

Minimizing Power Consumption in Combinational Logic Circuits by Reducing Switching Activity

Nahla D. Habeeb

Electrical Engineering dept.

College of Engineering

University of Mustansirya

Abstract

The aim of the present paper is to investigate the minimization of the power consumption in combinational circuits by reducing the switching activity. A synthesis approach based on an iterative procedure that compares the minterms consequently, eliminate the complementary variables, then ORing all the terms in one simplified equation is introduced . The results show that about 10% reduction in switching activity has been obtained by using this method if it is compared with the normal optimal solution obtained from K-map method.

Key Word: switching activity, low-power consumption, combinational circuits,CMOS circuit , K-map.

تقليل القدرة المستهلكة في الدوائر المنطقية بتقليل فعالية التشغيل

المستخلص

يهدف البحث الحالي الى دراسة تقليل القدرة المستهلكة في الدوائر المنطقية بتقليل فعالية التشغيل . يستند الاسلوب المتبع في البحث على عملية متتابعة يتم فيها مقارنة المدخلات المتشابهه (ذات الخرج ١) واختزال العناصر المتتامة ثم جمع الحدود المبسطة في معادلة واحدة. تشير النتائج الى ان فعالية التشغيل قد تم تقليلها بحدود ١٠% عند استخدام هذه الطريقة بالمقارنة مع تلك الدوائر المصممة باستخدام الطريقة التقليدية في مخطط كارنوف .

1. Introduction

The popularity of small, portable communications and computing devices has contributed to increasing interest in producing digital circuits with low power consumption and long operation lifetime. The power dissipated in CMOS circuits has two components: static, due to leakage current, and dynamic, due to switching activity. The static power is relatively low and is often neglected in power estimation. The dynamic component of power which occurs only during transition of internal circuit nodes from one logic level to another is given by the following expression:

$$P = \sum_{i} V_{DD}^{2} C_L f E_{sw} \quad (1)$$

Where V_{DD} is the power supply voltage in CMOS logic, C_L is the load capacitance at node i , f is the frequency of operation of the circuit , $E_{sw}$is the power consuming switching activity at node i, (number of gate output transitions/clock cycle)[1-4].It is understood from the above expression of the power consumption ,for a given CMOS technology with specified supply voltage of the circuit design, switching E_{sw} of a node i is the only parameter that affects the power consumption[5],since it is dependent on the input pattern and the circuit structure. A method for calculating the switching for combinational circuits realized using gate logic was presented in [6], where the switching activity for a logic gate refers to the total number of 0 to 1 and 1 to 0 transitions occurring at the output of the gate while all possible two pattern input sequences are applied at the input of the gate. By using their definition the switching activity for a logic gate can be evaluated by the following expression,

$$A_T = \sum A_i = \sum_{i} 2 \left| F_i \right| \left| R_i \right| \quad (2)$$

Where ATis the total switching activity of the circuit, and A_i is the activity at node i. F_i represents the set of minterms of the logic function realized at node i and Ri represents the maxterms. $\left| F_i \right|$ and $\left| R_i \right|$represent the cardinality of the sets Fi and Ri respectively. The switching activity estimation by assigning an integer value as defined in [6] makes it almost impossible for comparing different circuits since there is no reference metric on which comparisons can be made .Even though [6] provides a method for reducing the switching activity ,it does not provide a formal procedure for the design of a combinational circuit with reduced switching activity .A disjoint implicant approach for reducing the switching activity was proposed in[7],that aimed at increasing the number of inputs to a gate. The partitioning of

the prime implicants of a minimal sum -of -products expressions that share minterms into disjoint implicants increase the number of inputs to a gate ,which directly reduce the switching activity by 10% with marginal increase in circuit area and delay. An algorithmic approach using K-map had been proposed in [3], which modifies the normal optimal solution obtained from K-map to reduce its switching activity providing for more than 10% reduction in switching activity. In this paper a synthesis approach for reducing switching activity of many combinational logic circuits depending on the truth table of the logic expression is proposed.

2. Switching Activity in CMOS Combinational Logic Circuits

To estimate the power consumption of a circuit with high accuracy, a large number of input signal patterns should be simulated and the average value of E_{sw}calculated [8]. Switching activity can be calculated by a probability propagation algorithm whereby the transition probability of an internal circuit node is calculated from the signal probabilities of the primary input variable .The signal probability can be represented as follow [9]:

There is a binary sequence x (of length l), where m bits are logic 1.Then the probability that the signal is measured as 1 in a random clock cycle is m/l, and one can denote:

$$P(x=1) = m/ l \quad (3)$$

Obviously, there is n-bits (n= L-m) which has logic 0 in the sequence. Therefore the probability that the signal is measured as 0 in a random clock cycle is n/ L ,and one can denote

$$P(x=0) = n/ l \quad (4)$$

Therefore $p_{0\to1} = n / l * m/ l$ and $p_{1\to0} = m/ l * n/ l$,where $p_{0\to1}$ and $p_{1\to0}$ are the transition probabilities of the outputs switching from 0→1and 1→0 respectively .But battery power consumed is only when the output switches from 0 → 1 so the switching activity of two input AND gate equal to 3/16 ,for inverter equal to 1/4 ,for three input AND gate equal to 7/64 and for four input AND gate equal to 15/256 ,from this it is clear that switching activity is maximum when the number of $1'$S and $0'$ S of the function are equal .Since inverter has equal number of $1'$S and $0'$ S in its function ,it has the highest switching activity and this

explain why one have to avoid input inverters in designing logic circuits. Switching activity of a gate is also a function of the number of inputs to the gate .

A gate with fewer inputs will have higher switching activity compared to a gate with more inputs .Hence increasing the number of inputs to a gate is also an important design consideration for combinational logic design for reduced switching activity.[3,7]

3. Design of combinational logic circuits with minimum switching activity

In this section a simple procedure is introduced for designing low power consumption logic circuit based on writing the truth table of the logic expression then comparing the minterms respectively in order to eliminate the complementary variable, then eliminate the same minterm if exist, compare the remaining variable to see if it is possible to eliminate the complementary variable if exist as shown in the two example below:

Example 1: **F=∑ 0,1,4,5**

A B C DA B C DA B C D

0 0 0 **0** 0 **0** 0 --- 0 --- 0 ---

0 0 0 **1** ⇒ ---------- ⇒ ⇒ - - AC

0 1 0 **0** 0 **1** 0 --- ----------

0 1 0 **1** ----------

Example 2: **F=∑ 0,2,4,6**

A B C DA B C DA B C D

0 0 **0** 0 0 **0** -- 0 0 -- -- 0

0 0 **1** 0 ⇒ ---------- ⇒ ⇒ - - AD

0 1 **0** 0 0 **1** -- 0 ----------

0 1 **1** 0 ----------

So one can get the simplified minterm with no need to draw the K-map.

4. Simulation results

1- $f_1 = \sum 1, 3, 5, 8, 9, 11, 13, 15$

$f_1 = \bar{a}\bar{b}d + bc\bar{d} + ab\bar{c} + acd$ **{using the proposed method}**

$= \underbrace{(a+b)}_{3/16}d + b\underbrace{\bar{c}}_{1/}d + a\underbrace{(b+c)}_{3/1} + \underbrace{acd}_{7/64}$

7/64 7/64 7/64

1/4

Switching activity for this implementation is:

E_{sw} 1/4, 3/16, 7/64, 7/64, 3/16, 7/64, 7/64, 1/4

$f_1 = c\bar{d} + a\bar{b}\bar{d} + ad + ab\bar{c}$ **{ using k- map method }**

$= c\bar{d} + \underbrace{(a+b)}_{3/16}d + \underbrace{a}_{3/16}d + a\underbrace{(b+c)}_{3/16}$

1/ 3/1 7/64 7/64

1/4

Switching activity for this implementation is:

E_{sw}=1/4, 3/16, 3/16, 7/64, 3/16, 3/16, 7/64, 1/4

There is about 10% saving in switching activity

2- $f_2 = \sum 0, 1, 4, 6, 9, 10, 12, 14$ **{ using the proposed method }**

$f_2 = \bar{a}\bar{b}\bar{c} + b\bar{d} + ab\bar{c}d + ab\bar{c}\bar{d}$

$= \underbrace{(a+b+c)}_{7/64} + \underbrace{b\bar{d}}_{1/4} + \underbrace{ac}_{3/16}\underbrace{(b+d)}_{3/16} + \underbrace{ad}_{15/25}\underbrace{(b+c)}_{15/256}$

3/16

1/4

Total switching activity for this implementation:

E $_{sw}$=1/4, 7/64, 3/16, 3/16, 15/256, 3/16, 15/256, 1/4

f$_2$= ā b$^-$ c$^-$ + b d$^-$ + a c$^-$ d + b$^-$ c d$^-$ **{using the proposed method}**

= (a+ b + c) + b d$^-$ + a c$^-$ d + (b + d) c

1/4 1/4 3/16

7/64

3/16 7/64 7/64

1/4

Total switching activity for this implementation is:

E $_{sw}$ = 1/4,1/4, 7/64, 3/16, 7/64, 3/16, 7/64, ¼

There is about 11% saving in switching activity.

3 – f $_3$= ∑ 0, 1, 3, 4, 6, 7, 9, 12, 15

f $_3$ = ā b$^-$ c$^-$ + ā c d + ā b d$^-$+ a b c d + a b c$^-$d$^-$ + a b$^-$ c d$^-$ **{ using the proposed method }**

= (a+b+c) + ā c d + (a+d) b + a b c d + a b (c + d) + ac (b+d)

7/64 1/4 3/16 15/256 3/16 3/16

7/64 7/64 15/256 15/256

0.2211 0.145

63/256

Switching activity using this implementation is :

E $_{sw}$= 1/4 , 7/64 , 7/64, 3/16, 7/64, 15/256, 3/16, 15/256, 3/16, 15/256, 0.2211, 0.145,

63/256

f $_3$ = a$^-$ b$^-$ c$^-$+ a$^-$ c d + b c$^-$d$^-$ + b c d + b$^-$ c$^-$d + ā b d **{ using k- map method }**

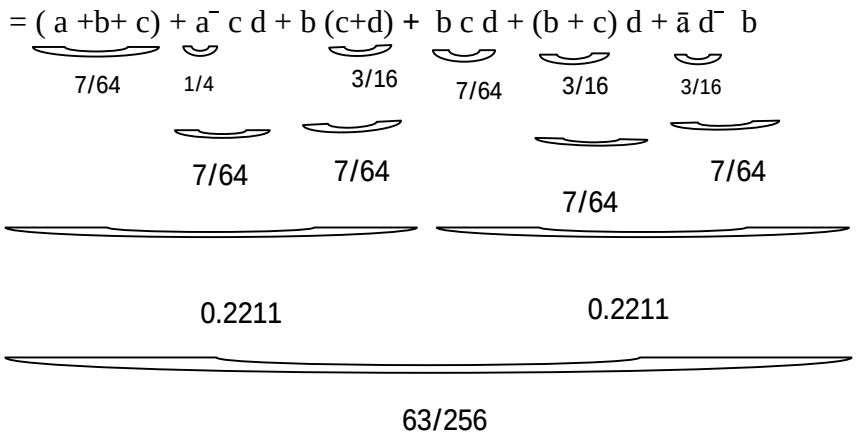

Switching activity using this implementation is :

E $_{sw}$ = 7/64, 1/4, 7/64, 3/16, 7/64, 7/64, 3/16, 7/64, 3/16, 7/64, 0.2211, 0.2211, 63/256

There is about 11% saving in switching activity.

5. Conclusions

In this paper a synthesis approach for the design of combinational logic circuits, with the primary objective of minimizing their switching activity is introduced. This paper shows clearly that there is no need to draw the k- map and to decide which group of minterms will be selected and which group will give the less switching activity, since from the truth table one can directly write the simplified equation which will give the optimum switching activity, the results shows that about 10% saving in switching activity is obtained using this procedure.

6. References

[1] M.S.Hsiao, 2002, Genetic Spot Optimization For Peak Power Estimation In Large VLSI Circuits, VLSI Design, Vol. 15 (1), pp. 407-416.

[2] M.S.Hsiao, E.M.Rudnick, and J.H.Pate, 2000, Peak Power Estimation of VLSI Circuits : New Peak Power Measures, IEEE Transactions on VLSI Systems, Vol. 8,No. 4.

[3] R.V.Menon, S. Chennupati, N.K.Samala,D.Radhakrishnan, andB.Izadi, 2004, Switching Activity Minimization In Combinational Logic Design, Proceeding of the International Conference on Embedded Systems and Applications, pp.47-53.

[4] M.Pedram,1996, Power Minimization In IC Design: Principles and Applications, Transactions of ACM, Vol.1, No. 1, pp.1-58.

[5] K.Paramasivam and K.Gunavathi, 2007, Switching Activity Based Method For Minimizing Testing Power In Digital Circuits, ECTI Transactions on Electrical Engineering, Electronics, and Communications, Vol.5, No.1.

[6] I.BrozozOwski and A.Kos, 1999, Minimization of Power Consumption In Digital Integrated Circuits By Reduction of Switching Activity, 2Sth Euromicro Conference, Vol.1 .

[7] R.V.Menan, S.Chennupati, N.K.Samala, D.Radhakrishnan, and B.Izadi, 2003, Power Optimized In Combinational Logic Design, Proceedings of International Conference on Embedded Systems and Applications, pp.223-227.

[8] A.Ghosh, S.Devadas, K.Keutzer, and J.White, 1992, Estimation of Average Switching Activity In Combinational and Sequential Circuits, In Proceedings 29th Design Automation Conf. pp. 253-259.

[9] Qing Wu, Xunwei Wu, 2003, A Note on The Relation Ship Between Signal Probability and Switching Activity, http/ www.cecs.uci.edu.

Laminar Fully Developed Forced Convection of Power Law Fluid in a Circular Tube

Ahmed J. Shkarah

Mechanical Engineering Department

Collegeof Engineering

University of Thi-Qar

Abstract

Laminar forced convection heat transfer in a non-Newtonian fluid flow inside a pipe has been investigated analytically. Fully developed laminar velocity distributions obtained by a power-law fluid rheology model is used, and viscous dissipation was taken into account. The theoretical analysis of the heat transfer is performed under a constant wall temp. case. An important feature of this approach is that it permits an arbitrary distribution of the surrounding medium temperature and an arbitrary velocity distribution of the fluid. These techniques were verified by a comparison with the existing results. The effects of the Brinkman number and rheological properties on the distribution of the local Nusselt number have been studied. It is shown that the Nusselt number strongly depends on the value of power law index. The Nusselt number sharply decreases in the range of $0 < n < 0.1$. However, for $n > 0.5$, the Nusselt number decreases monotonically with the increasing n, and for $n > 1$, the values of Nusselt number approach a constant value.

Keywords: Heat transfer, forced convection, Non-Newtonian fluid, analytical solution, viscous dissipation, Graetz's problem, laminar flow.

المستخلص

تم في هذا البحث دراسة نظرية لعملية انتقال الحرارة بالحمل القسري لجريان مائع غير نيوتوني متشكل هايدرودينيميكيا داخل انبوب دائري . المائع تم دراسته في مرحلة التشكيل التام هايدرودينميكيا واخذت فرضية الرفع للقوة كموديل لدراسة المائع .الدراسة النظرية اخذت فرضية ثبوت درجة الحرارة على الجدار وتمت دراسة مخططات السرعة ودرجات الحراة لتوزيعات مختلفة داخل الانبوب الدائريومعرفة تاثير ذلك على رقم نيسيلت .اعتمد الحل النظري على درجة الحرارة على الجدار .واستخدمت عده فرضيات اخرى للحل وقورنت بالنتائج .تم دراسية تاثير رقم برونكمان على رقم نيسلت ,ووجد ان رقم نيسلت يعتمد على قانون الرفع للأس ويقل عندما تكون قيمة اللأس اكبر من صفر واقل من العشر لذلك رقم نيسلت للاس اكبرمن خمسة اعشار يقل مع زياده قيمه اللاس و للقيم اكبر من الواحد .

1. Introduction

An understanding of convection heat transfer in non-Newtonian fluids inside pipes is crucial to the design of several types of thermal equipments. From this viewpoint, heat transfer problems of this type have been investigated by a number of researchers [1,2,3]. The problem pertaining to the derivation of the local Nusselt number in the thermal region when an incompressible fluid flows through a pipe with a fully developed velocity distribution is of particular interest; this problem is referred to as the Graetz problem. It has attracted the interest of not only engineers but also applied mathematicians because of the difficulties involved in deriving its solution. The original Graetz problem, which was first analytically solved by Graetz [4], is refer to the classical Graetz –Nusselt problem in single phase flow that neglects the effects of axial heat conduction, viscous dissipation, and thermal energy sources within the fluid. It is regarded as one of the most important solutions in the heat transfer science and it governs forced convection heat transfer for fluid with known velocity profile and involves finding of the heat transfer rate in a fully developed flow of fluid flowing inside conduit of various cross-sectional geometries with constant heat flux or constant wall temperature mode of heating. This type of solution allows temperature profile to be calculated from the coupled equations of motion andenergy [5].

A comprehensive analytically studies for the fully developed power-law fluid flowing in a circular tube for both uniform wall heat flux and wall temperature has been done [6] , but the authors neglected the effects of viscous dissipation. They show that the value of Nusselt number for a power-law fluid within uniform heat flux is given by:

$$Nu = \frac{8(3n+1)(5n+1)}{31n^2+12n+1} \tag{1}$$

Where n is the power-law index. For Newtonian fluid, i.e. for $n=1$, Eqn. (1) yields the well known result as:

$$Nu = \frac{48}{11} = const. \tag{2}$$

Where this result in Eqn. (2) was confirmed early by many number of authors [7,8].

However, the Graetz problem has been extended over problems that focus on turbulent flows, non-Newtonian flows, forced convection in a porous medium, and the effects of viscous dissipation for Newtonian fluid and that include effects of heat conduction [9-17]. In all the works cited above there is no studied related to the effects of viscous dissipation on heat transfer with non-Newtonian fluid.

Therefore, the objective of this study is to mathematically solve the forced convection heat transfer problem in a pipe subjected to constant wall temp. for fully developed region, which is a type of Graetz problem, and derive completely analytical solutions for the fluid temperature profile and local Nusselt number. Since the present study focuses on heat transfer with a sufficiently large Peclet number (Pe), the axial heat conduction is considered negligible. However, viscous dissipation is taken into account. Numerical calculations are performed to demonstrate the effects of the Brinkman number (Br) and rheological properties on the distribution of the local Nusselt number

2. Mathematical Model and Formulation

Figure (1)shows the physical model and coordinate system.A non-Newtonian fluid with fully developed velocity profile $u(r)$ flows into a cylindrical pipe of radius R .The pipe is convectively heated or cooled by the surrounding medium of constant wall temp. q_w.

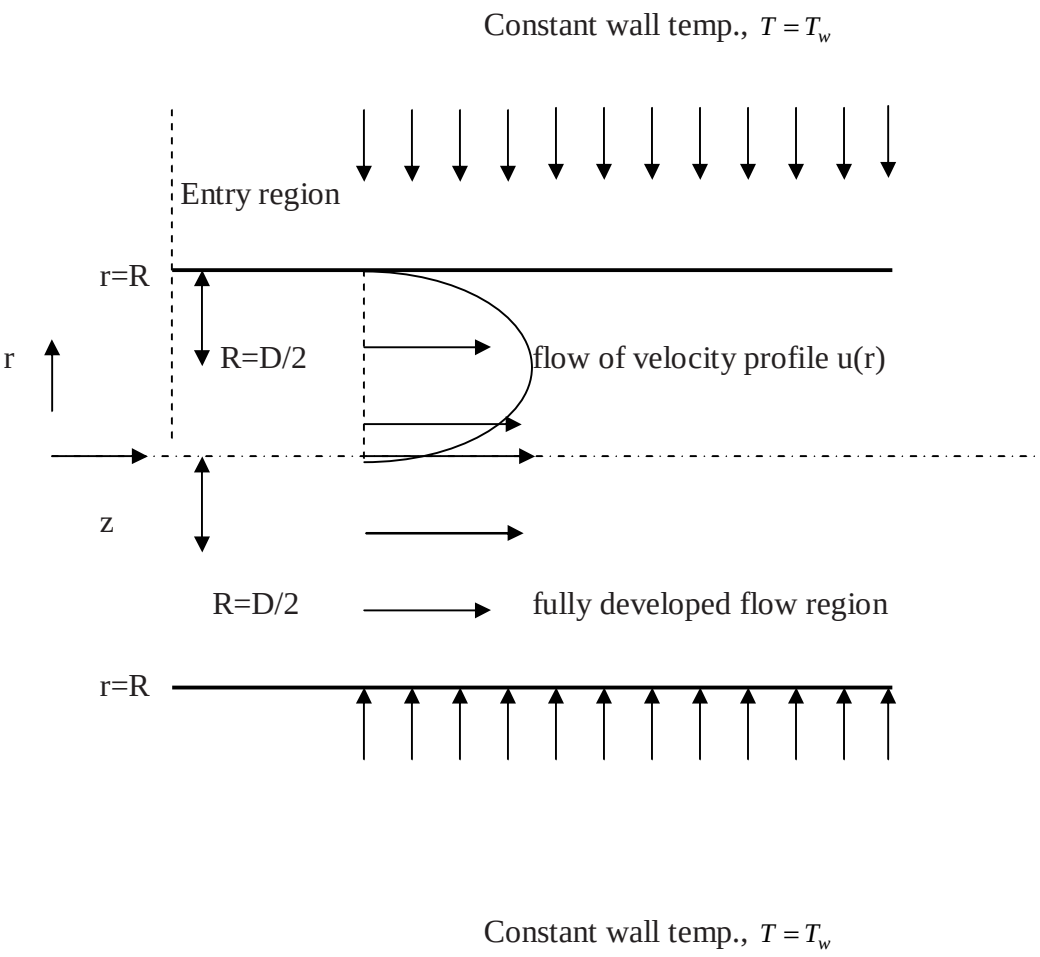

Figure (1). Notations and axes of the problem.

According to the type of fluid flowing inside the pipe, a power-law fluid, which can approximate the non-Newtonian viscosity of many types of fluids with good accuracy over a wide range of shear rates, is considered here. The shear stress (t_{rz}) acting on the viscous fluid is given by the formula [18]:

$$t_{rz} = -m\left|\frac{du}{dr}\right|^{n-1}\frac{du}{dr} \tag{3}$$

Where m and n are the power-law model parameter index, respectively. Depending on power law index (n); there are three cases as:

1. $n<1$ indicates that the fluid is a pseudo-plastic fluid,

2. $n=1$ indicates that the fluid is equivalent to a Newtonian fluid, and
3. $n>1$ indicates that the fluid is a dilatant fluid.

The fully developed velocity distribution is derived in terms of mean velocity (u_m) as follows [18]:

In order to illustrate the solution technique , a number of simplifying assumptions are made for the simplified of the basic equation as:

1. the flow mode is laminar, steady and axial symmetry.
2. the fluid physical properties are independent of temperature and pressure,
3. the axial heat conduction is negligible relative to radial heat conduction,
4. natural convection effects are neglected

$$\frac{u(r)}{u_m}=\frac{3n+1}{n+1}\left[1-\left(\frac{r}{R}\right)^{\frac{n+1}{n}}\right] \tag{4}$$

where (u_m) is the mean velocity.

By coupling Eqn. (3) with Eqn. (4), the shear stress for non-Newtonian power-law can be expressed by:

$$t_{rz}=m\left[\left(\frac{u_m}{R}\right)\left(\frac{3n+1}{n}\right)\left(\frac{r}{R}\right)^{1/n}\right]^n \tag{5}$$

In this case, the steady-state heat balance taking viscous dissipation into account is expressed as follows [18]:

$$k\frac{1}{r}\frac{\partial}{\partial r}\left(r\frac{\partial T}{\partial r}\right)=rc_p u(r)\left(\frac{\partial T}{\partial z}\right)-t_{rz}\left(\frac{du}{dr}\right) \tag{6}$$

Where ρ, c and k are the density, specific heat and thermal conductivity, respectively. In addition, the second term on the right-hand side is the viscous dissipationterm effects.

In order to avoid difficulties of definitions the heat transfer and to simplify the mathematical treatments, three modified boundary conditions are proposed and employed for special process requirements as:

-At pipe center; by applying constant centerline temperature gives:

-By symmetry, there can be no heat flux across the centerline in the pipe; this case means that the radial temperature gradient is zero, therefore:

B.C 1 r=0 at center line r=R at wall (7)

$$\text{B.C 2} \qquad \text{at } r=0 \qquad \frac{\partial T}{\partial r}=0 \tag{8}$$

-At pipe wall; the identified temperature gives the third boundary condition:

$$\text{B.C 3} \qquad \text{at } r=R \qquad T=T_w \tag{9}$$

Now, substituting the velocity profile, Eqn. (4), into energy balance Eqn. (6) yields;

$$\frac{1}{r}\frac{\partial}{\partial r}\left(r\frac{\partial T}{\partial r}\right)=\frac{u_m}{a}\left(\frac{3n+1}{n+1}\right)\left[1-\left(\frac{r}{R}\right)^{\frac{n+1}{n}}\right]\left(\frac{\partial T}{\partial z}\right)+\frac{m}{k}\left(\frac{3n+1}{n}\right)^{n+1}\left(\frac{u_m}{R}\right)^{n+1}\left(\frac{r}{R}\right)^{\frac{n+1}{n}} \tag{10}$$

Where a is thermal diffusivity and defined by:

$$a=\frac{k}{rc_p} \tag{11}$$

Generally, one tries to select dimensionless quantities so as to minimize the number of parameter in the final problem formulation and that is useful in scale-up problems by introducing the following dimensionless variables:

$$\left.\begin{aligned} x&=\frac{r}{R};h=\frac{z}{2RPe}\\ q&=\left(\frac{T_w-T(r)}{T_w-T_c}\right)\end{aligned}\right\} \tag{12}$$

Substitution of Eqn. (12) into Eq. (10) yields a dimensionless partial differential equation as:

$$\frac{1}{x}\frac{\partial}{\partial x}\left(x\frac{\partial q}{\partial x}\right)=\frac{1}{4}\left(\frac{3n+1}{n+1}\right)\left[1-x^{\frac{n+1}{n}}\right]\left(\frac{\partial q}{\partial h}\right)-Br\left(\frac{3n+1}{n}\right)^{n+1}x^{\frac{n+1}{n}} \tag{13}$$

Where the Brinkman number (Br) is defined by:

$$Br = -\frac{mu^{n+1}}{kR^{n-1}(T_w - T_c)} \tag{14}$$

and the Peclet number (Pe) is given by :

$$Pe = \frac{2u_m R}{a} \tag{15}$$

Based on these new parameters and Eqns. (7), (8) and (9), the dimensionless boundary conditions becomes as:

B.C: 1 at $x = 0$; $q = 1$ (16)

B.C: 2 at $x = 0$; $\frac{dq}{dx} = 0$ (17)

B.C: 3 at $x = 1$; $q = 0$ (18)

Generally for the case of constant wall temp., radial temperature profiles are well stabilized; so that $q(x,h)$ is a function of dimensional cylindrical coordinate (x) alone, the constancy of the flux implies that:

$$\frac{\partial q}{\partial h} = A_0 \tag{19}$$

where A_0 is a constant; substituting Eqn. (19) into Eqn. (13) yields an ordinary differential equation, as:

$$\frac{1}{x}\frac{d}{dx}\left(x\frac{dq}{dx}\right) = \frac{A_0}{4}\left(\frac{3n+1}{n+1}\right)\left[1 - x^{\frac{n+1}{n}}\right] - Br\left(\frac{3n+1}{n}\right)^{n+1} x^{\frac{n+1}{n}} \tag{20}$$

Let introduce new other simplified parameters as:

$$N = \left(\frac{3n+1}{n}\right)^{n+1} Br \tag{21}$$

$$C_0 = \frac{A_0}{4}\left(\frac{3n+1}{n+1}\right) \tag{22}$$

and

$$b = \frac{n+1}{n} \tag{23}$$

Now, substituting Eqns. (21), (22) and (23), into Eqn. (20) yields;

$$\frac{1}{x}\frac{d}{dx}\left(x\frac{dq}{dx}\right) = C_0\left(1-x^{b}\right) - Nx^{b} \tag{24}$$

This separable differential equation can be directly integrated twice with respect to dimensionless radial coordinate (x); the results give temperature profile in circular pipe as follows:

$$q(x) = C_0\left(\frac{1}{4}x^{2} - \frac{1}{(b+2)^2}x^{b+2}\right) - \frac{N}{(b+2)^2}x^{b+2} + C_1 \ln x + C_2 \tag{25}$$

in which C_1 and C_2 are constants of integration. These two constants can be evaluated from the first two boundary conditions Eqn. (16) and Eqn. (17) and by utilizing of Eqn. (25), as:

$$C_1 = 0 \quad \text{and} \quad C_2 = 1 \tag{26}$$

These two expressions of integration constants can be inserted into Eqn. (25) and rearranged to give the dimensionless temperature profile as follows:

$$q(x) = C_0\left(\frac{1}{4}x^{2} - \frac{1}{(b+2)^2}x^{b+2}\right) - \frac{N}{(b+2)^2}x^{b+2} + 1 \tag{27}$$

Based on the third boundary condition, Eqn. (18), with Eqn. (27), one can find parameter

$$C_0 = 4\left[\frac{\left(N-(b+2)^2\right)}{\left(4-(b+2)^2\right)}\right] \tag{28}$$

When substitution for C_0 into Eqn. (27), the local radial temperature distribution becomes as:

$$q(x) = \left(\frac{(N-C_0)}{(b+2)^2}\right)x^{b+2} + \left(\frac{C_0}{4}\right)x^{2} + 1 \tag{29}$$

In another form:

$$\frac{T_w - T(r)}{T_w - T_c} = \left(\frac{(N-C_0)}{\left(\frac{3n+1}{n}\right)^2}\right)\left(\frac{r}{R}\right)^{\frac{3n+1}{n}} + \left(\frac{C_0}{4}\right)\left(\frac{r}{R}\right)^{2} + 1 \tag{30}$$

This equation represents the temperature profile for power-law fluid in cylindrical pipe with viscous effects under the effect of constant wall temp..

In fully-developed flow, it is usual to utilize the bulk temperature (mean fluid temperature), T_b , rather than the center-line temperature when defining the Nusselt number [8,18]. This mean or bulk temperature is given by:

$$T_b = \frac{2p\,rc_p \int_0^{2p} \int_0^R T(r)u(r)rdrdq}{2p\,rc_p \int_0^{2p} \int_0^R u(r)rdrdq} \tag{31}$$

In dimensionless form of bulk temperature (q_b), Eqn. (31) becomes:

$$q_b = \frac{\int_0^1 q(x)f(x)xdx}{\int_0^1 fx(x)dx} \tag{32}$$

Where f is the dimensionless velocity profile and defined as:

$$f = \frac{u}{u_m} \tag{33}$$

By substitution velocity and temperature profiles Eqns. (4) and Eqn. (29) into Eqn. (32) becomes:

$$q_b = \frac{\int_0^1 \left\{\left[\left(\frac{(N-C_0)}{(b+2)^2}\right)x^{b+2} + \left(\frac{C_0}{4}\right)x^2 + 1\right]\left(1-x^b\right)\right\}xdx}{\int_0^1 \left(1-x^b\right)xdx} \tag{34}$$

Taking the generality of the analysis into account, this equation, Eqn. (34), can be readily integrated to obtain the dimensionless forms of bulk temperature as follows:

$$q_b == \left[\frac{2(N-C_0)}{(b+2)(b+3)(2b+3)}\right] + \left(\frac{C_0(b+2)}{8(b+4)}\right) + 1 \tag{35}$$

According to the axes that shown in Figure 1, the local heat transfer coefficient inside the pipe is normally defined by:

$$q_w = h(T_w - T_b) = k\left.\frac{dT}{dr}\right|_{r=R} \tag{36}$$

According to the definition the local Nusselt number (Nu) is given by:

$$Nu = \frac{hD}{k} = \frac{2R\left.\frac{dT}{dr}\right|_{r=R}}{(T_w - T_b)} \tag{37}$$

Based on dimensionless parameters, the local Nusselt number (Nu) is can be expressed by:

$$Nu = 2\frac{\left.\frac{dq}{dx}\right|_{x=1}}{(q_w - q_b)} \tag{38}$$

Where q_W is the dimensionless wall temperatures, which could be evaluated by $q_w = q|_{x=1}$, therefore when substitution in Eqn. (29), the results could be as:

$$q_w = q|_{x=1} = \left[\frac{(N - C_0)}{(b+2)^2}\right] + \left(\frac{C_0}{4}\right) + 1 \tag{39}$$

In addition, from Eqn. (29), the temperature gradient at wall $\left(\left.\frac{dq}{dx}\right|_{x=1}\right)$ is given as:

$$\left.\frac{dq}{dx}\right|_{x=1} = \frac{(2N + bC_0)}{2(b+2)} \tag{40}$$

By substitution the Eqns. (35), (39) and (40) into Eqn. (38) and simplified the results, the final results of Nusselt number (Nu) can be evaluated and expressed as:

$$Nu = \left[\frac{31n^2 + 12n + 1}{8(3n+1)(5n+1)} + 2^{n-1} Br\left(\frac{3n+1}{n}\right)^n\right]^{-1} \tag{41}$$

This equation represents the Nusselt number for power-law fluid in cylindrical pipe with viscous effects under the effect of constant wall temp. for fully developed laminar flow.

3. Results and discussion

In the absence of dissipation effect (Br=0) the solution is independent of whether there is wall heating or cooling. However, viscous dissipation always contributes to internal heating of the fluid; hence the solution will differ according to the process taking place. The Brinkman number (Br) is chosen as a criterion which shows the relative importance of viscous dissipation. For brevity and standing in a reasonable range, -1 < Br < 1. Where positive values of *Br* correspond to wall heating ($T_w > T_c$ and Br>0) case that mean heat is being supplied across the walls into the fluid, while the opposite is true for negative values of Br, that mean wall cooling cases ($T_w < T_c$ and Br<0).

As stated earlier that the thermal boundary conditions have been considered for the pipe wall as constant wall temp.. For this boundary condition both wall heating or wall cooling cases are examined and treated separately.

Figures (2a, b and c) show the temperature profiles made dimensionless using this scale for wall heating, no viscous dissipation and wall cooling cases, respectively, where these profiles based on Eqn. (29). These plots make clear the aforementioned effects of increased dissipation. As expected, increasing dissipation increases the bulk temperature of the fluid due to internal heating of the fluid. For the wall heating case, this increase in the fluid temperature decreases the temperature difference between the wall and the fluid, as will be shown later, which is followed with a decrease in heat transfer. When wall cooling is applied, due to the internal heating effect of the viscous dissipation on the fluid temperature profile, temperature difference is increased with the increasing Brinkman number (Br). In fact, wall cooling is applied to reduce the bulk temperature of the fluid, while the effect of the viscous dissipation is increasing the bulk temperature of the fluid. Therefore, the amount of viscous dissipation may change the overall heat balance. When the Brinkman number exceeds a certain limiting value, the heat generated internally by viscous dissipation process will overcome the effect of wall cooling.

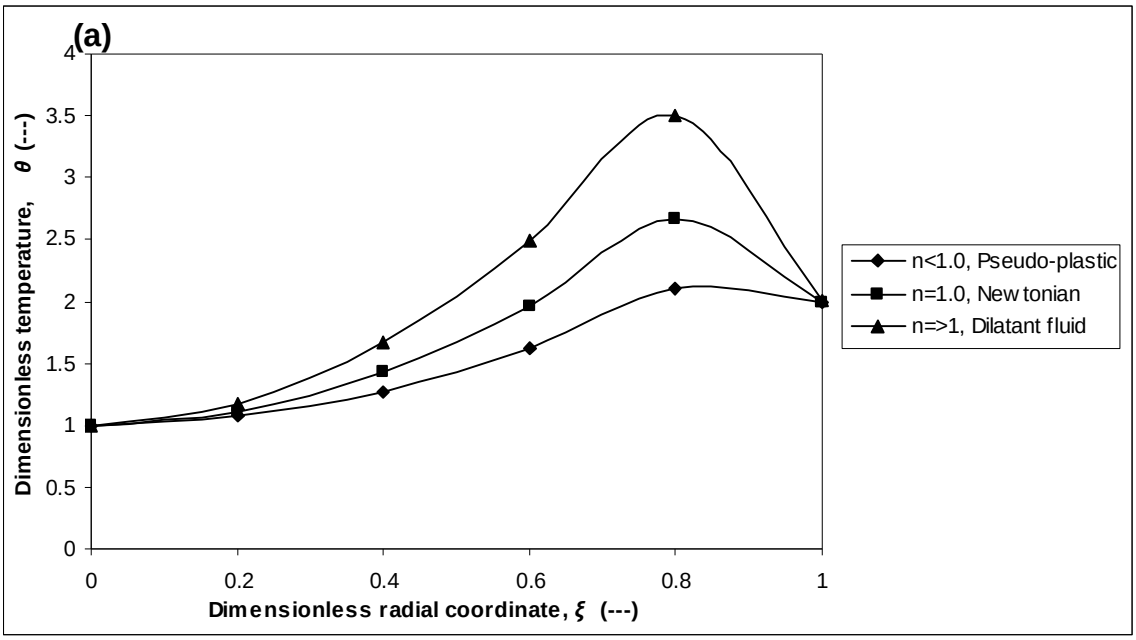

Figure (2- a)

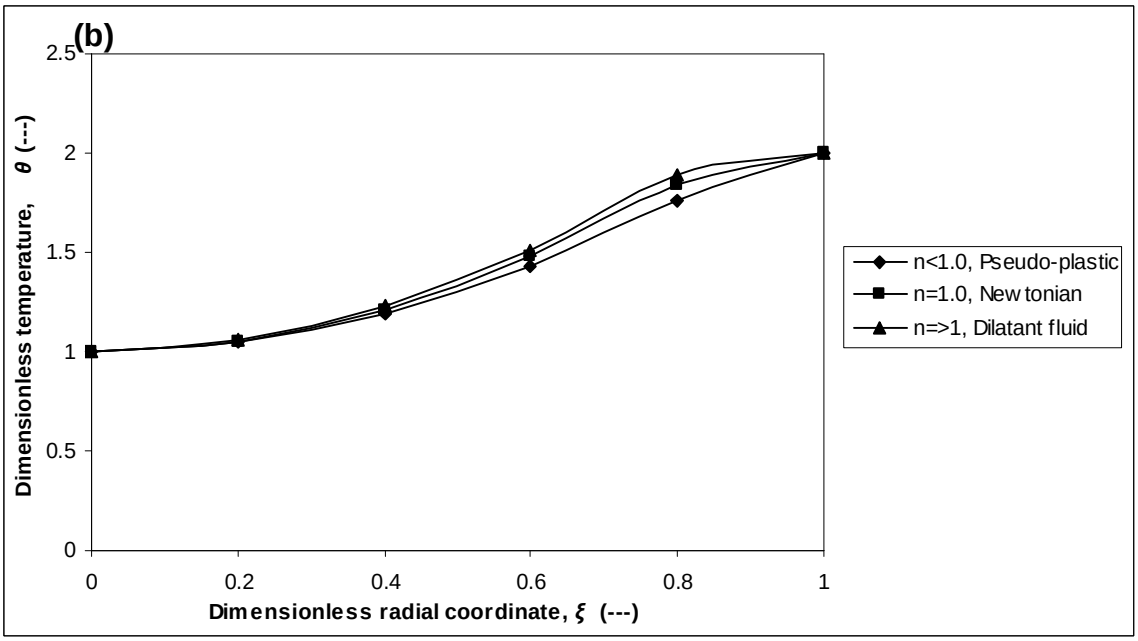

Figure (2-b)

Figure (2). Effects of power law index on dimensionless fluid temperature profiles for: (a) heating wall (Br=-1.0), (b) no viscous dissipation (Br=0.0), and (c) cooling wall (Br=1.0).

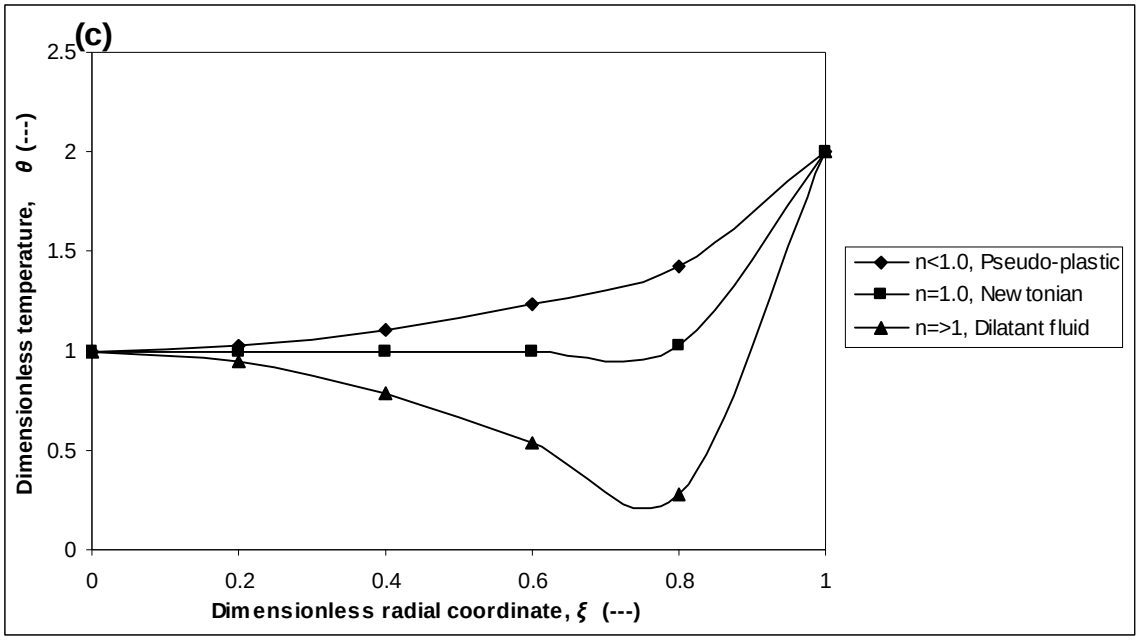

Figure (2-c)

Figure (3) represents the variation of Nusselt number with the rheological properties (power-law index) for constant wall temp. case with different values of Brinkman number. Where the asymptotic and downstream Nusselt number profiles are shown clearly for wall heating (Br > 0). When wall cooling (Br < 0) is applied to reduce the bulk temperature of the fluid, as explained earlier, the amount of viscous dissipation may change the overall heat balance. With increasing value of Br in the negative direction, the Nusselt number reaches an asymptotic value. As noticed, when Br goes to infinity for either the wall heating or the wall cooling case, the Nusselt number reaches the same asymptotic value. This is due to the fact that the heat generated internally by viscous dissipation processes will balance the effect of wall cooling. Generally, Nusselt number with viscous effects for both wall heating and wall cooling is less than Nusselt number for non viscous dissipation.

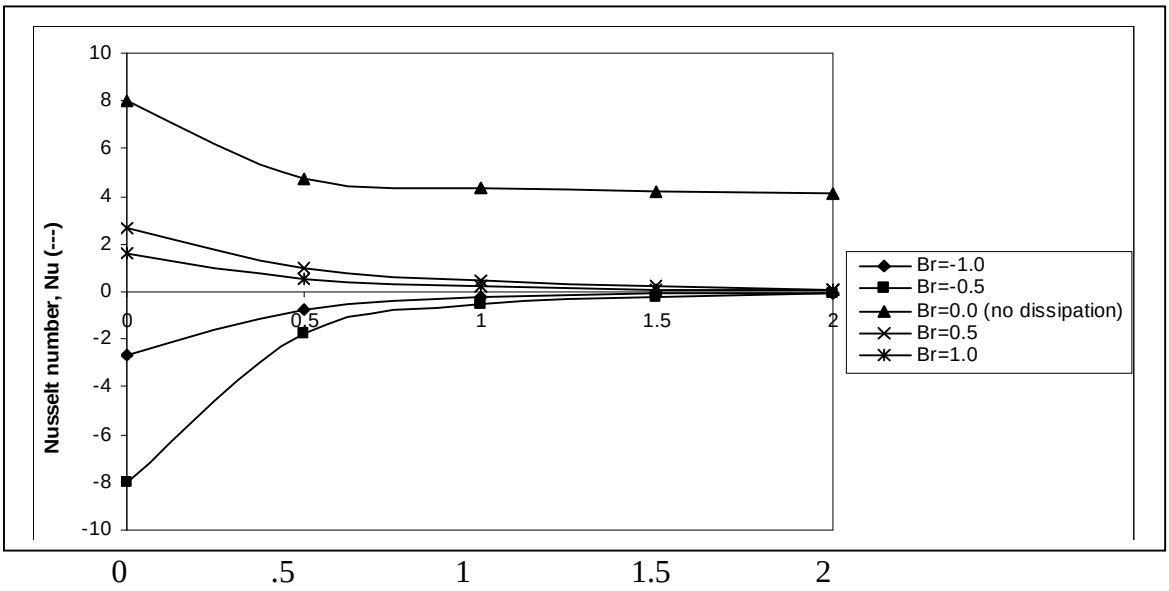

Figure (3). Effects of power-law index on Nusselt number for different values of Brinkman number.

While Figure (4) represents the variation of Nusselt number with the Brinkman number for constant wall temp. case with different values of power law index (n). Actually, this is an expected result, when Eqn. (41) is closely examined. For the wall heating case, with the increasing value of Br, Nu decreases to reach constant values. This is because the temperature difference which drives the heat transfer decreases. At Br=0.5, the heat supplied by the wall into the fluid is balanced with the internal heat generation due to the viscous heating. For Br > 0.5, the internally generated heat by the viscous dissipation overcomes the wall heat. When Br=1.0, Nu reaches an asymptotic value. Generally, Nusselt number Newtonian fluid is higher than those for pseudo- plastic and dilatants fluids.

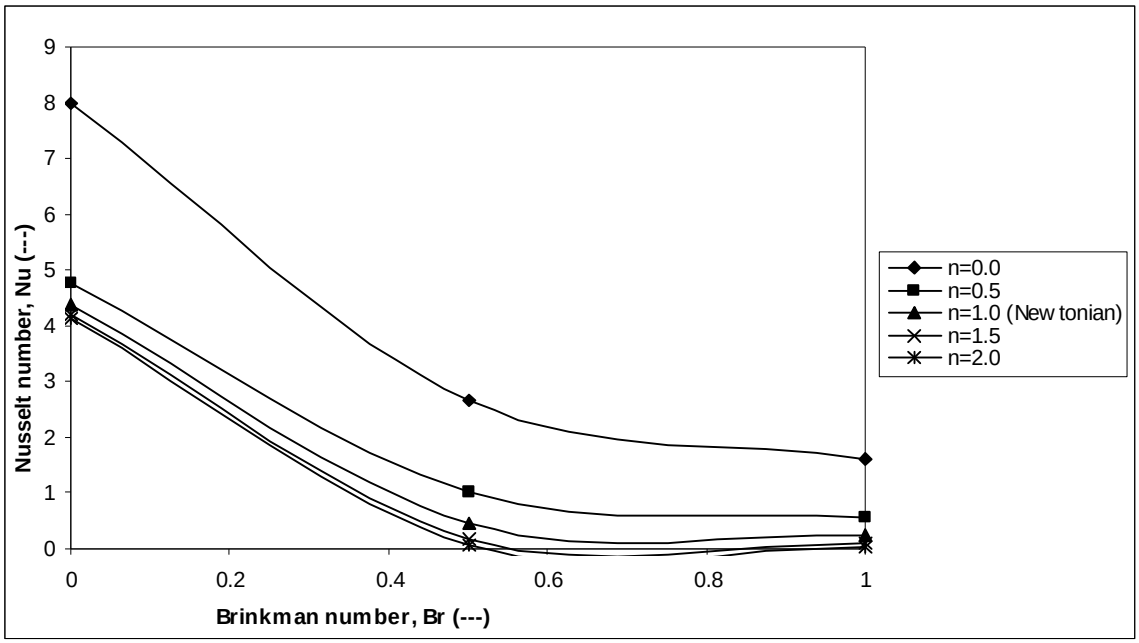

Figure (4). Effects of Brinkman number on Nusselt number for different values of power-law index.

4. Conclusions

The forced convection heat transfer problem with viscous dissipation inside a pipe subjected to constant wall temp. has been solved mathematically, which is a type of the Graetz problem. Completely analytical solutions for the fluid temperature and localNusselt number (Nu) have been derived. The effects of the Brinkman number (Br) and rheological properties (power-law index) on the distribution of the local Nusselt number have been shown through numerical calculations. The local Nusselt number in the thermal region tends to increase with a decrease in the power-law model index (n). It has been shown that viscous dissipation in the fluid can significantly influence laminar flow heat transfer.

With regard to the Graetz problem, the present analytical method can be applied to heat transfer not only in a pipe but also in a concentric annulus and a channel between parallel plates; it can also be applied to heat transfer in a channel with a moving wall because there is no restriction on the velocity distribution form of a fluid.

5. References

[1] Ou, J.,and Cheng, C. "Heat transfer in pipes with uniform heat flux" Appl. Sci. Res. Vol. 28, pp.289–301 (1973).

[2] Basu, T., and Roy, N. "Laminar heat transfer in a tube" Int. J. Heat and Mass Transfer, Vol. 28, pp.699–701(1985).

[3] Barletta, A., and Zanchini, E. "Forced convection in the thermal entrance region of a circular duct with slug flow and viscous dissipation" Int. J. Heat and Mass Transfer, Vol. 40, pp.1181–90 (1997).

[4] Brinkman, C. "Heat effects in capillary flow" Appl. Sci. Res., A2, pp.120–124, (1951).

[5] Kays,W., and Crawford, M., "Convective heat and mass transfer", 2nd Edition, McGraw-Hill, New York (1993).

[6] Abdulmohsin, R., and Abid, B., "Modeling of heat transfer to non-Newtonian power-law fluid in a tube", Eng. Journal of Nahrain University, Vol.6, pp.249-269 (2002).

[7] Lin, F., Hawks. H., and Leidenfrost, W. "Analysis of heat transfer in laminar pipe flows with convective boundary conditions" Int. J. Heat and Mass Transfer, Vol. 26, pp. 97–105 (1983).

[8] Rohsenow, W., Hastnetti, J., and Gonic, E. " Handbook of heat transfer applications" 2nd Edition , McGraw-Hill Com., New York (1985).

[9] Dang, D. "Heat transfer of a power-law fluid at low Peclet number flow" J. Heat Transfer, Vol.105, pp.542–549 (1983).

[10] Liou, T., and Wang, S. "Solutions to the extended Graetz problem for a power-law fluid with different entrance boundary conditions" Numerical Heat Transfer, Vol. 17, pp. 91–108 (1990).

[11] Liou, T., and Wang, S. "Solutions to the extended Graetz problem for a power-law fluid with different entrance boundary conditions" Numerical Heat Transfer, Vol. 17, pp. 91–108 (1990).

[12] Lawal, A., and Mujumdar, S. "The effects of viscous dissipation on heat transfer in arbitrary cross sectional ducts" Int. J. Heat and Mass Transfer, Vol. 35, pp.437–46 (1992).

[13] Zanchini E. "Effect of viscous dissipation on the asymptotic behavior of laminar forced convection in circular tubes" Int. J. Heat and Mass Transfer, Vol. 40, pp.169–178 (1996).

[14] Lahjomri, J., Zniber, K., Oubarra, A., and Alemany, A. "Heat transfer by laminar flow in the thermal entrance region with uniform wall heat flux: the Graetz problem extended" Energy Conversion and Management, 2003, Vol.44, pp.11–34 (2003).

[15] Aydın, O., "Effects of viscous dissipation on the heat transfer in a forced pipe flow; Part 1: hydrodynamicly developing flow " Energy Conversion and Management, Vol. 46, pp.757–69 (2005).

[16] Aydin, O. "Effects of viscous dissipation on the heat transfer in a forced pipe flow; Part 2: thermally developing flow" Energy Conversion and Management, Vol. 46, pp.3091–3102 (2005).

[17] Bird, B., Stewart, E., and Lightfoot, N., "Transport phenomena" 2nd Edition, John Wiley & Sons, New York (2002).

6. Nomenclature

List of symbols

Br	Brinkman number = $mu_m^{n+1}R^{n-1}/ [k (T_w - T_c)]$
c_p	specific heat ($J\ kg^{-1}\ K^{-1}$)
h	local heat transfer coefficient ($W/m^2 .K$)
n	power-law model parameter ($Pa.s^n$)
Nu	local Nusselt number = 2hR/k
r	radial coordinate (m).
R	pipe radius (m)
T	fluid temperature (K)
u	axial fluid velocity (m/s)
u_m	mean axial fluid velocity (m/s)

Pe	Peclet number = $2u_mR/a$
q_w	constant heat flux (W/m^2)
z	axial coordinate (m).

Greek symbols

η	dimensionless axial coordinate $=z/(u_mR^2 . a)$
k	thermal conductivity (W/m K)
θ	dimensionless fluid temperature = $(T_w - T)/(T_w - T_c)$
f	dimensionless velocity = u/u_m
a	thermal diffusivity (m^2/s)
ρ	fluid density (kgm^{-3})
τ_{rx}	shear stress (Pa/m^2)
ξ	dimensionless radial coordinate = r/R

Subscripts

b	bulk
c	centerline
w	wall